

**Signaling Mechanisms on Membrane Surfaces: Studies of Membrane-Bound
Master Kinases**

By

Thomas Christopher Buckles
B.S., University of Oklahoma, 2013

A thesis submitted to the
Faculty of the Graduate School of the
University of Colorado in partial fulfillment
of the requirement for the degree of
Doctor of Philosophy
Department of Biochemistry
University of Colorado
2019

This thesis entitled:
Signaling Mechanisms on Membrane Surfaces:
Studies of Membrane-Bound Master Kinases
written by Thomas Christopher Buckles
has been approved for the Department of Biochemistry

Joseph J. Falke

Jeffrey C. Cameron

Date_____

The final copy of this thesis has been examined by the signatories, and we find that both the content and the form meet acceptable presentation standards of scholarly work in the above mentioned discipline.

Buckles, Thomas Christopher (Ph.D., Biochemistry)

Signaling Mechanisms on Membrane Surfaces: Studies of Membrane-Bound Master Kinases

Thesis directed by Professor Joseph J. Falke

The leading edge pseudopod of polarized chemotaxing eukaryotic cells is a membrane associated signaling platform integral to movement, gene expression, growth and proliferation. In spontaneously polarized leukocytes such as macrophages, for example, the leading edge pseudopod guides cell movement up attractant gradients during the innate immune response. To accomplish this, a complex network of kinases and other proteins, including PI3K, AKT1, Ras superfamily G-proteins and RTKs assemble at the leading edge membrane where they control pseudopod stability and the direction of migration. More broadly, many of the same proteins assemble on membrane surfaces in growing cells where they control normal cell growth and survival, as well as oncogenesis in many human cancers. Despite their importance to practical applications and human health, the protein-protein interactions and regulatory mechanisms of these proteins' interactions remain largely unresolved. The first part of this research focuses on elucidating the mechanism by which Ras and soluble phosphopeptides synergistically activate PI3K. Specifically, the small G-protein Ras is known to bind and activate the lipid kinase PI3K, which phosphorylates the constitutive plasma membrane lipid phosphatidyl-inositol-(4,5)-bisphosphate (PIP₂) thereby generating the crucial signaling lipid phosphatidylinositol-(3,4,5)-bisphosphate (PIP₃). This Ras-PI3K-PIP₃ signal regulates cell migration through cytoskeletal and membrane reorganization. In cell growth and survival pathways, the same Ras-PI3K-PIP₃ signal stimulates normal cell growth, while excessive PIP₃ generation can trigger or support oncogenesis leading to many human cancers. Consequently, Ras and PI3K are important oncogenes, such that about one quarter of all human tumors show mutations in a member of the Ras family, and over 200 oncogenic mutations linked to human cancers have been identified in PI3K α . Two contrasting mechanisms of Ras activation of PI3K

have been discussed in the literature: one proposes that Ras recruits additional PI3K to the membrane surface, while the other proposes that Ras binding allosterically activates the PI3K catalytic site. *In vitro* single molecule TIRF microscopy was employed to resolve these hypotheses by measuring the lipid kinase turnover rate of PI3K and its membrane surface binding density in the presence and absence of Ras. The findings directly reveal the mechanism of synergistic PI3K activation by Ras and soluble phosphopeptides: Ras is found to dramatically increase the membrane recruitment of PI3K rather than allosterically activating its catalytic site. The second part of this work focuses on the effects of common therapeutics on the leading edge pseudopod of polarized macrophages and illustrates simple cell morphology and PIP₃ signaling assays employing live cell fluorescence and DIC microscopy to quantify these effects, both at a single-cell and population level. The findings reveal that certain drugs do not detectably perturb the leading edge, while rapid addition of other drugs causes temporary leading edge pseudopod collapse followed by slow adaptation and recovery. Specifically, both ibuprofen and acetaminophen, over the counter pain therapeutics, cause leading edge collapse when added rapidly to polarized macrophages, followed by a full recovery within three hours. Live cell fluorescent and DIC microscopy was used to address this effect. The results suggest the need to identify drugs that perturb the leading edge pseudopod of macrophages and other leukocytes, and to administer those drugs sufficiently slowly to avoid pseudopod collapse and likely inhibition of the innate immune response.

Acknowledgements

This work is a continuation of others' efforts. First, I'd like to acknowledge current and past lab members whose shoulders I stand on – Dr. Jeff Knight, Dr. John Evans, Dr. Kyle Landgraf, Mo Gordon, Hayden Swisher, Justin Martyr, and Nick Cordaro were all integral in the initiation and development of these projects. Special recognition is needed for Dr. Brian Ziemba, whose advice and experience let me see the forest for the trees. Finally, Dr. Joe Falke, whose mentorship and thoughts shaped both me and the work herein.

Family and friends' support were important to me throughout my Ph.D. My parents and brothers: Jeff, Katy, John, and Joe, without whom I would not be where I am. My friends, from Denver to Oklahoma to Texas, who never let me feel alone. My doggos, Ollie and Huckleberry, who taught me what loyalty is. Finally, my wonderful girlfriend Charli, whose unrelenting happiness is a tide that lifts all boats.

I also gratefully acknowledge Olga Perisic for expert PI3K purification and Jay Groves for kindly providing the H-Ras expression plasmid as well as helpful conversations with expert colleagues, including: Dr. Roger Williams from University of Cambridge, Prof. Anna Huttenlocher from University of Wisconsin, Madison; and Drs. Ken Hunt, Rachel Frank, and Sourav Poddar from the University of Colorado Sports Medicine Clinic. Resources and experts at the University of Colorado, Boulder were integral to the completion of this work: The BioFrontiers Advanced Light Microscopy Core (Dr. Joseph Dragavon), The Biochemistry Cell Culture Facility (Dr. Theresa Nahreini, Nicole Kethley), and The Biochemistry Mass Spectrometry Laboratory (Danijel Djukovic, Thomas Lee). Finally, I thank funding programs for support: NIH R01 Grant GM063235 (JJF), the Medical Research Council (MC U105184308 to R.L.W.), the AstraZeneca/LMB Blue Skies Initiative (MC A024-5PF9G to R.L.W.), and St. Catharine's College (G.R.M.), NIH Grant S10-RR021005 (Sciex API 4000 QTrap Mass Spectrometer), and the NIH/CU Molecular Biophysics Training Program (TCB).

Table of Contents

Chapter I:

Signaling Mechanisms on Membrane Surfaces: Studies of Membrane-Bound Master Kinases

Overview	1
RTK-Ras-PI3K α signaling and activation	4
Leukocyte leading edge stability is affected by rapid exposure to therapeutics	8
Single molecule and cellular methods overview.....	9
Thesis outline	12

Chapter II:

Mechanism by Which Receptor and H-Ras Synergistically Activate PI3K α and PIP₃ Signaling: A Single Molecule Study

Abstract.....	14
Introduction	15
Methods.....	18
Results.....	23
Discussion.....	33

Chapter III:

The Leading Edge Pseudopod of Leukocytes: Specific Therapeutics Trigger Pseudopod Collapse Followed by Adaptation and Recovery

Abstract.....	40
---------------	----

Introduction	41
Methods.....	43
Results.....	49
Discussion.....	61

Chapter IV:

Discussion and Future Studies

A Role for Ras in Altering the Docking Geometry and Specific Activity of PI3K α ...	65
Preliminary and Future Studies of Other G Protein-PI3K Signaling Modules	71
Preliminary and Future Studies of Leading Edge Pseudopod Collapse by Other NSAIDs.....	76
Expanding the Diagnostic Protocol for Characterizing Drug Effects on the Leukocyte Leading Edge Pseudopod	77

References	79
-------------------------	----

Appendices

A. Protocol for Liposome Creation and Deposition for Single Molecule TIRF Fluorescence Tracking	91
B. Protocol for Tethering Small G-Proteins to Deposited Lipid Bilayer.....	96
C. TIRF Microscope Setup and Use (Homebuilt Nikon TE-2000)	97
D. H-Ras Purification Protocol.....	100
E. Protocol for RAW 264.7 Culture Method	103
F. Protocol for RAW 264.7 NSAID Addition Experiments, Fast Methodology	105
G. Protocol for RAW 264.7 NSAID Addition Experiments, Slow Methodology	107
H. Protocol for Sfp Protein Site-Specific Labeling Procedure.....	108

I. Diffusion Coefficient Considerations 110

List of Tables

Chapter I:

Table 1.1. Common lipids used for single molecule experiments 7

Chapter II:

Table 2.1 - Controls comparing the surface densities and diffusion characteristics of different H-Ras nucleotide binding states and different numbers of coupled lipids 26

Chapter III:

Table 3.1. Therapeutic drugs and control compounds employed in this study 51

List of Figures

Chapter I:

Figure 1.1. Leading edge signaling platform assembly.....	2
Figure 1.2. Leading edge pseudopod collapse of polarized macrophages	8
Figure 1.3. Population averages of varied molecular systems can portray similar behavior.....	10
Figure 1.4. TIRF microscopy detection of single molecule labeled protein bound to signal lipid.....	12

Chapter II:

Figure 2.1. Molecular schematic of PI3K complex synergistically activated by receptor and G protein in the single molecule kinase activity assay	16
Figure 2.2. Modular representation of the H-Ras and PI3K α proteins used in this study	19
Figure 2.3. Synergistic phospho-Tyr peptide and H-Ras stimulation of PI3K α : Controls examining the dependence on H-Ras density and number of lipidation sites	24
Figure 2.4. Effect of receptor-derived, phospho-Tyr peptide (pYp) and H-Ras on net PI3K α kinase activity and PIP ₃ production	27
Figure 2.5. Controls examining the effects of PI3K activators on the binding of PH domain to PIP ₃	28
Figure 2.6. Synergistic phospho-Tyr peptide and H-Ras stimulation of PI3K α : Controls examining the H-Ras membrane anchoring and nucleotide requirements.....	29
Figure 2.7. Effect of pYp and H-Ras on PI3K α membrane recruitment, and on the specific kinase activity of the membrane-bound enzyme	31
Figure 2.8. Effect of pYp and H-Ras on PI3K α association-dissociation kinetics.....	32
Figure 2.9. Detecting and quantifying single protein molecules diffusing in 2-dimensions on the target supported lipid bilayer	34
Figure 2.10. Working model for the mechanism of synergistic PI3K α activation by receptor-derived phospho-Tyr peptide and H-Ras.....	38

Chapter III:

Figure 3.1 Representative images of spontaneously polarized RAW macrophages illustrating the leading edge pseudopod and effects of inhibitors	46
Figure 3.2. Short term effects of rapid drug addition on single polarized RAW macrophages	54
Figure 3.3. Effect of drugs on the lipid kinase activity of purified PI3K in an in vitro PIP ₃ production assay	55
Figure 3.4 Long term effects of rapid drug addition on populations of polarized RAW macrophages.....	57
Figure 3.5. Stability of therapeutic drug concentrations in cell culture after rapid drug Addition.....	58
Figure 3.6. Effects of slow drug addition on populations of polarized RAW macrophages.	60

Chapter IV.

Figure 4.1. To-scale model of H-Ras-PI3K γ - Lipid Bilayer.....	67
Figure 4.2. PI3K β activity on supported lipid bilayer	72
Figure 4.3. Single molecule kinase assay measurements of Rab5 activation of VPS34 complex II	73
Figure 4.4. Single molecule assay measurements of VPS34-membrane surface binding and effect of fluorescent nanobody on VPS34 kinase activity	75
Figure 4.5. Preliminary leading edge pseudopod data for alternate pharmaceuticals	77

Appendices

Figure A1.1. pixel measurements of normal point spread functions in TIRF apparatus	110
--	-----

Chapter I:

Signaling Mechanisms on Membrane Surfaces: Studies of Membrane-Bound Master Kinases

Overview

Leukocyte chemotaxis is a highly specialized, sensitive, and essential component in human health, playing a key first responder role in innate immunity – a process that controls the targeted destruction of infectious agents, extracellular debris, and endogenous cancers (1-6).

The presence of a chemical gradient of attractant for the cell to sense is required for the cell to effectively chemotax. The cell, beginning in an area of low attractant concentration, can sense and migrate up an attractant gradient towards an area of higher attractant concentration. Example attractant gradients include inflammatory markers released by other cells such as interleukin 1-alpha (IL-1A), growth factors such as platelet derived growth factor (PDGF), nutrients such as adenosine triphosphate (ATP), and bacterial metabolites (7-9).

The ability of leukocytes to effectively sense the attractant gradient and functionally migrate is reliant on a complex network of signaling proteins and second messengers that assemble at the leading edge. In leukocytes this network can assemble even in the absence of an attractant gradient, yielding a spontaneously polarized cell ready to respond immediately to the appearance of a gradient. These pathway proteins and second messengers include receptor tyrosine kinases (RTKs); Ca^{2+} ; phosphoinositide-3-kinase (PI3K) and its product signaling lipid phosphatidylinositol-3,4,5-trisphosphate (PIP_3); protein kinase C (PKC); Phosphatase and tensin homolog (PTEN); small G-proteins (e.g. Ras, Rac, Rab); AKT1; and actin filaments (Fig. 1.1) (8, 10-19).

A similar or identical pathway composed of the same protein and lipid elements plays a central role in controlling cell growth and survival under normal growth conditions, and oncogenic mutations in this pathway trigger or support oncogenesis in many human cancers.

For example, mutations in PI3K α or Ras have been found in ~15% or ~25% of all cancers, respectively (20-22). A small number of specific residues found in PI3K α (E542, H1047) and Ras (G12) bear much of the responsibility, and are represented in 7% and 11% of all cancers, respectively (21, 22). A more thorough understanding of the molecular mechanisms of pathway components and their regulation will be significant contributions to signaling biology and could open important new directions in rational and computational drug discovery.

In both pathways, when an attractant small molecule or growth hormone binds and activates a transmembrane receptor tyrosine kinase (RTK), the RTK recruits additional copies or novel signaling proteins, including PI3K, to the inner leaflet of the plasma membrane. There are three total classes of PI3K in mammals – class I, II, and III. Within class I, there are four catalytic isoforms - α , β , γ , and δ . The primary function of class I PI3Ks is to catalyze the phosphorylation of plasma membrane phosphatidylinositol 4,5-bisphosphate

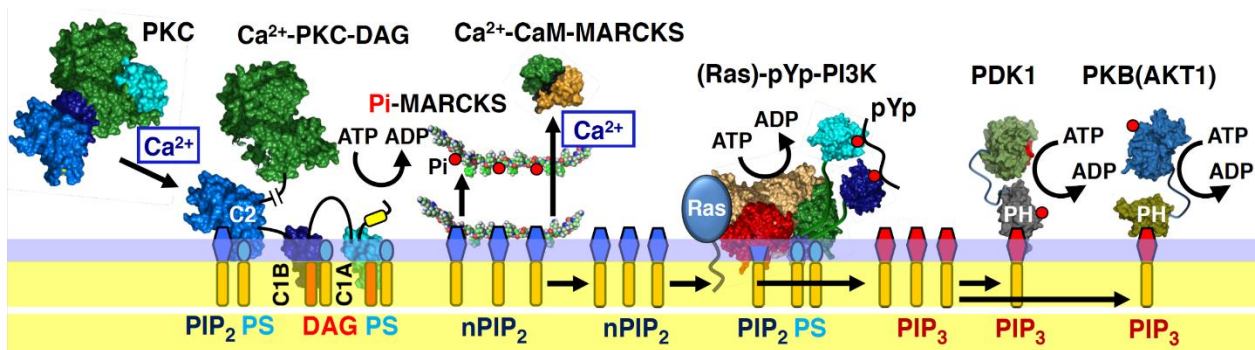


Figure 1.1. Leading edge signaling platform assembly. Extracellular Signal sensing recruits a complex network of signaling proteins and second messengers. PKC and Ca⁺² release PIP₂ from MARCKS sequestration. This allows Ras activated PI3K to phosphorylate PIP₂ into PIP₃, a strong second messenger for PH domains, such as AKT and PDK, another activator of AKT. Phospho Tyrosine Kinase activation motif (RTK, soluble activator) remove PI3K autoinhibition and allow for membrane binding competency (represented as pYp).

(PIP₂) to yield phosphatidylinositol 3,4,5-triphosphate (PIP₃), though class I can also indirectly generate phosphatidylinositol 3,4-bisphosphate from phosphatidylinositol 4-phosphate (23, 24).

There are three class II isoforms, PI3K α , β , and γ . Class II PI3Ks generate phosphatidylinositol-

3-phosphate (PI-3-P) from phosphoinositol (PI), and PI 3,4-phosphate from PI-4-phosphate. Class II PI3Ks have received little attention to date and represent an interesting line of inquiry due to their largely mysterious set of downstream effectors and upstream activators. The Class III PI3K, although named last, could represent the ancestral inositol lipid kinase due to its ubiquity across eukaryotes. There is only one class III isoform, named VPS34. The primary function of the class III isoform is the phosphorylation of PI into PI-3-P on endosomal membranes. VPS34 and its small G-protein activator Rab5 are further discussed in Chapter IV. Both class I and class III have constitutively bound regulatory subunits: p85 α , β , γ , and δ for class I, and VPS15 for class III. These regulatory domains inhibit kinase activity to prevent rampant growth and gene expression changes without proper initiation (23, 25-28). This work will primarily focus primarily on the class I PI3K α , as well as preliminary studies of the class III PI3K VPS34. Class I and III PI3Ks have activation input from small GTPases in the Ras superfamily or from heterotrimeric G proteins, while class I PI3Ks hold the distinction of direct activation by receptors and soluble phospho-Tyr proteins (RTKs, GPCR G $\beta\gamma$, IRS-1, Gab) (23, 29, 30).

Due in part to the extensive level of signal propagation and reinforcement, the PI3K signaling pathway possesses exquisite sensitivity and speed. Sensitivity is integral to the functionality of chemotaxis, as the cell must be able to respond over large macroscopic distances to minute concentration gradients with low amplitudes and slopes. Signaling speed is needed to minimize response time, allowing the cell to respond with lower latency. In the case of infectious agents this helps prevent foreign agents from taking foothold in a host organism. Misregulation of any component of the chemotaxis pathway can trigger inflammatory or innate immunity problems, or in the cell growth pathway can trigger or support carcinogenesis.

RTK-Ras-PI3K α signaling and activation. RTK-Ras-PI3K α activation represents a central signaling module in chemotaxis, growth, and proliferation. As one of the central activators of PI3K signaling, Ras, as well as PI3K itself, are important players in inflammation and innate immunity, and can stimulate tumorigenesis when hyperactive. Membrane-bound Ras associates with PI3K at the membrane surface and synergizes with phospho-Tyr proteins to drive PI3K binding to its substrate lipid PIP₂ (Table 1.1) and activation of the PI3K catalytic domain. The master kinase PI3K catalyzes a phosphorylation event to create the strong second messenger signaling lipid PIP₃. Many proteins possessing a plextrin-homology (PH) domain, including PDK1 (phosphoinositide-dependent kinase 1) and AKT1 (also called protein kinase B, or PKB), are then recruited to the lipid membrane (31) by way of their strong affinity for the PIP₃ second messenger lipid where they begin their own signaling processes. PDK1 phosphorylates AKT1 at position Thr308, enhancing AKT1 activity (Fig. 1.1) (32). This post-translational modification (PTM) acts as a positive reinforcement and signal propagation pathway in PI3K signaling. The master kinase AKT1 is upstream of multiple important signaling pathways, including mammalian target of rapamycin 1 (mTORC1) and forkhead box protein O1 (FOXO), both strong regulators of apoptosis and metabolism (23). AKT1 also has direct influence over the transcription factors BAD, BAX, and NF- κ B, enhancing cell growth and downregulating apoptosis (20, 33-35).

Just as important as signaling reinforcement is signal termination. The primary deactivator of PI3K signaling is phosphatase and tensin homolog (PTEN), an important tumor suppressor gene due to its function in this pathway. Specifically, PTEN removes the 3' phosphate group from the inositol ring of PIP₃, restoring it to the substrate PI3K lipid PIP₂. PTEN activity loss has been found in up to 70% of primary prostate tumors, as well as significant percentages of gastric cancer, non-small cell lung cancer, endometrial hyperplasia, and autism cases (36-42).

An additional key element of PI3K regulation, the protein myristoylated alanine-rich C-kinase substrate (MARCKS), acts as a PIP₂ buffer by sequestering PIP₂ for release during a signaling event. It accomplishes this by utilizing a highly cationic stretch of residues that electrostatically bind to the strong negative charge of multiple PIP₂ headgroups with high affinity. Upon signal activation, Ca²⁺ release activates protein kinase C (PKC) and/or calmodulin to phosphorylate or bind MARCKS, respectively, thereby displacing it from PIP₂ (Fig. 1.1) (8). This mechanism provides both a check on PI3K reaction speed and an additional layer of signal control.

Canonically, transmembrane RTKs and their downstream phospho-Tyr proteins are the primary direct activators of class I PI3Ks. A monomeric, inactive RTK, upon binding a target ligand, will typically dimerize with another RTK molecule, bringing their cytoplasmic kinase domains into proximity. Once near each other, the kinase domains will trans-autophosphorylate each other at cytoplasmic tyrosine residues, stimulating them to phosphorylate downstream proteins on Tyr residues. The autoinhibitory SH2 domains of the p85 regulatory subunit of PI3K bind to the resulting phosphotyrosines on RTKs or soluble downstream proteins. This binding event initiates a structural shift in the regulatory subunit, thereby displacing the inhibitory SH2 domains from the membrane binding surface of the catalytic domain, and exposing the active catalytic helical elements for membrane and PIP₂ binding (29, 30, 43-45). Example PI3K RTK activators include Platelet Derived Growth Factor Receptor β (PDGFR β) and Epidermal Growth Factor Receptor (EGFR). In addition to transmembrane RTKs, soluble phosphotyrosine activators such as IRS-1 and Gab are capable of direct PI3K α activation (30, 45-48). Soluble phospho-Tyr proteins such as these, which remove the inhibitory SH2 domains in a similar manner, represent a closely related PI3K activation mechanism.

Members of the small GTPase Ras superfamily have been shown to directly bind and activate class I PI3Ks as well, a subject explored in greater detail further in this composition.

Until this work, the mechanism by which H-Ras combines with phosphotyrosine to synergistically activate the master kinase PI3K α has remained a mystery. The first evidence of a Ras PI3K interaction was PI3K kinase activity in Ras immunoprecipitations from transformed cells in 1991 (49). Three years later, it was demonstrated that the two proteins directly interact by anchoring Ras to agarose beads and pulling down PI3K (50). In 2000, the first crystal structure of any Ras-PI3K isoforms (H-Ras-PI3K γ) was shown, with PI3K γ exhibiting a widened PIP₂ substrate binding cleft when bound to Ras, suggesting an allosteric component to Ras-PI3K activation (51). However, live cell and in vitro studies (52, 53) suggested that Ras may also recruit additional PI3K to the membrane, leading to the alternative hypothesis that Ras activates via membrane recruitment rather than by allosteric activation of the catalytic site. These previous studies could not measure the effect of Ras association on the turnover rate of individual, membrane-bound PI3K molecules, thus the relative importance of activation by allostery and recruitment could not be judged. Chapter II shows that Ras activates the PI3K-phosphoprotein complex by the membrane recruitment mechanism, with a small but reproducible decrease in specific lipid membrane kinase activity. Specifically, these Chapter II studies focused on H-Ras activation of PI3K α . H-Ras and class I PI3K α are both ubiquitously expressed, and are representative of their respective protein families (22, 54). We expect the findings to be generalizable to other Ras isoforms (N, and K Ras, with K-Ras existing in two splice variants: 4A and 4B), and other PI3K isoforms activated by membrane association (19, 50, 55-58). A more complex Ras activation mechanism may apply when PI3K is bound to a membrane component such as an RTK.

Development of therapeutics for this signaling pathway has remained elusive, in part due to the complex nature and the many feedback loops that exist in the pathway. The findings presented in chapter II uncover an important molecular mechanism that could aid future therapeutic design.

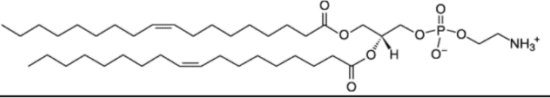
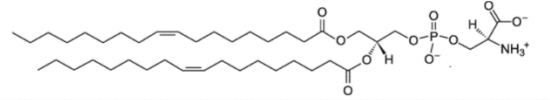
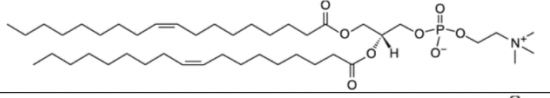
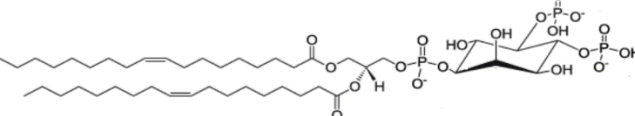
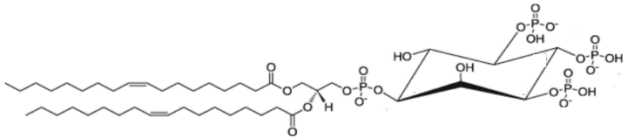
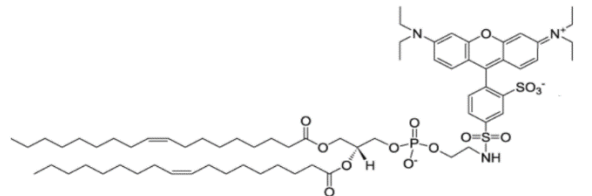
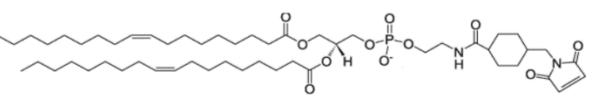
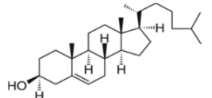
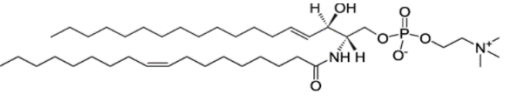
Lipid	Structure	M.W.	Mol % PI(3)K Assay	Mol % Fluorescent Control	Mol % P.M. Mimic
DOPE		743.44 Da	73	-	28
DOPS		801.21	25	-	23
DOPC		786.11	-	99+	12
PIP ₂		1074.18	1	-	1
PIP ₃		1171.17	Trace	-	Trace
DOPE-LRB		1371.72	-	~100ppb	-
DOPE-MCC		985.25	1	-	-
Cholesterol		385.65	-	-	26
Sphingomyelin		729.10	-	-	8

Table 1.1. Common lipids used for single molecule experiments. This table represents a non-exhaustive list of common synthetic lipids, their structures, molecular weights (in daltons), and their mole percentage utilization in various supported lipid bilayer preparations. Abbreviations: DO – Dioleoyl; PE – Phosphoethanolamine; PS – Phosphoserine; PC – Phosphocholine; PIP₂ – Phospho-1'-myo-inositol-4,5 bisphosphate; PIP₃ - Phospho-1'-myo-inositol-3,4,5 triphosphate; DOPE-LRB – DOPE-N-Lissamine Rhodamine-B sulfonyl; DOPE-MCC – DOPE- N-[4-(p-maleimidomethyl)cyclohexane-carboxamide (59).

Leukocyte leading edge stability is affected by rapid exposure to therapeutics. In addition to understanding the molecular mechanisms of individual proteins for leading edge signaling in leukocyte chemotaxis and innate immunity, it is also important to address whether compounds, especially therapeutic drugs used in the clinic, cause leading edge perturbation at a cellular level. In the presence of an attractant gradient, or often even in the absence of a gradient, a leukocyte deploys a leading edge pseudopod. This pseudopod is characterized by a ruffled, extended cytoplasmic projection from the cell body (Fig 1.2A). Due to the importance of the leading edge in attractant gradient sensing and motility, it is key for a proper innate immune response that any drug-induced disruption to the leading edge is known, especially in immunocompromised individuals.

Chapter III reveals that some therapeutic drugs, namely acetaminophen and the NSAID ibuprofen, collapse the leading edge pseudopod area and PIP₃ density at the single cell level when added rapidly (entire therapeutic dosage applied at t = 0) (Fig 1.2 B). Further population studies show that pseudopod collapse is alleviated by introducing the perturbing drug to the

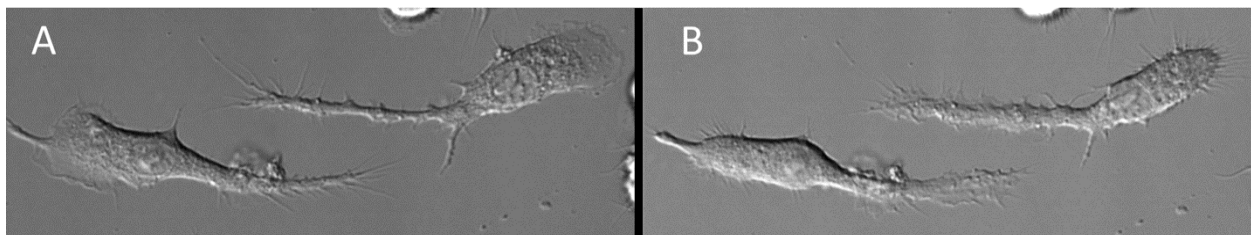


Figure 1.2. Leading edge pseudopod collapse of polarized macrophages. (A) Two archetypal polarized RAW 264.7 macrophages displaying active, ruffled leading edges. **(B)** Five minute rapid exposure to the NSAID ibuprofen produces a pronounced collapse of the leading edge inwards. This collapse is fully recovered after three hours (Chapter III, Fig 3.3).

cells slowly over the course of one and a half hours, in which case leading edge pseudopod integrity is maintained. Moreover, after pseudopod collapse is triggered by rapid drug addition, slow full pseudopod recovery is observed at the population level over the course of two to three hours, indicating that the perturbation is temporary, and the cells eventually adapt to the high drug concentration. Two other NSAIDs that were tested, acetylsalicylic acid (aspirin) and diclofenac, cause no such perturbation.

The mechanism for the observed drug-triggered pseudopod collapse is unknown. The drugs do not degrade over time as determined by mass spectrometry (Fig. 3.4), nor does collapse correlate with drug pKa, charge, or mass (Table 3.1). The mechanism of recovery is also unknown – however, the leukocyte leading edge signaling pathway, like all sensory pathways, possesses an efficient adaptation mechanism vital to its ability to direct movement in gradients superimposed on different constant background concentrations of attractant. This adaptation pathway may well play a role in pseudopod recovery after drug-induced collapse, and in the lack of collapse observed when the perturbing drug is added sufficiently slowly.

Single molecule and cellular methods overview. Addressing different questions about how the leading edge signal pathway operates and responds to stimuli requires different techniques, each of which may be better suited to the specific challenges presented by a hypothesis. The complex nature, feedback loops, and multiple inputs of the leading edge signal pathway suggest an in vitro approach for mechanistic studies, whereby an isolated system can be assembled, and the system reduced to the essential components required for addressing a given question.

Working in the single molecule regime presents multiple benefits. First, it allows distinguishing individual subpopulations and characterization of their different qualities, which is difficult or impossible in a bulk measurement that combines all subpopulations into an “ensemble average” (Fig. 1.3). Furthermore, single molecule measurements allow the user to

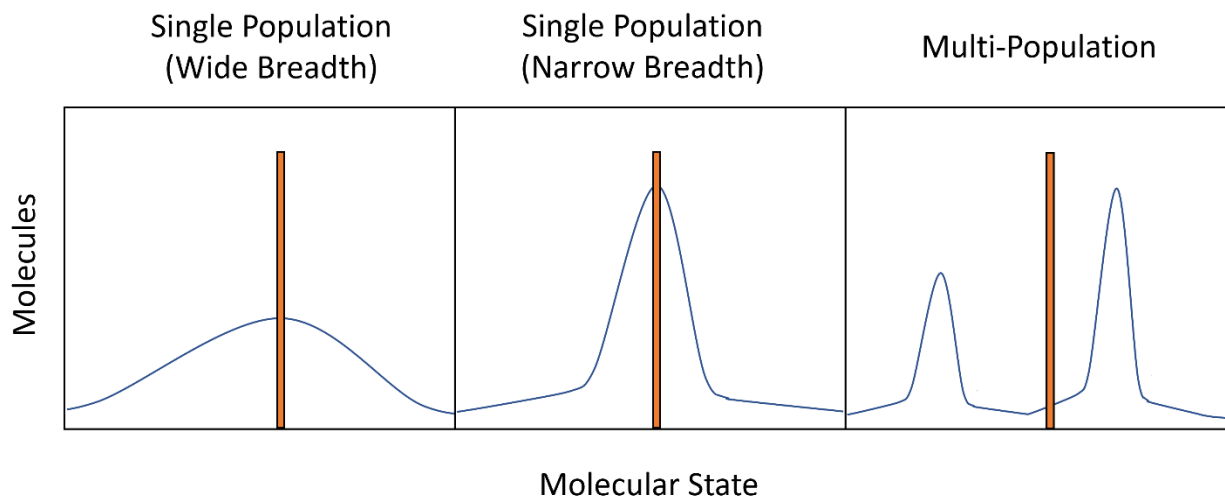


Figure 1.3. Population averages of varied molecular systems can portray similar behavior. The population average (orange bar) of all three exemplified systems is equivalent – however, each system exists in different substates. Population one exists in many subpopulations, spread across a wide array of molecular states. Population two exists in a narrow band of a few populations. Population three exists as two independent populations, separated by non-occupied states. Each macropopulation average is similar and would be indistinguishable in an ensemble bulk measurement.

define the proportional role that outliers play in the mean macropopulation. Additionally, single molecule dynamics can be directly monitored on a timescale of 20 ms, the video frame rate of the TIRFM system employed in these studies. Appendix I further explores the time scale of diffusion in our system relative to image capture rate. Together these features allow the user to view steps in a reaction process that would be invisible in most ensemble studies, allowing a more detailed molecular mechanism to be elucidated. Finally, in the Chapter II studies of signaling reactions on a membrane surface, the single molecule analysis of 2-D diffusion on a membrane surface allows direct measurement of the diffusion coefficient of a homogeneous population, or the individual diffusion coefficients of subpopulations, as well other key features of diffusional behavior.

To quantify these parameters for signaling reactions in the Ras-PI3K-PIP₃ pathway reconstituted on a membrane surface (Chapter II), a total internal reflection fluorescence (TIRF)

microscopy approach is ideal. In objective based TIRF microscopy, incoming excitation laser light is projected to the objective at an angle beyond the critical angle of reflection, such that it is totally reflected rather than refracted. However, an evanescent wave of excitation is projected beyond the objective approximately 200 nanometers (Fig 1.4). The amplitude of this evanescent wave decays exponentially as the distance from the surface is increased. The advantages of a TIRF imaging technique include a significantly lower fluorescent background due to the decaying evanescent wave of excitation, which excites only fluorophores at or near the surface, such that excess fluorophore can be added to the bulk solution phase with minimal background impact, as the majority of dye in solution will not see any excitation light. Since the evanescent wave is present only near the surface of the experiment, it lends itself perfectly to a study of membrane-associated proteins on a supported lipid bilayer, in which all characters of interest are located on the surface-deposited membrane. In our single molecule TIRFM studies we track the 2-D diffusion of individual molecules on the surface over time, yielding for each a single molecule diffusion "track". Fluorescent tracks can be filtered by length, brightness, or diffusion coefficient to focus on a target population and eliminate contributions from many contaminants. The resulting data has myriad applications – surface diffusion kinetics, on and off rates from the surface, surface binding density, protein-protein interactions, and protein-lipid interactions can all be calculated from track data.

In contrast, a more holistic approach employing live cell studies is needed to assess the effects of drugs on the leukocyte leading edge pseudopod (Chapter III). Cultured RAW 264.7 cells, a murine macrophage cell line, represent a good model system for testing the effects of drugs on the morphology and stability of the leading edge pseudopod. When observing the pseudopod, a combination of techniques can be used, including fluorescence microscopy and differential interference contrast (DIC) microscopy. These techniques are complementary when analyzing both single cell and population level data. Fluorescence microscopy allows measurements of quantities within the cell, such as production of the signaling lipid PIP₃. While

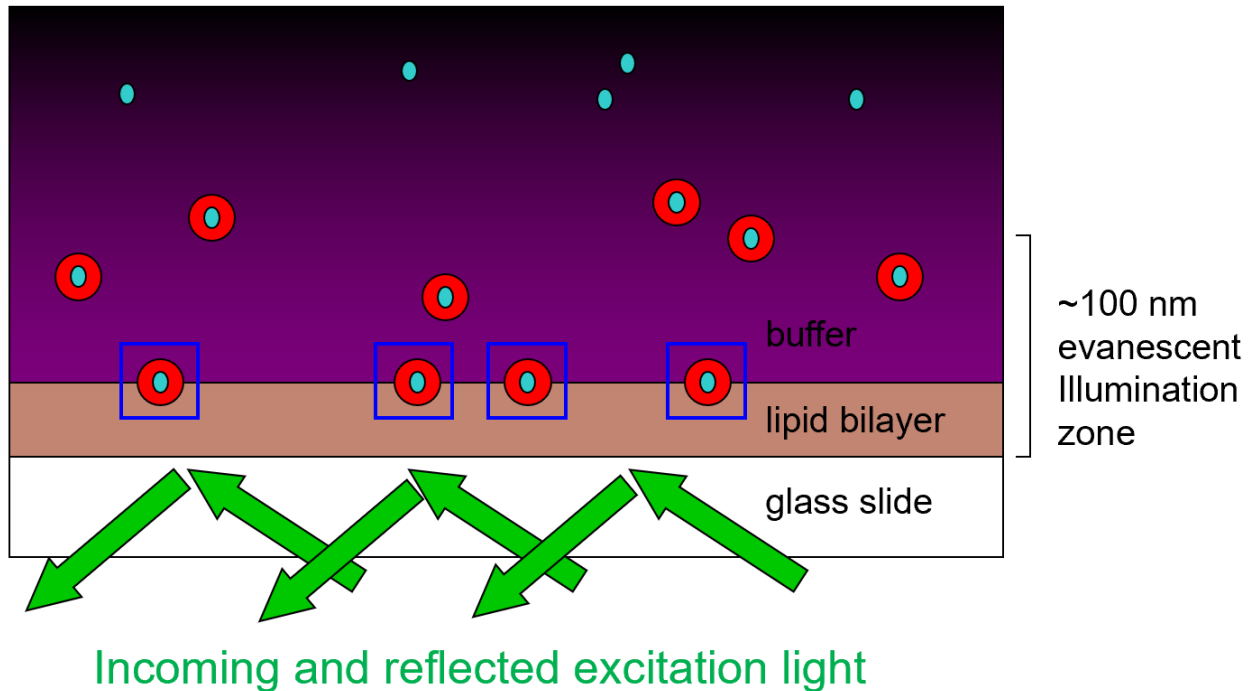


Figure 1.4. TIRF microscopy detection of single molecule labeled protein bound to signal lipid. In TIRF microscopy, incoming excitation light (e.g. 542nm) is projected beyond the critical angle of incidence such that it is totally reflected. A quantum effect of excitation light, the evanescent wave, propagates ~100 nm beyond the surface of reflection, illuminating only dyes at or near the surface of the experiment.

limited in the number of cells that can be employed in this manner per experiment, these measurements can be crucial in understanding cell dynamics, heterogeneity, and mechanisms. In contrast, DIC microscopy is higher throughput, as macrophagic transformations are difficult and time consuming. This high throughput is vital for population level observations.

Thesis outline. In chapter II, the mechanism of synergistic PI3K α activation by H-Ras and soluble phospho-Tyr proteins is explored in detail. Chapter II reveals the mechanism by which Ras activates a soluble PI3K-phosphoprotein complex is a recruitment driven, on-rate dominated one. In addition, this chapter reveals that Ras association triggers a small but reproducible decrease in the specific lipid kinase activity of PI3K, further emphasizing that recruitment, not an allosteric conformational change, is responsible for the synergistic Ras activation of PI3K. The presence of H-Ras on the membrane increases the membrane density of PI3K α ~20-fold, while the protein-protein interaction slows the turnover rate of each PI3K α

stably bound to the membrane surface ~2-fold, yielding a net ~10-fold increase in PI3K α activity and PIP₃ generation.

In chapter III, the collapse of the leukocyte leading edge pseudopod by certain therapeutic drugs is reported for the first time, and the initial features of this phenomenon are described. Acetaminophen and Ibuprofen cause significant disruption of the leading edge pseudopod of cultured murine macrophages when added rapidly. This disruption is alleviated if the drugs are added slowly over time. Other pharmaceuticals, acetylsalicylic acid and diclofenac, cause no leading edge disturbance whether added rapidly or slowly.

In chapter IV, the findings of the experimental sections are summarized and discussed in further detail, as well as future directions for each project. The potential causes of the Ras-triggered small but reproducible drop in PI3K lipid kinase specific activity are explored. Additional related kinase-GTPase modules are mentioned, and how further studies of those modules may serve to give a more universal understanding of PI3K-small-G-protein activation mechanisms. Preliminary evidence for class III PI3K VPS34 activation by the GTPase Rab5 is presented here. Finally, parting thoughts on new therapeutics to test in a macrophage leading edge stability assay (chapter III), as well as expanding the analysis by measuring the effects of perturbing drugs on macrophage chemotaxis are addressed.

Chapter II:

Mechanism by which Receptor and H-Ras Synergistically Activate PI3K α and PIP₃ Signaling: A Single Molecule Study

ABSTRACT

Cellular pathways controlling chemotaxis, growth, and survival are activated by receptor tyrosine kinases (RTKs) and small G proteins of the Ras superfamily that stimulate specific isoforms of phosphatidylinositol-3-kinase (PI3K). These PI3K lipid kinases phosphorylate the constitutive lipid phosphatidylinositol-4,5-bisphosphate (PIP₂) to produce the signaling lipid phosphatidylinositol-3,4,5-trisphosphate (PIP₃). Progress has been made in understanding direct, moderate PI3K activation by phospho-Tyr residues on receptors and soluble activators. In contrast, the mechanism by which phospho-Tyr and Ras synergistically activate PI3K to much higher levels remains unclear, and two competing models have been proposed: membrane recruitment vs. activation of the membrane bound enzyme. To resolve this central mechanistic question, the present study employs single molecule TIRFM to investigate PI3K activation in a six-component pathway reconstituted on a supported lipid bilayer. The findings reveal that simultaneous activation by soluble phospho-Tyr activator and H-Ras generates strong, synergistic, activation of PI3K α , yielding a large increase in net kinase activity via the membrane recruitment mechanism. Synergy requires phospho-Tyr and two anionic lipids (phosphatidylserine (PS) and PIP₂) to make PI3K α competent for membrane binding and catalysis of PIP₃ production. Synergy also requires membrane-bound H-Ras, which greatly speeds the formation of a stable, membrane-bound PI3K α complex. H-Ras and soluble phospho-Tyr accomplish this by modestly slowing the PI3K α off-rate from the membrane, and dramatically increases its equilibrium surface density. Surprisingly, H-Ras binding slightly

inhibits the specific kinase activity of the membrane-bound PI3K α molecule; however, this minor enzyme inhibition is overwhelmed by the great enhancement of membrane recruitment. The results directly show that Ras synergy with soluble phospho-Tyr activators occurs via the PI3K membrane recruitment mechanism, rather than by allosteric PI3K activation. These findings have significant impacts for the fields of chemotaxis, innate immunity, inflammation, carcinogenesis, and drug design.

INTRODUCTION

Receptor-Ras-PI3K-PIP₃ signaling is central to an array of essential pathways. Localized PIP₃ signals are generated at the leading edge membrane of chemotaxing cells, including leukocytes migrating towards a site of infection or inflammation (5). PIP₃ signals also play central roles in cell growth and survival pathways (30). Many human cancers are linked to excessive PIP₃ production arising from oncogenic mutations in receptor, Ras or PI3K components (30, 60-63).

Previous mechanistic studies have shown that receptor tyrosine kinase (RTK) activation of the dominant class IA PI3K family modulates the interaction of the two subunits of the PI3K heterodimer. This modulation occurs when receptor phospho-Tyr residues, located in a flexible cytoplasmic loop, bind to one or both inhibitory SH2 domains of the p85 regulatory subunit (43, 62, 64-66) (Figure 2.1). The resulting phospho-Tyr binding displaces the SH2s from the p110 catalytic subunit, triggering a conformational change that exposes lipid binding surfaces and activates the catalytic site for substrate PIP₂ binding, thereby generating modest levels of membrane binding and kinase activity. Alternatively, soluble phospho-Tyr proteins (e.g. IRS-1, Gab) can directly activate PI3K by displacing the inhibitory SH2 domains, yielding the same conformational change that exposes and activates the membrane binding and catalytic region of

the p110 subunit. For example, IRS-1 is directly phosphorylated on Tyr residues by the insulin RTK, and thereby displays a potent PI3K activation motif with the essential phospho-Tyr residues needed for lipid kinase activation (67-69).

In cells and *in vitro*, receptors and G proteins have been observed to act in concert to synergistically stimulate PI3Ks and PIP₃ production (29, 53, 58). In cells, some stimuli may

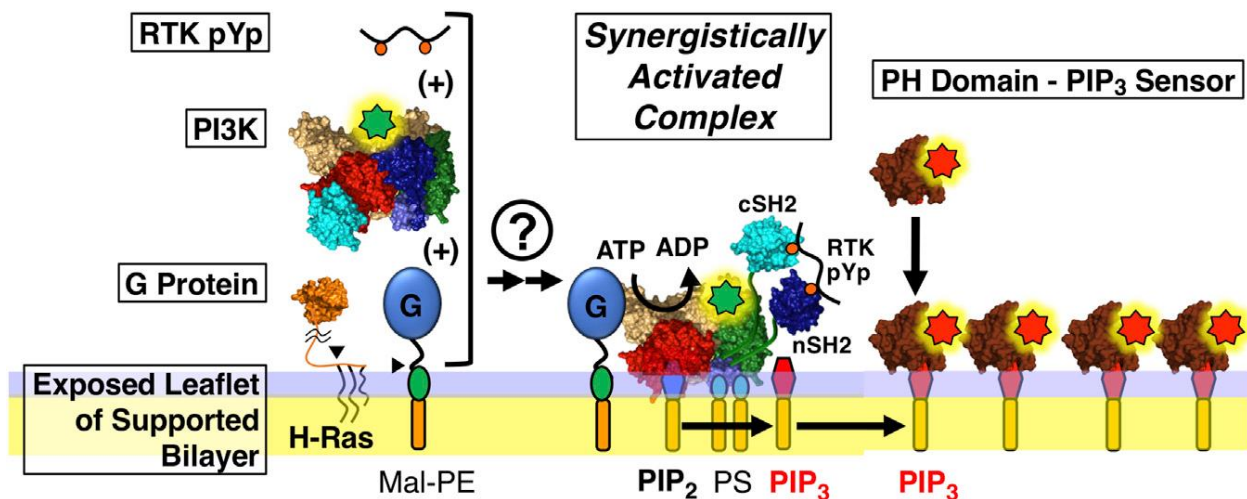


Figure 2.1. Molecular schematic of PI3K complex synergistically activated by receptor and G protein in the single molecule kinase activity assay. Shown is a schematic depiction of the fully active PI3K α complex assembled on the supported lipid bilayer. In this complex, PI3K α is synergistically activated by both (i) the activation loop of the platelet-derived growth factor receptor, an RTK, which is phosphorylated at specific Tyr residues (RTK-pYp), and (ii) the small G protein anchored to maleimide lipid (H-Ras). The arrowhead indicates native Cys 181 that is a palmitoylation site in wild type H-Ras, and is sufficient for stable, functional coupling to maleimide lipid in the *in vitro* single molecule kinase assay. The assay monitors PI3K α -catalyzed production of product PIP₃, where each PIP₃ molecule produced is detected by the binding of fluorescent GRP PH domain added in excess as a PIP₃ sensor. The assay monitors the initial rate of PIP₃ production when less than 2 % of the substrate PIP₂ population is converted to PIP₃. At these low levels of PIP₃, product rebinding to PI3K α is negligible, thus sequestration of the product PIP₃ by the sensor protein is non-perturbing.

simultaneously activate multiple, parallel G protein responses that stimulate multiple PI3K populations to produce additive PIP₃ signals, making it difficult to ascertain whether synergy requires direct, simultaneous binding of receptor and G protein to PI3K (29, 58). *In vitro*, it has recently been demonstrated that the simultaneous presence of receptor phospho-Tyr and G

protein is indeed sufficient to generate synergistic activation of class IA PI3Ks, consistent with the simultaneous binding of both ligands to PI3K at their distinct binding sites identified by crystallographic studies (51, 63, 66).

Two competing models have been proposed for the molecular mechanism by which G protein amplifies the modest PI3K activation triggered by receptor alone to generate dramatic, synergistic activation. In the recruitment model, G protein enhances PI3K binding to the membrane, yielding increased membrane density of the active lipid kinase (52, 70). In the enzyme activation model, the G protein-PI3K interaction increases the specific activity (or turnover number) of each membrane-bound, G protein-associated, kinase molecule (20, 51). The two mechanisms are not mutually exclusive; thus one could dominate, or both could contribute. Current evidence is inconclusive. For example, Ras isoforms do recruit PI3K to the membrane in cells (52). On the other hand, Ras binding does trigger PI3K conformational changes detected in crystallographic and hydrogen-deuterium exchange studies that could, in principle, modulate its enzyme activity (51, 53). Previous studies take opposite sides, or conclude the issue is an open question (51, 53, 58, 70). To date the two models have not yet been resolved for any G protein-PI3K regulatory pair.

To address these mechanistic questions, the present study employs single molecule TIRFM to investigate a representative receptor-Ras-PI3K-PIP₃ signaling module reconstituted from four protein/peptide components and two lipid components on a supported lipid bilayer: (i) A widely employed soluble phospho-Tyr peptide (pYp) is used to mimic the flexible, regulatory phospho-Tyr loop of an RTK receptor (18, 43, 64, 66, 71, 72). The pYp peptide sequence is derived from the platelet-derived growth factor receptor (PDGFR), an RTK central to chemotaxis and inflammation, and possesses phospho-Tyr at one or two conserved phosphorylation sites. (ii) The membrane-anchored, small GTPase H-Ras is employed as a representative Ras isoform. H-Ras is central to leukocyte transmigration and is linked to 65 oncogenic mutations thus far (21, 57, 73). More broadly, mutations in this and other Ras isoforms are linked to

approximately 25% of human cancers (20). (iii) The alpha isoform of PI3K is the most prevalent and oncogenic (63, 74). This heterodimeric lipid kinase is composed of catalytic (p110 α) and regulatory (p85 α) subunits and is activated both by RTKs and Ras isoforms (63, 64). PI3K α is involved in leukocyte chemotaxis and inflammation (5, 75), and is linked to 255 oncogenic mutations (40, 52, 60, 74) (Cosmic database). (iv, v, vi) The anionic lipids phosphatidylserine (PS) and PIP₂ serve as PI3K α lipid binding targets; the latter is also the substrate for PIP₃ production (64, 76). (vii) GRP1 PH domain is a high-affinity PIP₃ sensor employed to specifically detect product PIP₃ even in the presence of high PIP₂ densities (77).

The findings reveal strong, direct synergy between simultaneous soluble phospho-Tyr and H-Ras activators. As previously observed, phospho-Tyr residues are required for modest activation of PI3K α lipid binding and PIP₃ production (65, 66). When membrane-bound H-Ras is also present, the resulting receptor-G protein synergy drives much stronger PI3K α activation, and the findings show this synergy is generated by the membrane recruitment mechanism. The enzyme activation mechanism does not contribute to this activation; instead, the findings reveal that H-Ras binding slightly but significantly inhibits the specific enzyme activity of membrane bound PI3K α .

METHODS

Reagents. Except where noted otherwise, fluors, synthetic lipids, synthetic phospho-Tyr peptide containing the activation loop sequence of platelet-derived growth factor receptor (PDGFR, an RTK), and other reagents and materials were obtained as previously described from the same suppliers (18, 71). In addition, the maleimide headgroup phospholipid DOPE-MCC or Mal-PE, (dioleoyl-phosphoethanolamine-N-[4-(p-maleimidomethyl)cyclohexanecarboxamide]) was obtained from Avanti. Functional PI3K α and GRP1 PH domain were

obtained and labeled with fluorophore by a gentle, enzymatic procedure at their Sfp labeling tag, as previously described (18, 71).

Preparation of supported lipid bilayers possessing membrane-anchored H-Ras. A published method was employed to express and purify unlipidated H-Ras from *E. coli* (78) (Fig. 2.1). Following confirmation of identity by mass spec analysis, the desired nucleotide (generally non-hydrolyzable GTP analogue GMPPNP, or, where indicated, GTP or GDP) was loaded into

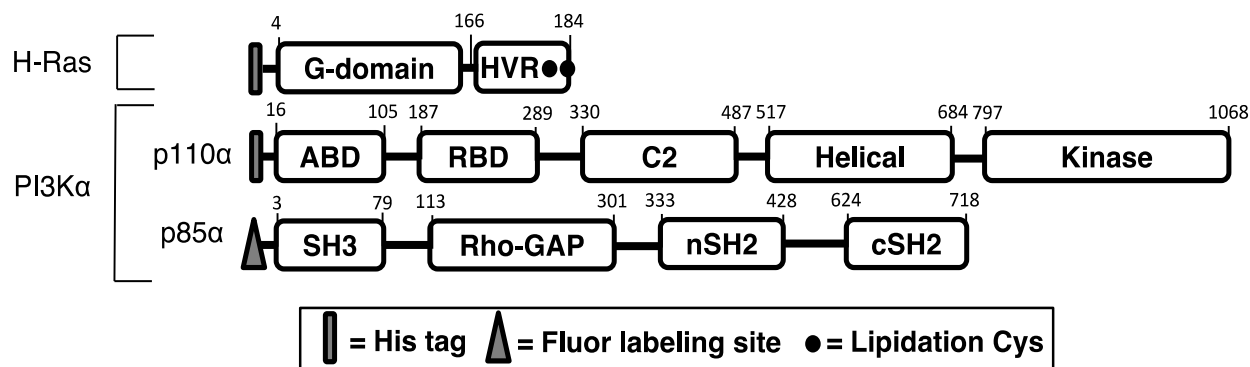


Figure 2.2. Modular representation of the H-Ras and PI3K α proteins used in this study.

The H-Ras 1-184 construct utilized was previously developed by the Groves laboratory (RRR) and possesses an N-terminal 6xHis affinity purification tag, and a mutation (C18S) that removes a surface-exposed Cys residue in the GTPase domain while retaining two C-terminal lipidation Cys residues (Cys 181, 184). The latter two Cys residues are palmitoylated in native H-Ras and are used for membrane anchoring in this study. Finally, the construct deletes the two, C-terminal 185 and 186 residues of native, mature H-Ras. Except where otherwise noted (Fig. 2.6, Table 2.1), H-Ras loaded with the non-hydrolyzable GTP analogue GMPPNP is employed in all experiments.

The full length recombinant human phosphoinositide-3-kinase alpha (PI3K α) employed was described in our previous publications (2,3) and possesses an N-terminal 6xHis affinity purification tag on its p110 catalytic subunit, as well as an N-terminal enzymatic Sfp-labeling tag on its p85 regulatory subunit. H-Ras was recombinantly expressed and purified as described previously (4). To load with the desired nucleotide, a nucleotide replacement reaction was performed as previously detailed (1) by buffer exchanging purified H-Ras into an EDTA rich stripping buffer (150 mM NaCl, 50 mM EDTA, 1 mM TCEP, 20 mM HEPES, pH 7.4) followed by a second exchange into EDTA free, Mg²⁺ containing kinase buffer (100 mM KCl, 15 mM NaCl, 2 mM EGTA, 1.9 mM Ca²⁺, 5 mM Mg²⁺, 1 mM TCEP, 20 mM HEPES, pH 6.9). The nucleotide of choice was then added in excess of H-Ras followed by a 20 min incubation at 21° C. Finally, aliquots were snap frozen in liquid N₂ and stored at -80° C. When samples are thawed on ice and used in experiments, the added nucleotide is included at a concentration of 1 mM in all experimental buffers, to ensure that any nucleotide that dissociates is replaced.

H-Ras by nucleotide exchange using a standard, high EDTA exchange method (78). The bilayer lipid mixture employed was DOPE : DOPS : DOPIP₂ : DOPE-MCC in mole ratios 73:25:1:1. Our previously described procedures (18, 71, 77, 79, 80) were used to deposit a homogeneous bilayer composed of these lipids on ultra-clean glass, yielding a supported lipid bilayer (29). The purified, nucleotide-loaded H-Ras was covalently coupled to the headgroups of DOPE-MCC via its native membrane-anchoring Cys residues 181 and 184 or, where noted, via only Cys 181 (see Table 2.1). After washing the bilayer to remove all remaining free H-Ras, the surface density and diffusion speed of anchored H-Ras were measured by single molecule TIRFM using a fluor-tagged, antibody to detect and count each membrane-bound H-Ras molecule (see Fig. 1.1 and Table 2.1). Functional analysis revealed the membrane-anchored H-Ras is active in PI3K α recruitment and kinase assays and exhibits the expected nucleotide specificity for activation by GTP or GTP analogue).

Single molecule TIRFM measurements. TIRFM experiments were carried out at $21.5 \pm 0.5^\circ$ C on an objective-based TIRFM instrument as described previously (77, 79). Supported bilayers were first washed with TIRF assay buffer (100 mM KCl, 20 mM HEPES pH 6.9, 15 mM NaCl, 5 mM glutathione, 2.0 mM EGTA, 1.9 mM Ca²⁺, 0.5 mM Mg²⁺, where this Ca²⁺/Mg²⁺ buffering system yields 10 μ M free Ca²⁺ and 0.5 mM free Mg²⁺), then imaged before and after adding a concentrated mixture of BSA and CHAPS to final concentrations 100 μ g/ml and 0.05%, respectively. After this addition, only a few dim, rapidly dissociating fluorescent contaminants were typically observed on the bilayer prior to protein addition and were easily eliminated from the data as described below. Occasionally, the contaminant level was excessive and the reagents (starting with the lipids) were remade.

Following confirmation of minimal contamination, stabilizers, proteins and ATP (1 mM) were added to the observation chamber as needed and were equilibrated 3 min. These added components included a low level of BSA (100 μ g mL⁻¹ BSA final) to block sticky surfaces that could adsorb the dilute proteins (81), and, where appropriate, CHAPS to prevent PI3K

aggregation (0.05% CHAPS), phospho-Tyr peptide for PI3K activation, guanosine nucleotide (1 mM) for maintaining H-Ras in its nucleotide-loaded state (in experiments employing this protein), and GRP PH domain (800 pM) as a PIP₃ sensor. Where needed, aliquots of PI3K were thawed on ice and diluted into stabilizing buffer that maximizes its stability (125 mM NaCl, 20 mM HEPES pH 7.2, 25% glycerol, 4 mM TCEP, 0.05% CHAPS, 100 µg mL⁻¹ BSA) until dilution into TIRF chamber containing assay buffer (see above).

To minimize contributions from small numbers of immobile unfolded proteins, a bleach pulse ~30-fold higher power than used for imaging was applied for ~10 s, then fluorescence was allowed to return to a steady state for at least 60 s before data acquisition. For each sample, a set of 2-4 movie streams were acquired at a frame rate of 50 frames/s, and a spatial resolution of 4.2 pixels/µm on the home-built instrument, using NIS Elements Basic Research (Nikon, Melville, NY).

Single molecule diffusion tracking. As in our previous studies (77, 79, 82), diffusion trajectories of single protein molecules were tracked and quantitated using the Particle Tracker plugin for ImageJ (83) yielding a per-frame quantitation of particle position and brightness. Then resulting data was then imported into Mathematica for further analysis. Only particles possessing fluorescence intensities within a defined range were included in the analysis, thereby eliminating bright fluorescent contaminants/protein aggregates and dim, non-protein contaminants. Additional displacement-based exclusions removed immobile particles, rapidly dissociating particles, and overlapping tracks for which particle identity is lost. All exclusions were described and validated previously (77, 79, 82).

PI3K membrane binding densities. To investigate the mechanisms of PI3K α activation by receptor-derived phospho-Tyr peptide (pYp) and/or membrane-anchored H-Ras, we employed our recently published single molecule methods to quantify the effects of activators on PI3K α surface density and lipid kinase activity (18, 71). Binding measurements

focused on stable PI3K α complexes bound to the membrane for at least 5 consecutive 20 ms movie frames, yielding tracks lasting ≥ 100 ms.

To quantify the average density of PI3K α on the membrane surface in a given TIRF movie, the number of single particle tracks (defined as described above) in a given field of view was determined for each movie frame, then averaged over all frames. Bleaching of individual tracks or the bulk population was not a major issue since the average residence time on the membrane prior to dissociation was short compared to the average bleach time; as a result, fluorescent proteins dissociate from the membrane before bleaching and are replaced from the bulk population which lies predominantly outside the TIRF excitation field. Under our experimental conditions, the average time-to-bleach of the Alexa 555 fluor was ≥ 20 sec (77, 79), which is at least 10-fold longer than the average bound state lifetime of any labeled protein in this study.

PI3K kinase activities. A single molecule kinase assay employed to quantifying PI3K α lipid kinase activity and PIP₃ production as previously described (18). The method counts all single molecules of product PIP₃ generated by the PI3K lipid kinase reaction, using a saturating concentration of fluor-tagged, GRP-PH domain (800 pM) to bind and detect each PIP₃ molecule generated on the membrane surface. After PI3K is added to the chamber (see Single Molecule TIRFM Measurements above), ATP (1 mM) was added from a buffered stock (assay buffer containing 100 mM ATP and 82.5 mM Mg²⁺) to start the kinase reaction. Subsequently, fluor-tagged PH domain tracks were quantified as previously described at 5 timepoints (18, 71). To determine the PI3K α specific activity, the resulting net rate of PIP₃ production is divided by the average density of PI3K α determined by the above binding assay (with appropriate correction for the PI3K fluorescence labeling efficiency).

Statistics. PI3K α is a large, 208 kDa heterodimeric enzyme with nine structural domains and retains function well when stored in frozen, single thaw aliquots. However, thawed aliquots

exhibit variability in activity that represent the major limitation on precision in studies of membrane binding, kinase activity, and specific activity. Thus, large numbers of replicates were carried out on multiple days to allow rigorous statistical analysis. Specifically, for each measured parameter, n means were determined, where each mean averaged 3+ replicates carried out on the same day. Error bars represent the standard error of these n means determined on 5–15 different days ($n = 5–15$).

RESULTS

Mimicking the cellular signaling pathway, and production of membrane-anchored H-Ras. The single-molecule approach enables use of near-physiological protein concentrations and target lipid densities designed to approximate those found in the cellular pathway. Thus, this study employed a PI3K α concentration (2 nM) of the same order as its physiological concentration (estimated 3 nM (37), together with a pYp level (saturating) to simulate PI3K α bound to the regulatory loop of its phospho-activated RTK receptor. The H-Ras coupling protocol yields a surface density of monomeric H-Ras (1 per μm^2 ; see Fig. 2.9; Table 2.1) ~30-fold lower than the surface density reported in cells (84, 85). However, the in vitro system presented here fully loads membrane-anchored H-Ras with GTP or non-hydrolyzable GTP analog, yielding a surface density of active, monomeric H-Ras similar to that expected for moderate H-Ras signals in cells where only a fraction of the membrane-anchored population is activated by GTP loading (86). Moreover, the specific kinase activity (turnover number) of PI3K α bound to pYp and H-Ras on the membrane surface is the same, within error, at different H-Ras surface densities (Figure 2.3). These findings are consistent with a simple picture in which, as the H-Ras surface density increases, the density of membrane-bound PI3K α and its net kinase activity increase linearly, whereas the specific activity of membrane-bound PI3K α remains unchanged because its activation mechanism is density independent. The

fluorescent GRP1 PH domain employed to detect PIP₃ molecules generated by PI3K α is present in the in vitro single-molecule kinase assays at levels (800 pM) sufficient to fully bind all product PIP₃ molecules, just as sufficient PH domain proteins are present in cells to bind all product PIP₃ (87). Finally, the supported bilayer densities of the anionic background lipid PS (mole fraction 25%) and the target-substrate lipid PIP₂ (mole fraction 1%) are similar to those estimated for the plasma membrane cytoplasmic leaflet (88, 89).

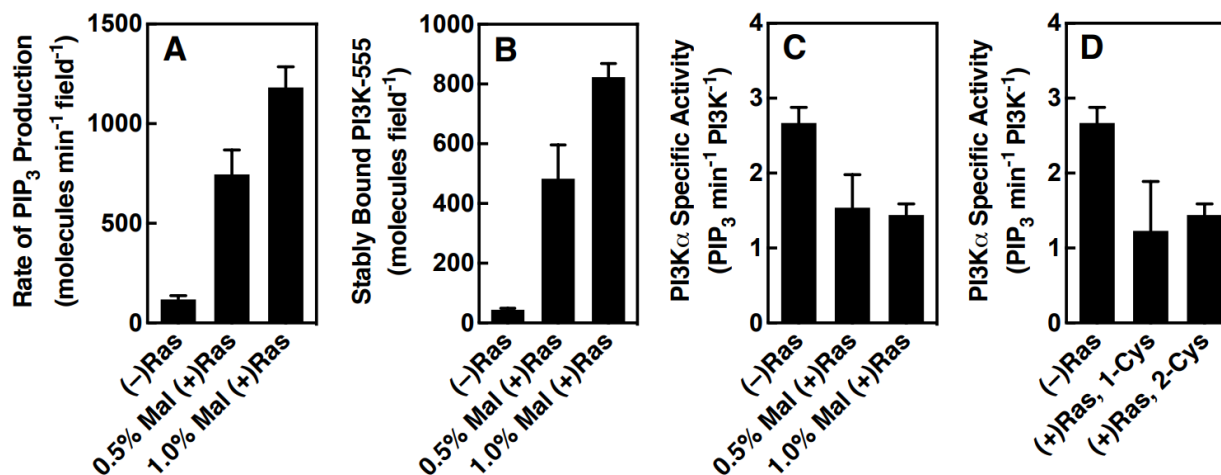


Figure 2.3. Synergistic phospho-Tyr peptide and H-Ras stimulation of PI3K α : Controls examining the dependence on H-Ras density and number of lipidation sites. Each single molecule TIRFM measurement included RTK-derived phospho-Tyr peptide (pYp) to generate basal PI3K α activation. (A,B,C) In all data reported in this study, H-Ras is coupled to membranes containing 1.0% maleimide lipid, except where noted as 0.5% maleimide lipid in these three panels. The H-Ras coupling to membranes containing maleimide lipid is carried out with ≥ 1000 fold mole excess H-Ras over maleimide for 5 min. When the density of maleimide lipid is reduced 2-fold, panels (A,B) show that the rate of PIP₃ production by PI3K α and the density of stably bound PI3K α decrease proportionally (within error). Thus, as panel (C) shows, the specific kinase activity of the average membrane-bound PI3K α molecule is the same on both membranes (within error). These data are consistent with a simple linear dependence of the net PI3K α membrane binding and kinase activity on the density of membrane-coupled H-Ras, while the kinase activation mechanism and specific activity in the membrane-bound state are independent of H-Ras density. (D) In all data reported in this study, 2-Cys H-Ras possessing two lipidation Cys residues (C181, C184) is coupled to membranes containing maleimide lipid, except where noted in panel (D) and Table 2.1 for 1-Cys H-Ras possessing a single lipidation Cys (C181, C184S). This panel shows that the specific kinase activity of the average membrane-bound PI3K α molecule is the same for 2-Cys H-Ras, which is coupled predominantly by both Cys residues (see Table 2.1), and for 1-Cys H-Ras coupled via a single Cys. **Methods.** Previously described single molecule TIRFM procedures were employed, as described in Methods and in our previous publications (2,3,5-8). Data at 22 °C are averages over 7-9 replicates on at least 2 days. Error bars are standard errors of the mean (A,B) or propagated standard errors of the mean (B,C).

Our previous single-molecule TIRFM studies have characterized the membrane binding and two-dimensional diffusion of the PI3K α and GRP PH domain proteins on supported bilayers, revealing that PI3K α possesses extensive bilayer contacts involving multiple lipids, whereas GRP PH domain binds a single PIP₃ and diffuses like a single lipid, since the lipid drag against the bilayer largely controls the diffusion speed. This study carries out the first single-molecule analysis, to our knowledge, of PI3K α regulation by H-Ras, employing a recently developed approach (78) to covalently anchor functional H-Ras to the supported lipid bilayer. The membrane coupling procedure targeted two native Cys residues that are located near the C-terminus of the hyper-variable region (HVR) (Figure 2.2) and are palmitoylated in native H-Ras, where they serve as plasma membrane anchors. Here, both of these Cys residues were employed as supported bilayer anchors by covalently coupling them to a maleimidyl-modified phospholipid headgroup.

Single-molecule TIRFM was used to characterize the density and diffusion speed of the maleimide-lipid-anchored H-Ras on the supported bilayer surface (Fig. 2.9; Table 2.1). The measured density was ~ 1 H-Ras/ μm^2 (Table 2.1). Analysis of the two-dimensional diffusion tracks revealed two subpopulations of membrane-anchored monomeric H-Ras with fast and slow diffusion speeds, corresponding to the frictional drag of one and two coupled lipids (77, 90), respectively (Table 2.1). The latter H-Ras subpopulation coupled to two lipids via C181 and C184 was found to be the larger, predominant subpopulation (Table 2.1). The resulting membrane-anchored H-Ras retains the native 14 residue, unstructured tether between membrane-anchored C181 and the folded GTPase domain (Figure 2.1 and 2.2)

Protein	Density (per μM^2)	D_{Fast} ($\mu\text{M}^2/\text{s}$)	Fraction Fast	D_{Slow} ($\mu\text{M}^2/\text{s}$)	Fraction Slow
H-Ras (2 Cys) GMPPNP ^{a,b}	0.8 ± 0.1	1.3 ± 0.1	0.26 ± 0.01	0.7 ± 0.1	0.74 ± 0.01
H-Ras (2 Cys) GMPPNP ^a	0.5 ± 0.1	1.7 ± 0.4	0.28 ± 0.05	0.7 ± 0.1	0.72 ± 0.05
H-Ras (2 Cys) GTP ^a	0.7 ± 0.3	1.9 ± 0.5	0.31 ± 0.25	0.4 ± 0.1	0.69 ± 0.03
H-Ras (2 Cys) GDP ^a	0.8 ± 0.2	1.3 ± 0.3	0.35 ± 0.03	0.4 ± 0.3	0.65 ± 0.02
H-Ras (1 Cys) ^a	0.8 ± 0.1	1.4 ± 0.1	1	-	-
GRP-PH-555	N.D.	1.6 ± 0.2	1	-	-

^a Detected by the binding of anti-H-Ras antibody labeled with Alexa Fluor 555

^b Same, but half the usual saturating concentration of antibody

Table 2.1. Controls comparing the surface densities and diffusion characteristics of different H-Ras nucleotide binding states and different numbers of coupled lipids. H-Ras loaded with the indicated nucleotide was covalently coupled to maleimide-PE lipid on supported bilayers. Individual molecules were visualized by the binding of fluor-tagged anti-H-Ras antibody, and 2D single molecule diffusion tracks were analyzed to determine the diffusion characteristics of the single molecule population. Some variation in H-Ras surface density is observed between experiments on different days, due to variability in the efficiency of maleimide-PE into the bilayer lipid mixture, and variability in the coupling efficiency of protein reacting with the maleimide headgroup. The 2 Cys H-Ras construct was used in all experiments in the main text and Supporting Materials, except where noted. This construct exhibits a major, slowly diffusing monomeric population coupled via both Cys 181 and 184 residues to two maleimide-PE lipids, as well as a minor, rapidly diffusing monomeric population coupled via a single Cys residue to one lipid (monomeric state defined by Fig. 2.9C-E). Comparison of H-Ras loaded with different nucleotides reveals no major differences between density or diffusion parameters, within the error of measurement: none of the observed differences are statistically significant. Specifically, the error bars overlap for all pairs of parameters measured for different bound nucleotides, with one exception: the error bars measured for the slow diffusion constants of H-Ras loaded with GMPPNP and GTP do not overlap, but the calculated p value (0.16) for this difference indicates it is not significant. Previous studies of 2-Cys H-Ras loaded with fluorescent GTP and GDP analogues also found that nucleotide substitution had no detectable effect on the brightness or diffusion of H-Ras monomers when light-induced dimerization was suppressed by the presence of reducing agent (9). All of our studies include a physiological level of the cytoplasmic reducing agent glutathione (5 mM); thus, as predicted (9), light-induced dimerization is not observed, and H-Ras is monomeric. The 1 Cys H-Ras construct possesses the C184S mutation, and thus retains only one Cys residue for membrane coupling. This 1 Cys construct exhibits a homogeneous diffusion within error of that observed for the fast component of the 2 Cys construct diffusion, confirming that both fast diffusers are monomeric H-Ras coupled to a single lipid. Moreover, both fast diffusers exhibit diffusion constants indistinguishable from that of PH domain bound to a single PIP₃; thus, as expected, monomeric proteins each bound to a single DO lipid exhibit the same diffusion speed defined by the frictional drag of the bound lipid (5). **Methods.** Saturating (40 nM) antibody was added to supported bilayers decorated with H-Ras coupled to maleimide-PE, using a 1:30 ratio of fluor-labeled to dark H-Ras to ensure countable densities of fluorescent H-Ras molecules. The same TIRFM procedures described in Methods and Figs. 2.3, 2.6, and 2.9 were employed, except that PH domain was imaged on supported bilayers containing 1 mole percent PIP₃ rather than PIP₂. Data are averages of 6+ replicates acquired on 2+ days, 22 °C.

Synergistic activation of PI3K α by receptor-derived phospho-Tyr peptide and H-Ras. To probe the activation of PI3K α lipid kinase, we employed our previously described single molecule TIRFM assay of lipid kinase activity (18, 71). This assay directly monitors the number of individual product PIP₃ molecules produced as a function of time by catalytically active, membrane-bound PI3K α (Fig. 2.4 A, B, C).

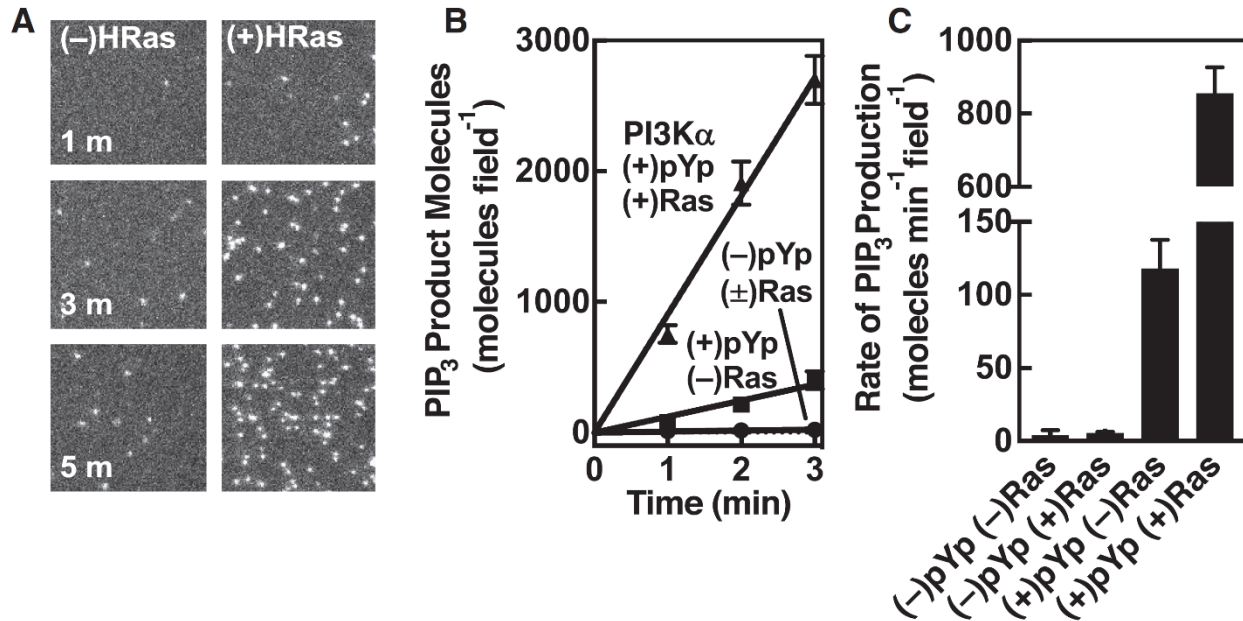


Figure 2.4. Effect of soluble phospho-Tyr peptide (pYp) and H-Ras on net PI3K α kinase activity and PIP₃ production. (A) TIRFM images of pYp-activated PI3K α lipid kinase activity on a target bilayer surface. Shown is the accumulation of product PIP₃ lipid detected by the fluor-labeled PIP₃ sensor (GRP PH domain), with and without membrane-anchored H-Ras. (B) Timecourse plotting the increasing number of PIP₃ molecules per field under four activating conditions, illustrating strong synergy between pYp peptide and H-Ras in activating PI3K α kinase and PIP₃ production. (C) The average slopes of these timecourses, yielding net rates of PIP₃ production, each generated from 3 replicates on each of 9+ different days (n = 27 to 36). (A,B,C) H-Ras is loaded with non-hydrolyzable GTP analogue GMPPNP.

Figure 2.4 reveals strong, direct synergy in PI3K α activation between phospho-Tyr peptide (pY peptide, or pYp) and membrane-bound H-Ras loaded with non-hydrolyzable GTP analogue. Notably, in the absence of pY peptide, H-Ras alone yields little or no activation

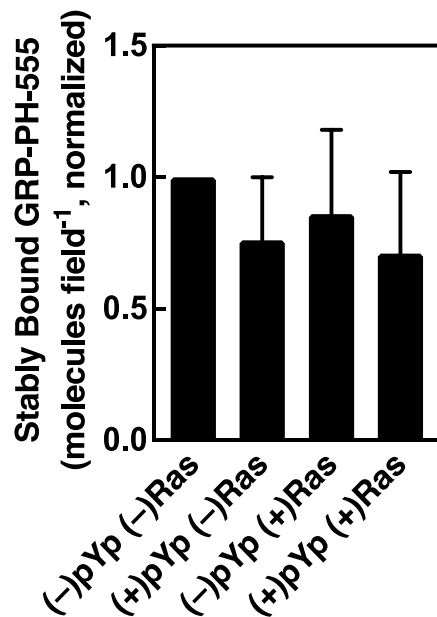


Figure 2.5. Controls examining the effects of PI3K activators on the binding of PH domain to PIP₃. Single molecule TIRFM was employed to quantitate the binding of the PIP₃ sensor employed in this study, Alexa Fluor 555-tagged GRP PH domain, to its target lipid. The presence of the PI3K activators RTK pYp and/or membrane-coupled H-Ras were found to have no significant effect on the density of PIP₃ sensor molecules on the supported bilayer surface. Thus, the effects of activators on PI3K α lipid kinase activity measured in the single molecule TIRFM assay (Figs. 2.4 and 2.6) can be attributed to the effects of the activators on the enzyme, rather than on PIP₃ sensor binding to product. Previously described single molecule TIRFM procedures were employed, as described in Methods and in our previous publications (2,3,5-8). Data are averages over 6 replicates on 2 days.

of PI3K α -catalyzed PIP₃ production. In contrast, saturating pY peptide alone triggers an approximately 30-fold increase ($p < 0.002$) in the net rate of PIP₃ production, indicating moderate PI3K α activation in the absence of H-Ras. Together, however, pY peptide and H-Ras synergistically speed net PIP₃ production nearly an order of magnitude (8 ± 2 -fold) ($p < 0.001$) relative to pY peptide alone, or approximately 200-fold ($p < 0.001$) faster than H-Ras alone. Controls show that the additional PI3K α activation triggered by H-Ras in the presence of pY peptide requires membrane-anchored H-Ras, is GTP-regulated, and is specific (Fig. 2.5).

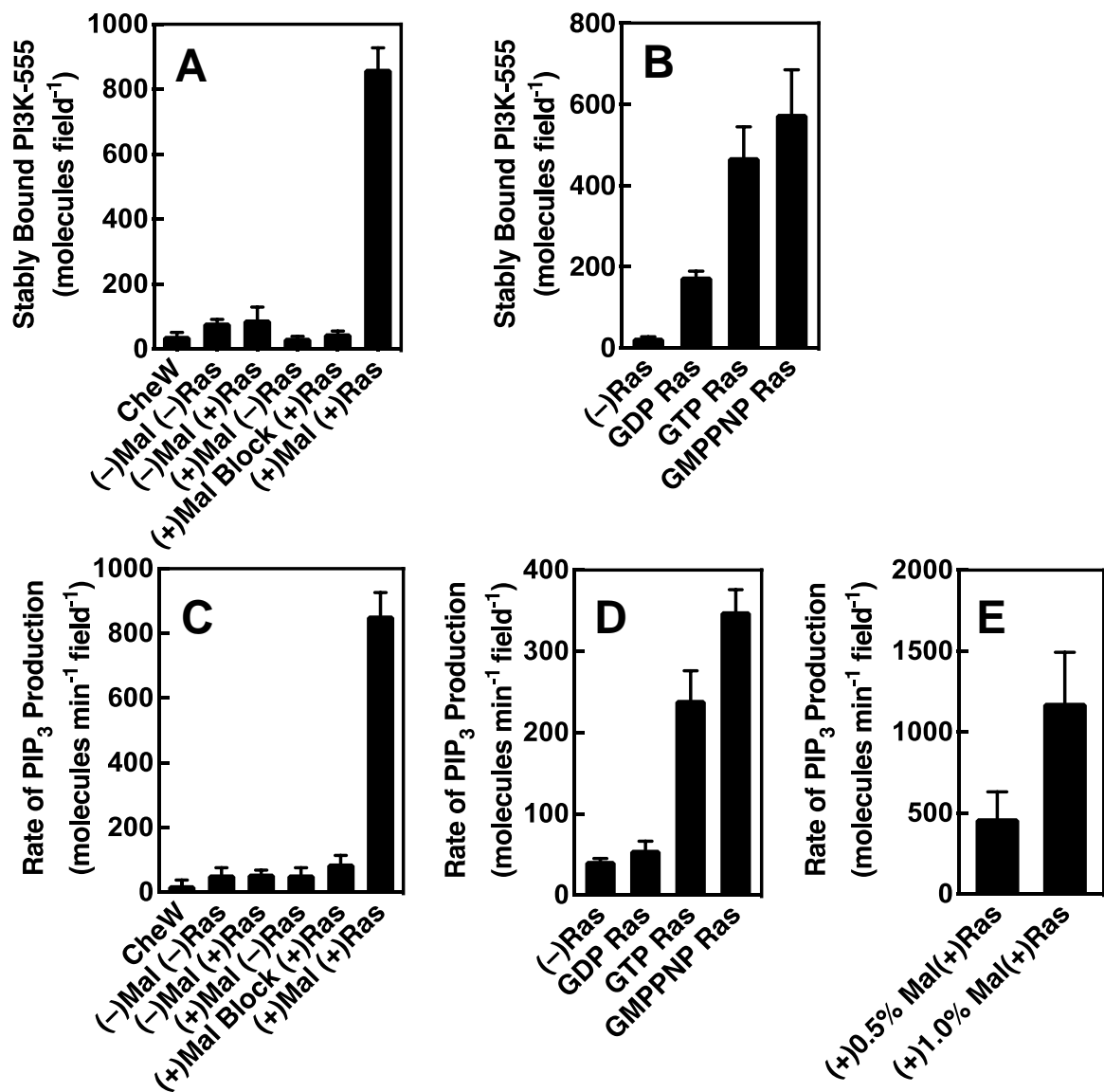


Figure 2.6. Synergistic phospho-Tyr peptide and H-Ras stimulation of PI3K α : Controls examining the H-Ras membrane anchoring and nucleotide requirements. Each single molecule TIRFM measurement included RTK-derived phospho-Tyr peptide (pYp) to generate basal PI3K α activation. **(A,C)** Synergistic PI3K α activation triggered by pYp and anchored H-Ras is lost when H-Ras coupling to the supported bilayer is prevented by (i) omission of maleimide lipid (Mal), or (ii) omission of H-Ras (Ras), or (iii) glutathione quenching of the maleimide lipid prior to H-Ras addition (Mal Block). Similarly, no additional PI3K α activation is observed when a different protein is coupled to the supported bilayer (CheW, a hydrophobic protein similar in size to H-Ras). **(B,D)** Synergistic PI3K α activation is lost when the membrane-anchored H-Ras is occupied by GDP, while GTP and non-hydrolyzable GTP analogue GMPPNP exhibit similar synergies. **(E)** When the mole density of maleimide-PE is reduced from 1% to 0.5%, the observed net PI3K α activity drops significantly ($p < 0.003$), consistent with a ~ 2 -fold reduction in H-Ras density and PI3K α membrane recruitment. Previously described single molecule TIRFM procedures were employed, as described in Methods and in our previous publications (2,3,5-8). Data at 22 $^{\circ}$ C are averages over 9-15 replicates on ≥ 3 days, except (E) is 6 replicates on 1 day.

Synergy dramatically increases the membrane density of stably bound PI3K α molecules. To investigate the unknown mechanism by which H-Ras dramatically amplifies the moderate PI3K α activation observed for pY peptide alone, we measured the effect of both activators on fluor-labeled PI3K α membrane binding and specific kinase activity.

Figure 2.7A shows that either pY peptide or H-Ras alone triggers moderate densities of long-lived PI3K α molecules on the membrane surface, while the two activators together exhibit strong synergy and dramatically increase the surface density of kinetically stable PI3K α complexes. Measurements focused on stable PI3K α diffusion tracks lasting ≥ 100 ms. Addition of saturating pY peptide increases the density of PI3K α 4 ± 2 -fold ($p < 0.001$) on supported bilayers lacking H-Ras, comparable to our recently published result on membranes of nearly identical lipid composition (18). Similarly, in the absence of pY peptide, supported bilayers possessing membrane-anchored H-Ras yielded 5 ± 2 -fold ($p < 0.001$) higher PI3K α surface density than bilayers lacking H-Ras. When both pY peptide and membrane-anchored H-Ras were present, the PI3K α surface density was 80 ± 30 -fold ($p < 0.001$) greater than in the absence of both activators, and 20 ± 2.5 -fold ($p < 0.001$) greater than pY peptide alone.

The strong synergy observed between pY peptide and H-Ras in driving increased equilibrium levels of PI3K α on the membrane surface arises both from faster formation of stable PI3K α membrane complexes and slower dissociation. Figure 2.8A shows that the apparent formation rates of stable PI3K α single particle tracks with bound state lifetimes exceeding 100 ms are the same, within error, for either activator alone. By contrast, relative to pY peptide alone, combined peptide and H-Ras greatly increases the formation rate of stable tracks 19 ± 5 -fold ($p < 0.008$) and reproducibly decreases their dissociation rate by a small but significant factor (1.4 ± 0.3 -fold, $p = 0.003$). Together these kinetic effects fully account for the 20 ± 2.5 -fold ($p < 0.001$) greater density of membrane-bound PI3K α observed when pY peptide and H-Ras act synergistically.

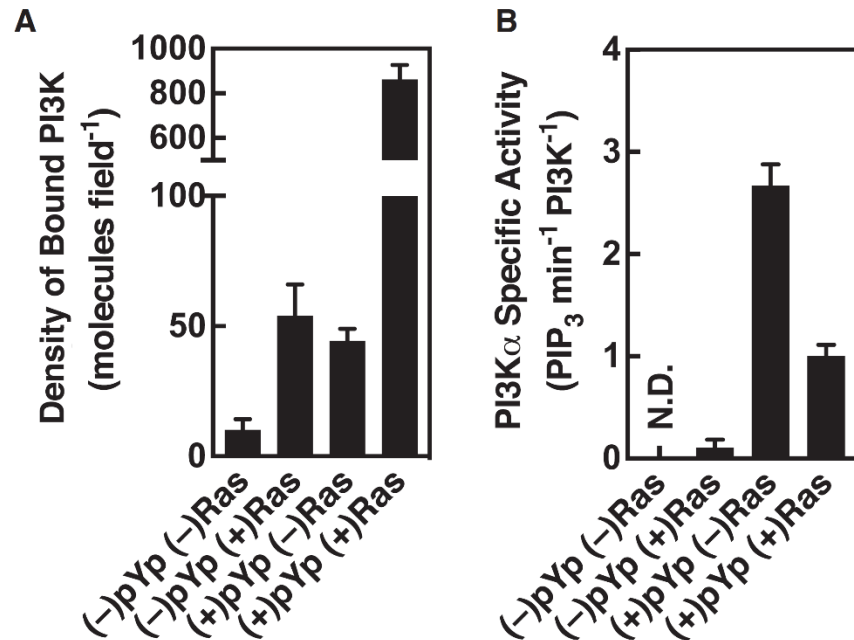


Figure 2.7. Effect of pYp and H-Ras on PI3K α membrane recruitment, and on the specific kinase activity of the membrane-bound enzyme. (A) Surface density of fluor-labeled PI3K α measured by single molecule TIRFM under the indicated activation conditions, generated from 3 replicates on 5 different days ($n = 15$). (B) Specific activity of membrane-bound PI3K α under each activating condition, calculated as the ratio of net PIP₃ production (2C) to the kinase surface density (3A). This specific activity ratio could not be determined for the (-)pYp (-)Ras condition due to the low density of kinase on the bilayer surface. (A,B) H-Ras is loaded with non-hydrolyzable GTP analogue GMPPNP.

Synergy slightly decreases the specific activity of membrane-bound PI3K α

molecules. Surprisingly, while pY peptide and membrane-anchored H-Ras synergize to increase the density of stably bound PI3K α molecules on the supported bilayer surface, this synergy decreases the specific lipid kinase activity of the membrane-bound enzyme. Figure 2.7B presents specific lipid kinase activities calculated by ratioing the rate of PI3K α -catalyzed PIP₃ production to the surface density of PI3K α (Figs. 2.4B, 2.7A). The specific kinase activity of the average membrane-bound PI3K α molecule activated by pY peptide and H-Ras together is, unexpectedly, 2.6 ± 0.6 -fold ($p < 0.001$) lower than observed for activation by pY peptide alone, indicating that the formation of the complex with H-Ras slightly but significantly inhibits the catalytic activity of membrane-bound, pYp-activated PI3K α . Overall, the findings reveal that

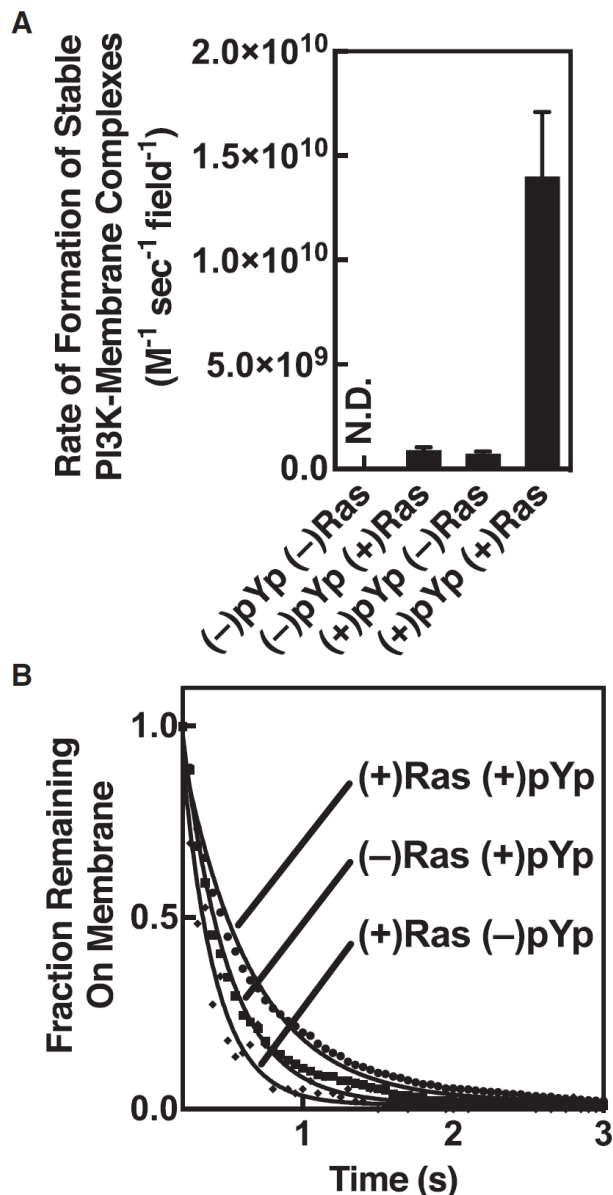


Figure 2.8. Effect of pYp and H-Ras on PI3K α association-dissociation kinetics. (A) Relative appearance rates of stable, fluor-PI3K α single particle diffusion tracks were measured under different activating conditions. These appearance rates were used to calculate the formation rate of active, stably bound PI3K α complexes on the membrane surface as follows. The number of PI3K α tracks with bound state lifetimes exceeding 100 ms in a TIRFM movie was determined, then divided by movie time and PI3K α concentration. Each rate was generated from movies acquired for 3 replicates on 5 different days ($n = 15$). **(B)** Off-rates of fluor-PI3K α from the membrane surface, calculated by binning the bound state lifetimes of PI3K α single particle diffusion tracks and fitting with a single-exponential decay. Each decay curve was generated from movies acquired for 3 replicates on 5 different days ($n = 15$). The resulting exponential decay constants were: $2.9 \pm 0.6 \text{ s}^{-1}$ for (-)pYp (+)Ras, $2.5 \pm 0.6 \text{ s}^{-1}$ for (+)pYp (-)Ras, and $1.9 \pm 0.2 \text{ s}^{-1}$ for (+)pYp (+)Ras. No kinetic data could be obtained for (-)pYp (-)Ras due to its very low density on the bilayer surface. (A,B) H-Ras is loaded with non-hydrolyzable GTP analogue GMPPNP.

the 8 ± 2 -fold ($p < 0.001$) faster net PIP_3 production observed for synergistic pY peptide and H-Ras activation, relative to pY peptide alone, arises from both the 20 ± 2.5 -fold ($p < 0.001$) greater PI3K α membrane recruitment noted above, combined with the 2.6 ± 0.6 -fold ($p < 0.001$) slower specific kinase activity. Notably, H-Ras alone yields moderate levels of PI3K α surface density but fails to generate any detectable kinase activation. Thus, both in the absence and presence of H-Ras (18, 29, 66, 71), pY peptide plays an essential role in making PI3K α competent for lipid association and stimulating lipid kinase activity. These results fully support the current view that association of receptor phospho-Tyr residues with the inhibitory SH2 domains of the PI3K p85 regulatory domain is required to make the p110 catalytic domain accessible for PIP_2 binding and catalysis. The observation that H-Ras slightly inhibits the specific kinase activity of pYp-activated PI3K α emphasizes that the contribution of H-Ras to synergistic G protein-receptor activation arises purely from a membrane recruitment mechanism, with no contribution from an enzyme activation mechanism.

DISCUSSION

The present findings show a strong, direct synergy between a soluble phospho-Tyr peptide (pY peptide or pYp) and membrane-anchored H-Ras in activating net PIP_3 production by PI3K α lipid kinase. The implications of these findings for the molecular mechanism of H-Ras synergy are especially applicable to synergy with soluble PI3K phospho-Tyr activators, such as Gab and IRS-1, due to the soluble nature of pYp in our experimental setup. Previously, synergy between phospho-Tyr and Ras activation of specific PI3K isoforms, including PI3K α , has been proposed by studies in cells, where it is difficult to rule out indirect synergies arising from multi-pathway activation (29, 58). A recent *in vitro* study observed direct, synergistic activation of PI3K kinase activity by simultaneously added pY peptide and H-Ras (53). Notably, however, this

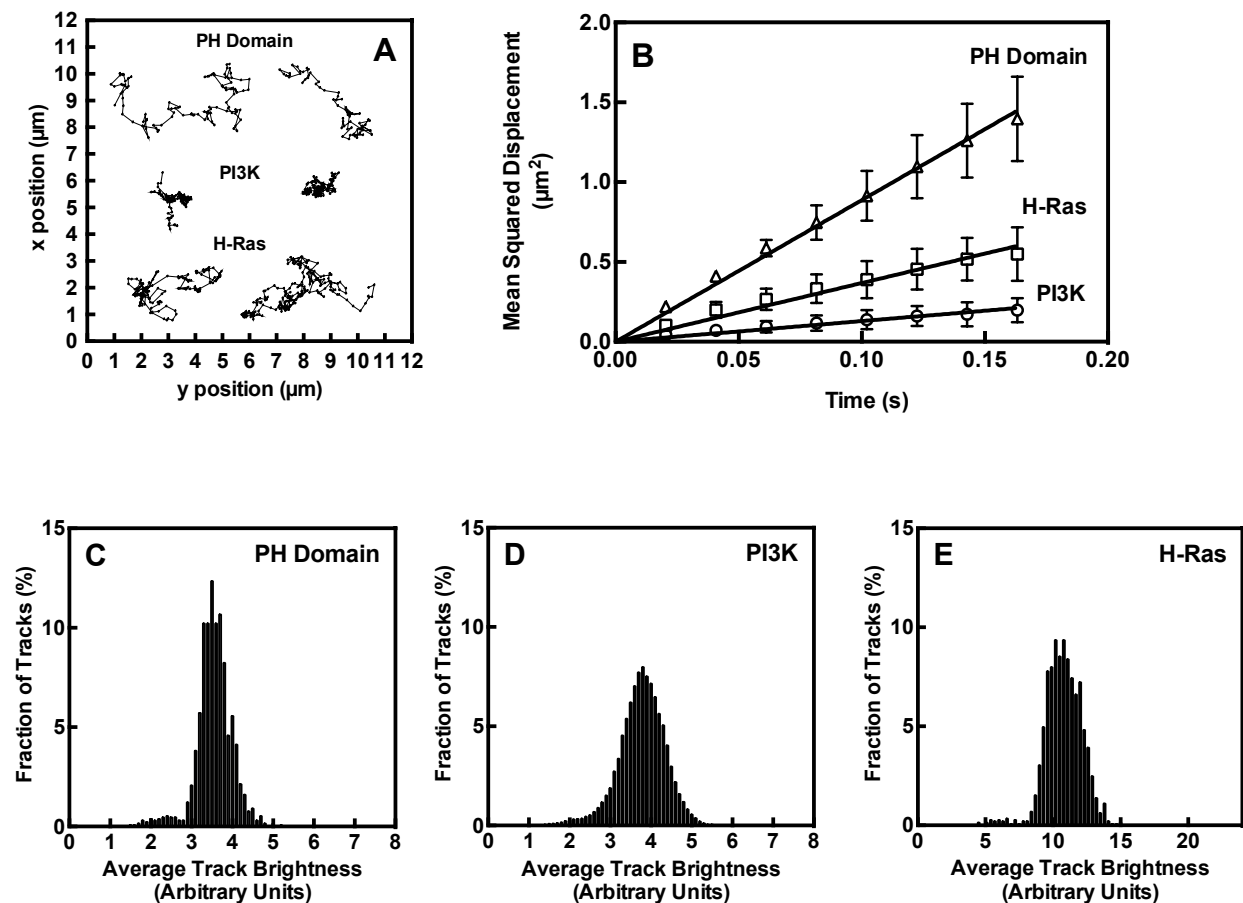


Figure 2.9. Detecting and quantifying single protein molecules diffusing in 2-dimensions on the target supported lipid bilayer. (A) Single molecule TIRFM reveals individual, fluor-tagged molecules diffusing in two dimensions on the supported bilayer surface. GRP-PH domain and PI3K are covalently tagged with Alexa Fluor 555 for visualization, while H-Ras (2-Cys construct, see Table 2.1) is detected by the binding of fluor-tagged anti-H-Ras antibody. (B) Mean square displacement (MSD) plots of the single molecule diffusion data for populations of each protein. (C-E) Relative brightness distributions for populations of each protein, where brightness of a protein is averaged over its track lifetime. Units are arbitrary but are normalized in the same fashion. The 3-fold greater brightness of H-Ras is due to the presence of three fluors, on average, covalently coupled to surface Lys residues on each anti-H-Ras antibody. In contrast, the PH domain and PI3K each possess a single fluor coupled to their Sfp labeling tag. **Methods.** Rabbit anti-Ras antibody (ab69747) was obtained from Abcam and labeled using excess AlexaFluor-555 succinimidyl ester via a standard procedure (5). Free fluorophore was removed by buffer exchange in Vivaspin 500 spin concentrators (30k MWCO). Unless indicated otherwise, standard supported lipid bilayers were employed as target membranes in all experiments. These bilayers were composed of four lipids, DOPE : DOPS : DOPIP₂ : DOPE-MCC in mole ratios 73:25:1:1. TIRFM procedures employed to track single particles, analyze 2D diffusion, and quantitate brightness distributions are described in Methods and in our previous publications (2,3,5-8). Data in B-E are averages over 4 replicates acquired on 2 or more days, 22° C. This figure provided by Dr. Brian Ziemba.

study did not quantify the effect of activators on PI3K membrane density, nor on the specific kinase activity of the membrane-bound enzyme, thus it was not able to resolve the membrane recruitment and enzyme activation models for the mechanism of synergistic activation.

The present findings reveal that H-Ras contributes to synergistic PI3K α activation via a membrane-recruitment mechanism. Relative to pY peptide alone, H-Ras interactions both speed the formation of kinetically stable, membrane-bound pYp-PI3K α complex by a factor of 19 ± 5 -fold ($p < 0.008$), and slightly but significantly slow the dissociation of PI3K α from membrane by 1.4 ± 0.3 -fold ($p = 0.003$). The enzyme activation model proposes that activation of PI3K α by H-Ras and other Ras isoforms could arise from increased specific kinase activity of the membrane-bound enzyme (20, 51). Surprisingly, binding to H-Ras is observed to significantly decrease, rather than increase, the specific kinase activity of the membrane-bound pYp-PI3K α complex. Thus, the H-Ras contribution to synergistic PI3K α activation arises purely from its ability to dramatically increase the surface density of active lipid kinase. Notably, H-Ras alone drives only a modest increase in PI3K α surface density and triggers no measurable kinase activation, reiterating the known requirement for receptor phospho-Tyr binding to the PI3K inhibitory SH2 domains to make the enzyme competent for bilayer and PIP₂ binding, as well as catalytic activity (18, 29, 66, 71).

Figure 2.10 (A,B) present the simplest kinetic scheme, and the corresponding reaction coordinate free energy profile, able to explain the observed kinetic and thermodynamic contrasts between PI3K α activation by the two activators, alone and in synergy. The phospho-Tyr peptide, pYp, first binds to the SH2 domains of the free kinase (I), triggering a conformational change that displaces the inhibitory SH2 domains from the catalytic subunit, thereby activating the lipid binding surfaces of PI3K α (18, 29, 66, 71) to yield the docking competent free kinase (II) (Fig. 2.10 A). The pYp-PI3K α complex is then hypothesized to bind via an electrostatic mechanism to the anionic membrane surface, where negative charge is provided mainly by PS, yielding a transient, weakly bound surface state (III). This transient

state (III) is hypothesized to undergo 2D diffusion (analogous to the electrostatic surface search of PH domains for PIP₃ (28) on the membrane surface. Usually it dissociates, but sometimes it binds PIP₂ and penetrates more deeply into the bilayer to yield a stably bound, kinase-active state (IV). In the presence of H-Ras, the pYp-PI3K α complex can encounter and bind H-Ras, either via its free state in solution (II) or via its transient surface state (III). The resulting binding of pYp-PI3K α to both H-Ras and the membrane surface, in quasi-stable state (V), prevents the rapid dissociation of transient state (III) from the membrane. Moreover, the H-Ras-bound surface state (V) is proposed to catalyze the transition to the more deeply penetrating, stable, kinase-active state bound to PIP₂ (VI), thereby speeding the formation rate of this stable, active state. Thus, the pYp and H-Ras activators act together in synergy to create a pathway to the stable, active state with lower activation barriers and enhanced thermodynamic stability, as illustrated by comparing the synergistic path (I)-(II)-(III)-(V)-(VI) to the pYp only path (I)-(II)-(III)-(IV) in Figure 2.10 B. Notably, the net stabilization of the final H-Ras-pYp-PI3K α -PIP₂ complex (path (I) to (VI)) is less than expected for simple additive stabilization by membrane and H-Ras binding (path (I) to (IV), plus path (III) to (V)). This observation suggests that the interaction between H-Ras and PI3K α in the H-Ras-pYp-PI3K α -PIP₂ complex perturbs the optimal PI3K α bilayer docking geometry achieved in the pYp-PI3K α -PIP₂ complex lacking H-Ras (5). Additional evidence for this perturbation is the lower specific kinase activity of the H-Ras-pYp-PI3K α -PIP₂ complex relative to the pYp-PI3K α -PIP₂ complex.

Overall, the findings provide important mechanistic insights into the receptor-Ras synergy that strongly activates PI3K in leukocyte chemotaxis, innate immunity, and inflammation, as well as in carcinogenesis. These insights also have implications for drug design targeting PI3K-catalyzed PIP₃ production in carcinogenesis or inflammation. The findings suggest that drugs designed to block activation of the PI3K SH2 domains by receptor phospho-Tyr residues will provide the strongest PI3K inhibition, since phospho-Tyr occupancy

of the SH2 domains is required for kinase activation by receptor alone, or by synergistic receptor-Ras activation. On the other hand, the findings indicate that drugs designed to block the interaction between H-Ras and PI3K should provide nearly the same degree of PI3K inhibition, since H-Ras dominates the synergistic activation. Moreover, the findings alleviate the prior concern that drugs targeting the Ras binding domain of PI3K might prevent Ras binding but inadvertently activate PIP₃ production via allosteric upregulation of the PI3K active site, since H-Ras binding to the PI3K α Ras binding domain actually inhibits, rather than activates, the PI3K enzyme. Further studies will ascertain whether the same activation and synergy mechanism observed for the H-Ras/PI3K α regulatory pair pertain to all G protein-PI3K pairings, or whether specialized activation mechanisms exist for specific PI3K isoforms interacting with specific G proteins, which include members of the Ras family, Rho family, and G $\beta\gamma$ family.

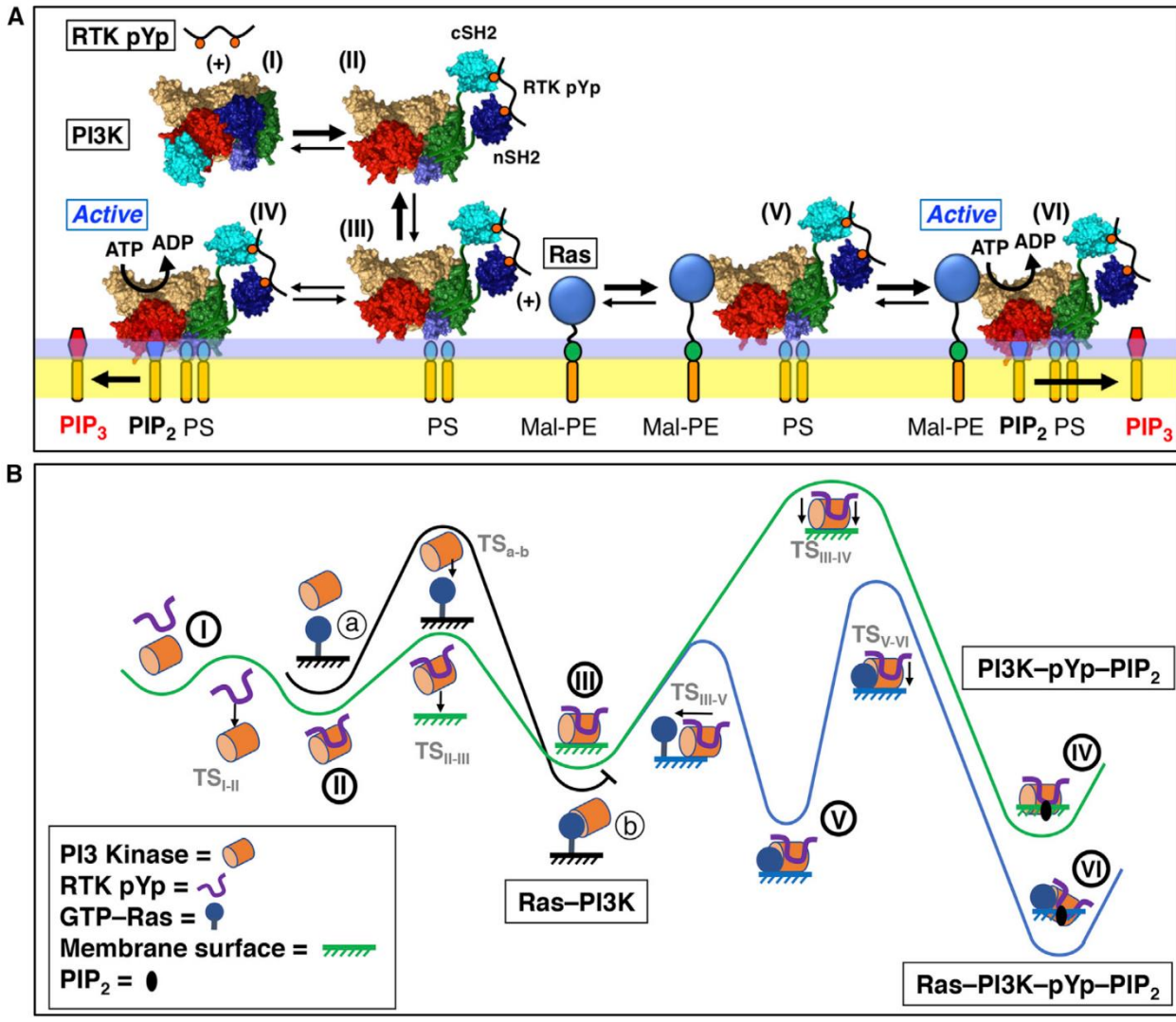


Figure 2.10. Working model for the mechanism of synergistic PI3K α activation by receptor-derived phospho-Tyr peptide and H-Ras. (A) Kinetic scheme showing schematic structural cartoons for each state in the hypothesized multi-step activation reaction, with dominant rates highlighted in bold. Activation begins with the binding of free PI3K α in solution (I) to the receptor-derived phospho-Tyr peptide (RTK pYp), present in excess. One or both inhibitory SH2 domains bind pYp and dissociate from the PI3K α catalytic domain, making it competent for moderate levels of PIP₂ binding and lipid kinase activity (65, 66). The resulting free pYp-PI3K α complex (II) docks to the membrane, yielding an inactive pYp-PI3K α complex transiently bound to the membrane surface in a shallow surface-bound state (III). This transient surface complex (III) rapidly dissociates and returns to solution (II) unless converted to a stable, membrane-bound, pYp-PI3K α complex by additional membrane interactions, such as deeper penetration into the bilayer (IV). The resulting stable, membrane-bound pYp-PI3K α complex (IV) is fully active and displays the maximum specific kinase activity. Alternatively, if present, membrane-anchored H-Ras can rapidly bind to the transient surface complex (III) and catalyze its conversion to the stably-bound Ras-pYp-PI3K α complex (V). Such catalytic assistance explains the faster rate of formation of the Ras-bound stable complex (V) compared to Ras-less stable complex (IV). Notably, the Ras-bound complex (V) exhibits two unexpected properties,

leading to the hypothesis that Ras binding perturbs the optimal membrane docking geometry displayed by pYp-PI3K α in the Rasless complex (IV). First, the rate of Ras-bound complex (V) dissociation from membrane is only slightly slower than that of Rasless complex (IV), indicating that the former complex does not possess the full kinetic stability expected for simple additivity of the binding free energies for pYp-PI3K α binding to H-Ras plus pYp-PI3K α binding to membrane. Second, the specific kinase activity of the Ras-bound complex (VI) is significantly lower than that of the Rasless complex (IV). These unexpected features are both consistent with a Ras-bound state (VI) in which structural constraints prevent the optimal interactions of pYp-PI3K α with Ras, and with the membrane (see text). **(B)** Reaction coordinate depiction of the kinetic scheme, using the same numbering scheme for intermediates (I) through (VI). Also shown is the unproductive path a to b for the absence of pYp, wherein PI3K α is able to bind weakly to Ras, but the lack of phospho-Tyr binding ensures the inhibitory SH2 continue to block PI3K membrane binding and kinase activation.

Chapter III:

The Leading Edge Pseudopod of Leukocytes: Rapid Exposure to Specific Therapeutic Drugs Triggers Pseudopod Collapse Followed by Recovery

ABSTRACT

Leukocyte migration is controlled by a membrane-based chemosensory pathway located on the pseudopod spanning the leading edge of the polarized cell. This pathway guides cell movement up attractant gradients during the innate immune response. Many drugs that block inflammation or pain are designed to inhibit inflammatory attractant release or to suppress pain signals, while retaining normal leading edge pseudopod function and innate immunity. The present study investigates the effects of four such drugs, at their clinical concentrations, on the leading edge pseudopod of cultured, polarized macrophages. The findings reveal that rapid or slow addition of two therapeutics (either acetylsalicylic acid or diclofenac) has no detectable effect on the pseudopod. In contrast, rapid addition of two other drugs (either ibuprofen or acetaminophen) causes temporary collapse of the pseudopod and its signature PIP₃ lipid signal, followed by adaptation and recovery. No such collapse is observed upon gradual addition of either drug. The findings demonstrate the utility of an in vitro assay to identify drugs that perturb the leading edge pseudopod, as well as drug perturbations likely to be alleviated by gradual drug administration. Moreover, the findings for a small group of four test drugs raise the possibility that many therapeutics could have perturbing effects on leukocytes, particularly when administered more rapidly than leukocyte adaptation can accommodate, with potentially inhibitory effects on innate immunity.

INTRODUCTION

Leukocytes, including macrophages and neutrophils, possess a sophisticated chemosensory system that controls cellular migration up primary attractant gradients to sites of infection, injury, or tumor formation during the innate immune response (2, 91-97). At the target site, recruited leukocytes and other cells release secondary attractants that recruit additional leukocytes as needed, but excessive secondary attractant signaling and recruitment can lead to local inflammation and, in extreme cases, toxic effects including tissue damage (reviewed in ((98-102)). The chemosensory pathway that directs leukocyte migration up primary and secondary attractant gradients is located on the single, large pseudopod at the leading edge of the polarized cell, where pathway components assemble on the cytoplasmic leaflet of the plasma membrane (reviewed in (9, 10, 92-94, 98, 103)). Drugs designed to reduce inflammation typically block cyclooxygenase enzymes (COX) that synthesize a major precursor of inflammatory attractant signals (reviewed in (104-106)). Ideally, such anti-inflammatory drugs block secondary attractant release but do not block the leukocyte chemosensory pathway, thereby maintaining a normal innate immune response in which the leading edge pseudopod continues to guide leukocyte migration to infections, wounds and tumors.

The leukocyte leading edge pseudopod and its chemosensory pathway is highly specialized, conferring unique properties to leukocyte chemotaxis not observed in other cell types. In particular, the leukocyte pathway possesses a positive feedback loop that maintains the stability and ruffling activity of the leading edge pseudopod even in the absence of an attractant gradient, enabling the pseudopod to rapidly detect and migrate up a new gradient as it appears (8, 18, 19, 71, 92, 93, 103, 107-111). The feedback loop is comprised of multiple essential second messengers, signaling proteins, and cytoskeletal elements including: Ca²⁺; phosphoinositide-3- kinase (PI3K); protein kinase C (PKC); small G-proteins (Ras, Rac); phosphatidylinositol-3,4,5- trisphosphate (PIP₃); and actin filaments (5, 8, 18, 19, 71, 91, 96,

103, 107, 108, 110, 112-123). Activation of any loop component leads to a characteristic co-activation of other loop components, expansion of the leading edge pseudopod, and increased accumulation of leading edge PIP₃. By contrast, inhibition of any loop component yields inactivation of other loop components, contraction of the pseudopod, and decreased PIP₃ levels. Another characteristic feature is an adaptation mechanism that damps out constant, background attractant levels enabling sensitive detection of attractant gradients even when superimposed on a complex chemical environment that may include uniform background signals.

The present study employs single cell and population observations of polarized RAW macrophages in culture to identify drugs that perturb the leading edge pseudopod. Since the pseudopod is easily visualized in live, cultured leukocytes by differential interference contrast microscopy (DICM) and by fluorescence microscopy (8, 115), it is possible to directly identify both inhibitory and activating drugs that perturb the pseudopod and its chemosensory pathway.

The study examines four representative, widely employed therapeutic drugs at their standard clinical dosages (124-130). Three are non-steroidal anti-inflammatory drugs (NSAIDs) commonly used to relieve both inflammation and pain: acetylsalicylic acid (aspirin), ibuprofen and diclofenac. The fourth, acetaminophen, is not an NSAID and relieves pain via unknown mechanisms. Also investigated are three control drugs with known effects on the leading edge signaling pathway at their standard experimental concentrations (8, 46, 115, 131-134): platelet derived growth factor (PDGF-ββ), an activator that is a strong macrophage attractant; wortmannin, a covalent suicide inhibitor that blocks the lipid kinase phosphoinositide-3-kinase (PI3K) responsible for synthesizing PIP₃; and Go6976, a reversible inhibitor that blocks protein kinase C (PKC). It is anticipated that the ability of these drugs to perturb the pathway may fall into at least four categories: (i) transient inhibition of the pathway followed by recovery, or (ii) long-term inhibition of the pathway with little or no recovery, or (iii) no detectable effect on the

pathway, or (iv) activation of the pathway.

The findings reveal that of the four tested therapeutic drugs, acetylsalicylic acid and diclofenac have little or no detectable effect on the macrophage leading edge pathway and pseudopod. In contrast, rapid (entire dose added at $t = 0$), but not slow (25% of dose applied 4x over 1.5 hours), addition of ibuprofen or acetaminophen temporarily inhibit the pathway, yielding short-term collapse of the leading edge pseudopod and loss of the key leading edge second messenger lipid PIP_3 . Longer term observations show that perturbed macrophages are able to adapt to the latter two drugs, eventually allowing virtually full recovery of the macrophage population. Such adaptation helps explain why all four therapeutic drugs, including those that trigger an initial pseudopod collapse in vitro, are well-established as safe, non-toxic drugs when used in the clinic at their standard dosages (124-130, 135). In contrast, the two non-clinical inhibitors (wortmannin, Go6976), which are predicted to block innate immunity (136, 137), yield rapid collapse of the leading edge pseudopod with little or no recovery within three hours. Overall, the findings demonstrate that an in vitro assay designed to measure the effects of therapeutic drug addition on the leading edge pseudopod of cultured leukocytes can be useful in classifying drugs with respect to their potential to perturb the pseudopod, and the ability of the pseudopod to adapt to such perturbation.

MATERIALS AND METHODS

Reagents. RAW 264.7 cells (Lots 70000171, 70012232) were obtained from the American Type Culture Collection (ATCC, Manassas, VA). Cell media (supplemented DMEM) was composed of DMEM obtained from Thermo Fischer Scientific (Waltham, MA), fetal bovine serum (FBS) from Millipore-Sigma (St. Louis, MO), penicillin, streptomycin and GlutaminePlus (L-alanyl-L-glutamine) from Atlanta Biologicals (Flowery Branch, GA). Dulbecco's phosphate buffered saline (D-PBS) was from Gibco (Gaithersburg, MD). Matriplate 96 well imaging plates

were from Matrical, Inc. (Spokane, WA). Acetylsalicylic acid, ibuprofen, acetaminophen, diclofenac, wortmannin, β bb, and HEPES (free acid) were obtained from Millipore-Sigma (St. Louis, MO). Go6976 was purchased from Tocris Biosciences (Minneapolis, MN). CellMask Deep Red and Green membrane stains were purchased from ThermoFischer Scientific (Waltham, MA). Cell-culture grade DMSO was purchased from MP Biomedicals (Santa Ana, CA). AKT-PH-mRFP mammalian expression plasmid was subcloned by John H. Evans (8, 115). Cell Culture and Transfections. Cell culture techniques used herein have been previously described (8, 115). Briefly, starting from cryogenic stocks, RAW 264.7 macrophages were grown at 37°C under 5% CO₂ in supplemented DMEM media containing 2 mM GlutaminePlus, 20 mM HEPES pH 7.2 with NaOH, 100 U/mL penicillin, 100 µg/mL streptomycin, and 10% FBS. Cells were washed in D-PBS pH 7.2 with HCl and passaged upon reaching ~80% confluency, as recommended by ATCC. Single cell or population experiments used RAW cells following at most 14 or 5 such passages, respectively.

Cell Imaging and Analysis. Live-cell microscopy methods have been previously described (8). Cells were counted by hemocytometer and plated at known density in 96 well imaging plates, then subsequently incubated at 37°C under 5% CO₂ for ~24 hours to facilitate cell adhesion and generate conditions of steady state cell polarization. In the bottom of each well, cells attach to a flat glass surface and spontaneously polarize in the absence of an attractant gradient. Two microscopes were employed. (i) Images for Fig 3.1 (except C,D) and Fig 3.6 were captured using a Nikon TiE microscope equipped with a 40x, 0.95 N.A. objective and a Hamamatsu ORCA-Flash 4.0 V3 Digital CMOS camera. (ii) Images for Figs 3.2 and 3.4 were acquired with a Nikon TiE spinning-disc confocal microscope equipped with a Yokogawa CSUX1 scanning unit, an Andor iXon 888 EMCCD camera, and a 60x, 1.3 N.A. water-immersion objective (Fig 3.2) or a 40x, 0.95 N.A. objective (Fig 3.4). For both microscopes, the imaging stage was enclosed in an environmental chamber maintaining humidity, 5% CO₂, and 37° C.

Imaging studies monitored a single cell, or a population of cells, following the addition of a drug or control carrier (DMSO or supplemented DMEM). Two types of addition protocols were employed. In rapid addition the drug or carrier was added (0.5 μL into 500 μL) at $t = 0$ to its final concentration with immediate, gentle pump-mixing. In slow addition the drug or carrier was added in four equal increments (each 0.25 μL into 500 μL) together yielding the final concentration at $t = 0, 30, 60, 90$ min followed by immediate, gentle pump-mixing. Final drug concentrations were PDGF- $\beta\beta$ 2.1 μM , wortmannin 500 nM, Go6976 1.0 μM , acetylsalicylic acid 1.1 mM, diclofenac 17 μM , ibuprofen 240 μM , acetaminophen 170 μM . All drugs were added in DMSO with the exception of PDGF- $\beta\beta$, which was added in supplemented DMEM. Previously described procedures were employed to capture and analyze single-cell timecourses (Fig 3.2) for individual, polarized cells with extended, actively ruffling leading edge pseudopods (28). Briefly, for each cell the value of the initial $t = 0$ timepoint was used to normalize all timepoints. Subsequently, for a group of at least 3 cells in an experiment carried out on the same day, corresponding normalized timepoints were averaged to generate a mean value for each timepoint. Finally, the resulting mean timepoints for individual experiments were averaged over all experiments to generate a global mean and its standard error of the mean (SEM) for $N =$ the number of experiments. Final global averages represented 17 - 32 total cells imaged in at least 3 experiments on at least 3 separate days for experimental treatments, or 9 -

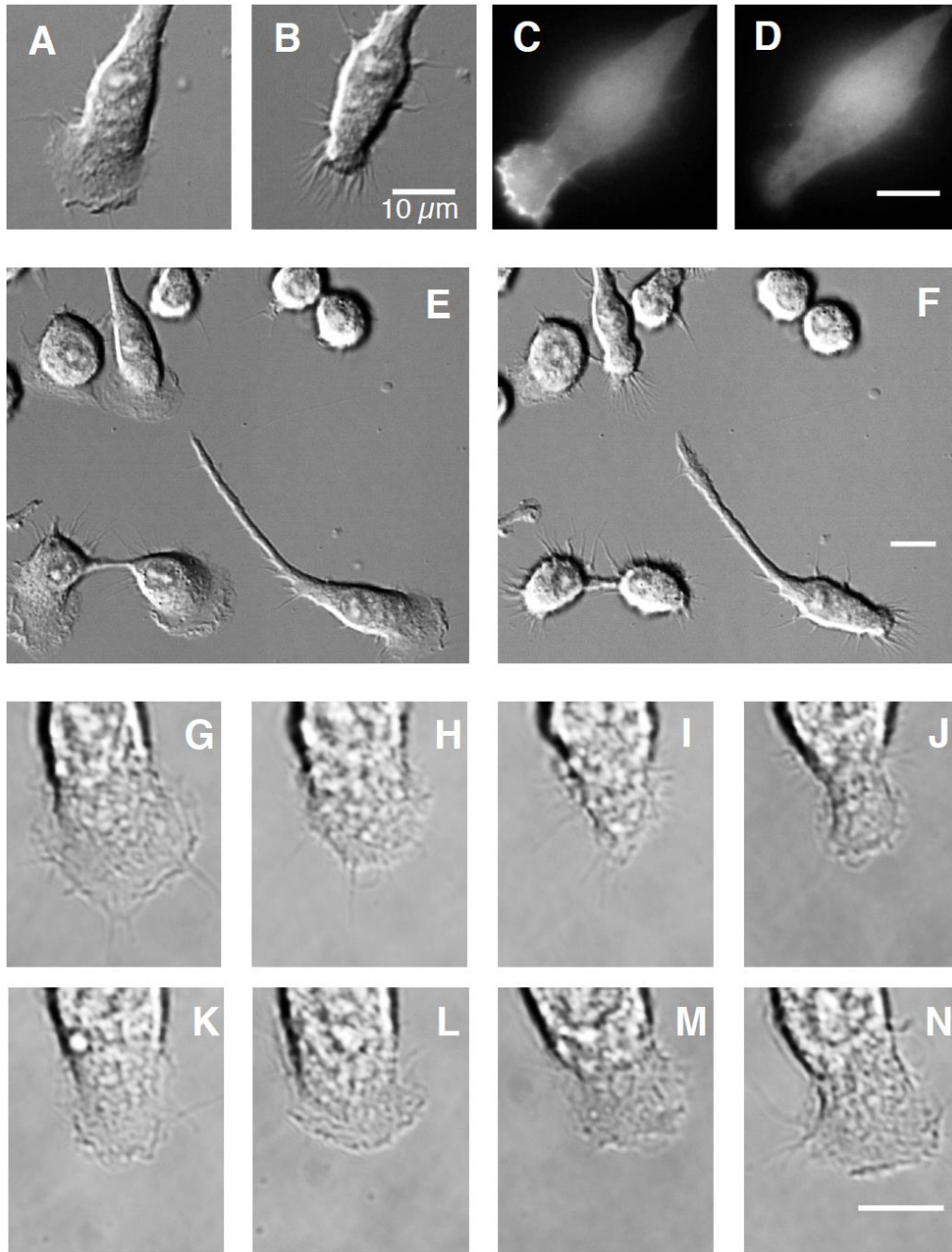


Figure 3.1. Representative images of spontaneously polarized RAW macrophages illustrating the leading edge pseudopod and effects of inhibitors. Cells were plated on glass at 37° C in the absence of an attractant gradient, then spontaneously polarized cells exhibiting extended, ruffling, leading edge pseudopods were imaged as described in Methods. These cells migrate slowly on glass and are thus well suited for quantitative imaging of events and time courses at their leading edges. Drugs were added at $t = 0$ to the total concentration indicated in Table 1. (A-D) Images of single polarized cells illustrating effect of drug addition on the leading edge pseudopod. (A,B) DICM imaging of a single cell to quantify the leading edge pseudopod area before and 5 min after ibuprofen addition, respectively. (C,D) Fluorescence imaging of AkT-PH-mRFP in a single cell to quantify the leading edge PIP₃ signal before and 5 min after

wortmannin addition, respectively (28, 32). (E,F) Subsections of DICM super-image quantifying the number of cells with extended leading edge pseudopods in a population before and 5 min after ibuprofen addition, respectively. Dividing cells are occasionally observed as illustrated by the pair at lower left. (G-N) DICM timecourse analyzing the effect of ibuprofen addition at $t = 0$ on the leading edge pseudopod, illustrating the temporary collapse followed by adaptation and recovery (timepoints 0, 2.5, 5, 9, 30, 60, 120, 180 min after ibuprofen addition). Scale bars indicate 10 μm .

15 total cells imaged in at least 3 experiments on at least 2 separate days for control treatments.

Statistical significance of differences between global means was calculated using student's t-test: a one-tailed test was employed for significance of a predicted increase or decrease, while a two-tailed test was used for significance of a possible difference of either sign.

Timecourses of cell populations in a large field containing approximately 1000 cells (Figs 3.4 and 3.6) were generated by imaging unit areas that served as individual data points and were stitched together into a full field stitched composite image (super-image) using Nikon Elements software. The field was scanned as either 8 x 8 (Fig 3.4) or 6 x 6 (Fig 3.6) unit areas. For each full field, an initial $t = 0$ super-image was captured, then super-images were captured at the specified timepoints after addition. Analysis of population timecourse data was as follows. In each single experiment, a population of 1245 ± 125 cells were captured in a super-image generated by stitching together 64 unit areas in an 8 x 8 grid using Nikon Elements Software. At each timepoint, the number of polarized cells with extended leading edge pseudopods was counted in Fiji (ImageJ) yielding an average over the 64 (Fig 3.4) or 36 (Fig 3.6) unit areas of that super-image. For each super-image, the resulting mean timepoints were normalized to the mean initial value of the $t = 0$ timepoint.

Finally, the final global mean timecourse was determined by averaging the corresponding mean normalized timepoints from different super-images (experiments), yielding the global mean timepoints and their SEM for $N =$ the number of super-images. The resulting global mean timecourses represent averages over 3 - 6 super-images (experiments) each containing approximately 1000 cells and collected from independent wells over 3 - 6 separate days for therapeutic drug treatments, or 2 - 6 separate days for control treatments. The

statistical significance of differences between global means was determined as described above for single cell studies.

LC-MS Conditions. Samples for mass spectrometry analysis were set up identically as those for long-term recovery experiments. 50 μL of media were taken from the sample immediately after drug addition and mixing, then snap frozen in LN₂. Samples were allowed to incubate 180 minutes before another 50 μL sample was withdrawn and snap frozen. After storage at -80 °C and thawing, samples were diluted into 250 μL MeOH containing 50 μM meloxicam as an internal sample standard. Samples were then stored at -20 °C for 20 minutes and subsequently spun at 15,000 x g for 15 minutes. While not disturbing the precipitated pellet, 200 μL of supernatant was extracted and dried via speedvac. Mass spectrometry sample images were also analyzed to ensure cell polarization recovery after drug addition. Prior to LC-MS analysis, dried study samples containing each drug were reconstituted in 200 μL (ibuprofen, acetaminophen and aspirin) or 100 μL (diclofenac) of 20 mM ammonium acetate in 60% water/35% acetonitrile/ 5% methanol + 0.1% formic acid. Except for acetaminophen samples, the reconstitution solvent also contained 20 μM 4-amino-salicylic acid (4-ASA) that was used as a post-reconstitution internal standard to monitor final sample preparation and mass spec performance (4-ASA overlapped the acetaminophen peak).

The LC system was composed of an Agilent 1100 binary pump, an Agilent 1110 autosampler and an Agilent 1100 temperature-controlled column compartment (Agilent Technologies, Santa Clara, CA). 10 μL of each sample was injected into the LC. Chromatography was performed in reverse phase (RP) on Agilent Eclipse XDB-C8 column (150 x 4.6 mm, 5.0 μm particle size, Agilent Technologies, Santa Clara, CA). The flow rate was 0.400 mL/min, auto-sampler temperature was kept at 4 °C, and the column compartment was set at 40 °C. Chromatography time was 35 min, and all 6 peaks eluted off the column between 10 and 20 min without any overlapping except for acetaminophen and 4-ASA.

Mass Spectrometry (MS) Conditions and Data Processing. After the chromatographic separation, MS ionization and data acquisition was performed using AB Sciex QTrap 4000 mass spectrometer (AB Sciex, Toronto, ON, Canada) equipped with electrospray ionization (ESI) source ionizing ibuprofen, aspirin, diclofenac as well as internal standards (meloxicam and 4-aminosalicylic acid) in negative and acetaminophen in positive mode, respectively. The instrument was controlled by Analyst 1.5 software (AB Sciex, Toronto, ON, Canada). Targeted data acquisition was performed in multiple-reaction-monitoring (MRM) mode. 5 MRM transitions were monitored in negative mode (4-aminosalicylic acid: 153.2 - /108.2 - ; aspirin: 180.2 - /137.3 - ; ibuprofen: 206.2 - /161.3 - ; diclofenac: 296.2 - /250.6 - and meloxicam: 351.4 - /147.0 -) whereas acetaminophen was analyzed in positive mode (MRM: 152.1 + /110 +). The source and collision gas was N₂ (99.999% purity). The ion source conditions were: curtain gas (CUR) = 25 psi, collision gas (CAD) = medium, ion spray voltage (IS) = ± 4K V, temperature (TEM) = 300 °C, ion source gas 1 (GS1) = 50 psi and ion source gas 2 (GS2) = 40 psi. Each MRM transition was scanned in “unit” resolution in both Q1 and Q3.

The extracted MRM peaks were integrated using MultiQuant 2.1 software (AB Sciex, Toronto, ON, Canada). The two spiked internal standards (meloxicam and 4-aminosalicylic acid) were used to monitor sample preparation and LC-MS assay performance. A standard mixture of all four study drugs was used as a quality control to measure signal reproducibility. Intra-day and inter-day reproducibility for each measured molecule was under 10% without data normalization.

RESULTS

Approach. To characterize the effects of drugs on the leukocyte leading edge chemosensory pathway, we utilized both single cell and cell population assays to monitor the

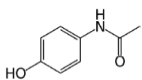
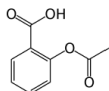
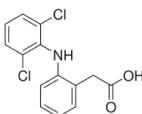
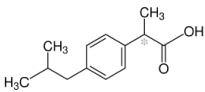
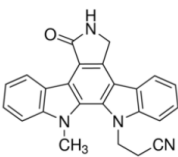
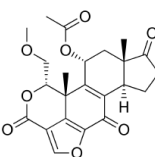
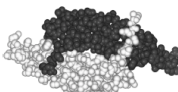
leading edges of RAW macrophages plated at controlled, low density on clean glass in standard media at 37° C in the absence of an attractant gradient. Under this basal environmental condition, the leading edge positive feedback loop triggers spontaneous polarization of a sizable subset (9 + 2 %) of the macrophage population, yielding large numbers of slow moving, easily imaged, polarized cells with well-developed leading edges spanned by a single, ruffling pseudopod (8, 115). Activators and inhibitors of the positive feedback loop are known to expand and contract the leading edge pseudopod, respectively, via a signaling mechanism that involves increased or decreased levels of the PIP₃ signaling lipid in the cytoplasmic leaflet of its plasma membrane, respectively (8, 103, 115, 138).

Single cell studies were carried out to probe the short-term effects of drugs on the size (area) and PIP₃ signal of the leading edge pseudopod in individual RAW macrophages. Each imaging experiment employed differential interference contrast microscopy (DICM) and spinning disk confocal fluorescence microscopy to record high resolution z-stacked images of the leading edge pseudopod of a polarized, actively ruffling macrophage before addition of each drug, and at selected timepoints for 5 min after drug addition. The resulting DICM images were used to quantify the timecourse of drug effects on pseudopod area, while the fluorescence images quantified levels of a standard fluorescent PIP₃ sensor (AKT1 PH domain fused to mRFP (8, 115)) on the pseudopod membrane. For a given drug treatment, timecourses obtained from observations of 17 to 32 single cells were averaged to generate a mean timecourse for drug effects on the leading edge pseudopod area and PIP₃ signal.

Population studies were carried out to quantify both short- and long-term effects of drugs on the leading edge pseudopods of large numbers of polarized cells in RAW macrophage populations. These studies employed DICM to record high resolution z-stacked images of macrophage populations containing ~1000 total cells, captured in subpopulations of ~20-40 cells per unit area in a grid containing 36-64 such areas per superimage. The number of cells with extended leading edge pseudopods per unit area was quantified before drug addition, and

at selected timepoints for 3 hours after drug addition. Finally, the mean timecourses for 6 superimages were averaged to generate an overall mean timecourse for effect of each drug on the number of polarized cells in the population.

The single cell and population assays are complementary. The single cell analysis provides a high resolution view of effects of drugs on the leading edge pseudopod for at least 17

Drug	Structure	M.W.	pKa	Therapeutic Concentration ^a	Experimental Concentration ^b	Target
Acetaminophen		151.16 Da	9.5 ^c	2.5–25 µg/mL ^d 17–170 µM	170 µM	Unclear
Acetylsalicylic Acid		180.16	3.5 ^c	20–200 µg/mL ^d 110–1100 µM	1100	COX1/2
Diclofenac		296.15	4.0 ^c	0.3–5 µg/mL ^e 1–17 µM	17	COX1/2
Ibuprofen		206.29	5.2 ^c	10–50 µg/mL ^d 50–240 µM	240	COX1/2
Gö6976		378.43	N/A	N/A	1.0	PKC
Wortmannin		428.43	N/A	N/A	0.50	PI3K
PDGF-ββ		24,300	N/A	N/A	2.1	PDGF-R

^a Therapeutically recommended range of total concentration in human serum

^b Experimental total concentration in cell culture medium (this study)

Table 3.1. Therapeutic drugs and control compounds employed in this study. A compiled list of the therapeutic drugs (acetaminophen, acetylsalicylic acid, diclofenac, ibuprofen) and control compounds (Go6976, wortmannin, and PDGF-ββ. Structures, molecular weights (in Daltons), and pKa are listed. Therapeutic concentration is on the high end of recommended blood serum therapeutic dose, as found in literature (125-127). Experimental concentration is the concentration employed in this study. Target describes the known molecular target of the compound.

individual, polarized macrophages. This analysis monitors the leading edge area as a sensitive detector of pseudopod function and stability, and also monitors leading edge PIP₃ level as a sensitive detector of pseudopod activity and signaling state. Both leading edge area and PIP₃ levels are highly sensitive sensors of pathway perturbation by drugs. The population analysis monitors the effects of drugs on the leading edge pseudopods of ~100 polarized cells per population of ~1200 total cells, making it possible to quantify how drugs impact the frequency of cells with active pseudopods in the overall population, and to detect long term recovery of the population following drug treatment.

Table 1 summarizes the four selected therapeutic drugs (acetylsalicylic acid, acetaminophen, diclofenac, ibuprofen), their recommended maximum dosages in humans, and other relevant parameters. Table 1 also summarize three control drugs (Go6976, wortmannin, PDGF-ββ) routinely used in laboratory studies of the leading edge pathway, as well as their standard experimental concentrations (8, 115).

Single cell analysis of drug-induced perturbation of the leading edge pseudopod.

To measure the timecourse of drug effects on individual RAW macrophages, highly polarized cells with extended, ruffling leading edge pseudopods were selected for observation, as illustrated in Fig 3.1. Note that selection of this subpopulation intentionally limits the study to healthy cells with an active leading edge pseudopod and signaling pathway. Subsequently, a drug or control vehicle (DMSO or buffer) was added, followed by immediate mixing and imaging at selected timepoints.

Fig 3.2 summarizes the effects of the four therapeutic drugs on the macrophage leading edge pseudopod. Rapid addition of the therapeutic dose of acetylsalicylic acid or diclofenac had little or no detectable effect on the pseudopod area (Fig 3.2A) and PIP₃ levels (Fig 3.2C). By contrast, addition of the therapeutic dose of ibuprofen or acetaminophen triggered significant loss of pseudopod area (decreased 49 + 10 %, $p < 0.001$, or 53 + 9 %, $p < 0.001$, respectively;

Fig 3.2A) and significant loss of pseudopod PIP₃ (decreased 27 + 7 %, p < 0.001, or 32 + 9 %, p < 0.001, respectively; Fig 3.2C) within 5 min. The parallel decreases in pseudopod area and PIP₃ levels triggered by ibuprofen or acetaminophen is consistent with pseudopod destabilization via inhibition of the leading edge signaling pathway.

Fig 3.2 also summarizes the effects of the three control drugs on the leading edge pseudopod. Addition of the known pathway activator (PDGF-ββ) led to a significant pseudopod area expansion (increased 43 + 12 %, p < 0.001) and increased PIP₃ levels (by 17 + 5 %, p < 0.001) during the 5 min observation period (Figs 3.2B,D). By contrast, the two control pathway inhibitors wortmannin and Go6976 each triggered significant losses of both the pseudopod area (decreased 38 + 6 %, p < 0.001 and 39 + 7 %, p < 0.001, respectively) and the PIP₃ signal (decreased 52 + 16 %, p < 0.001 and 55 + 15 %, p < 0.001, respectively) (Figs 3.2B,D).

The observation that a subset of the tested compounds significantly perturb pseudopod area and PIP₃ levels in single cell studies raises the possibility these drugs may directly modulate PI3K lipid kinase activity. Control studies summarized in Fig 3.3 confirm that wortmannin, a known irreversible PI3K inhibitor (8, 139), directly blocks the PIP₃ production of purified PI3K in vitro as expected. In contrast, the other drugs have little or no direct effect on the PIP₃ production of purified PI3K, indicating that only wortmannin directly inhibits PI3K activity.

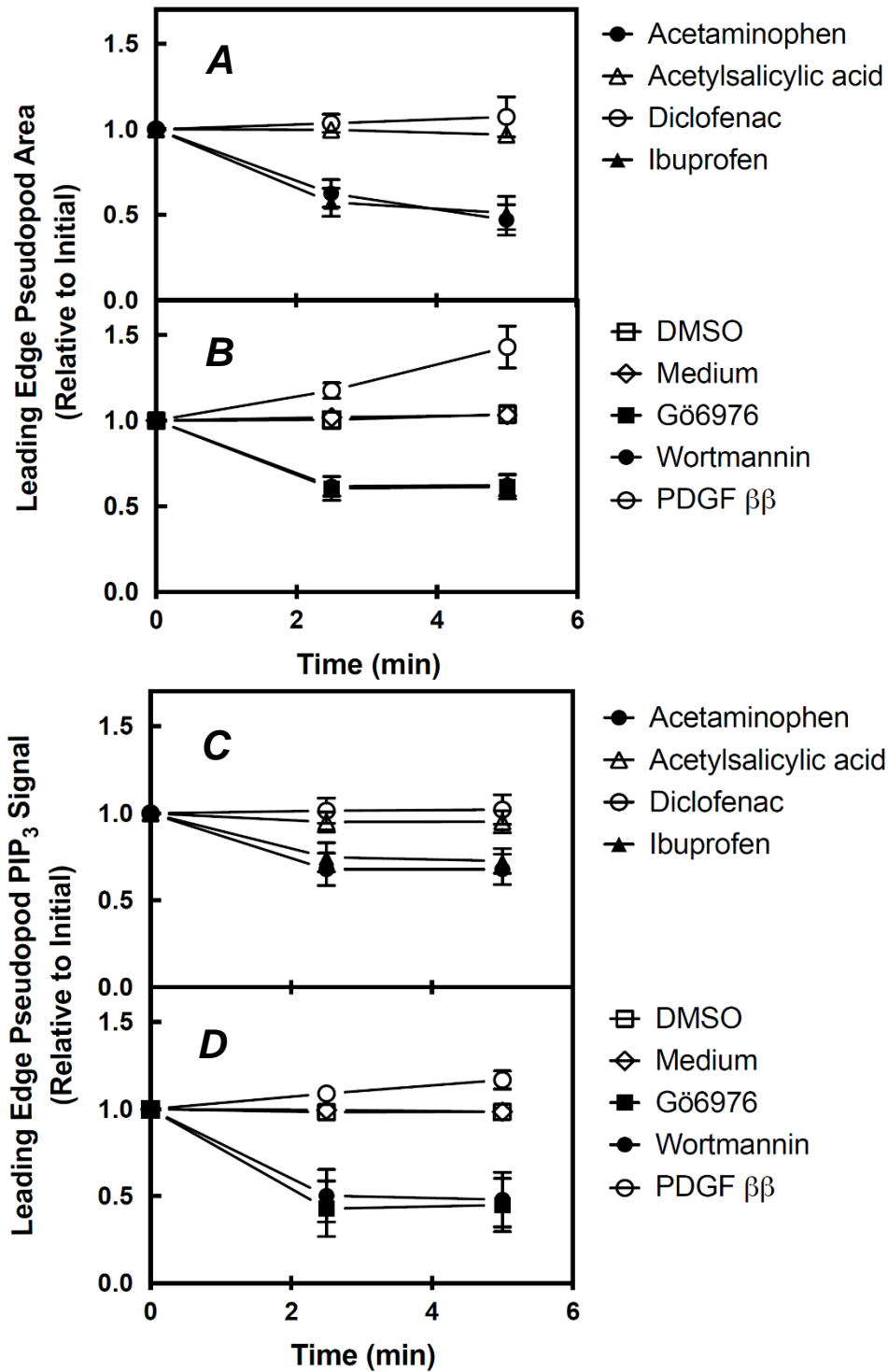


Figure 3.2. Short term effects of rapid drug addition on single polarized RAW macrophages. Cells were plated on glass in the absence of an attractant gradient, then the leading edge pseudopods of single polarized macrophages were imaged before treatment ($t = 0$) and at the indicated timepoints after addition of drug to the concentration indicated in Table 1. Plots show the effects of each drug on the leading edge pseudopod area (A,B), and PIP₃ level (C,D). Error bars are SEM for $N = 17$ to 32 cells over at least three experiments on at least two different

days. Error bars smaller than their data point symbol are not visible. This figure and data provided by Dr. Brian Ziemba. For details of the protocol and image analysis see ref 28.

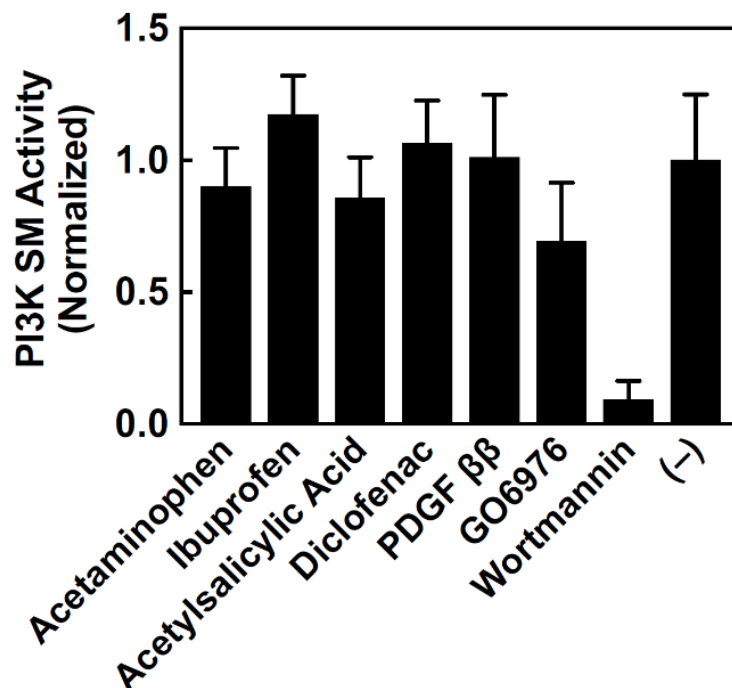


Figure 3.3. Effect of drugs on the lipid kinase activity of purified PI3K in an in vitro PIP₃ production assay. A previously described single molecule total internal reflection fluorescence microscopy (TIRFM) assay was employed to measure the specific kinase activity of purified PI3K molecules on a supported lipid bilayer by counting the number of PI3K molecules, as well as the number of product PIP₃ molecules they produce, via single molecule fluorescence (23-26, 72-74). Bars indicate the specific activity of PI3K in the presence of the indicated drug at the total concentration indicated in Table 1. Error bars are SD where n = 3 for acetylsalicylic acid and diclofenac, or n = 6 for ibuprofen and acetaminophen. This data provided equally by Dr. Brian Ziemba and Dr. Thomas Buckles.

Population analysis of drug-induced perturbation of the leading edge pseudopod.

To measure the long term timecourses of drug effects on populations of polarized RAW macrophages, populations of ~1000 well-resolved cells plated on glass in standard media were imaged at 37° C (see Methods and Approach). Only those macrophages with an active leading edge signaling pathway display the extended, ruffling leading edge pseudopod, which is thus used as a signature of pathway function (8, 115). Cells with extended, leading edge pseudopods were counted in each unit area at 6 timepoints during the 3 hr observation period.

Fig 3.4A shows the effects of the four therapeutic drugs, each added at the recommended clinical dosage, on the relative number of cells possessing extended leading edge pseudopods per unit observation area. As in the single cell analysis, acetylsalicylic acid or diclofenac had little or no effect on the number of cells with extended pseudopods over the 3 hour observation period, yielding timecourses indistinguishable from that of control vehicle addition. In contrast, within 5 min of addition, ibuprofen and acetaminophen each triggered significant reduction of the number of cells with extended pseudopods (decreased $74 \pm 14 \%$, $p < 0.001$ and $27 \pm 5 \%$, $p < 0.01$, respectively), as observed in the single cell assay. Notably, however, within 3 hours of ibuprofen or acetaminophen addition the number of cells with extended pseudopods returned to the initial level, suggesting that the macrophage population adapted to each drug, or that the drug was unstable in the tissue culture media.

Fig 3.4B shows the effects of the three control drugs on the normalized number of pseudopod-possessing cells in the RAW macrophage population. Global addition of the pathway activator (PDGF- $\beta\beta$), a known macrophage chemoattractant, triggered a significant increase (by $52 \pm 9 \%$, $p < 0.01$) in the number of pseudopod-possessing cells within 3 hours. At the other extreme, addition of a control pathway inhibitor (either wortmannin or Go6976) triggered a major decrease (by $90 \pm 1 \%$, $p < 0.001$ or $62 \pm 3 \%$, $p < 0.001$ respectively) in the number of observed pseudopods within 5 min, with little or no recovery during the 3 hour observation period as expected for strong inhibition of an essential component of the leading edge pathway.

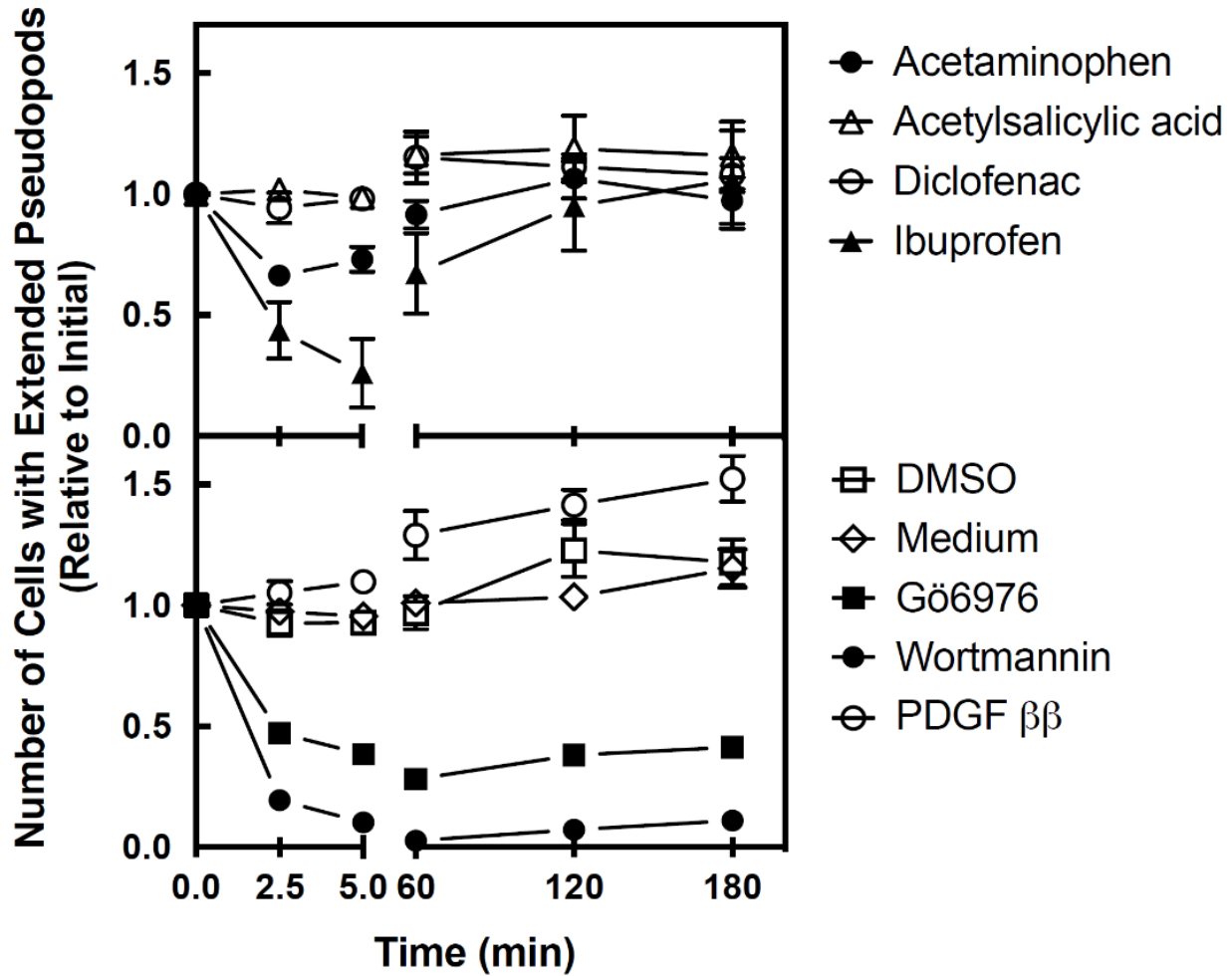


Figure 3.4. Long term effects of rapid drug addition on populations of polarized RAW macrophages. Cells were plated on glass in the absence of an attractant gradient, then images of the cell population were collected at the indicated timepoints following addition of (A) therapeutic drugs, or (B) control drugs at $t = 0$ to the total concentrations indicated in Table 1. The number of cells in the population displaying extended leading edge pseudopods was counted for each timepoint and normalized to the initial number prior to drug addition. Data collected for multiple populations was averaged, yielding the illustrated mean timecourse for each treatment. Error bars are SEM for $N = 6$ experiments carried out on at least five days for experimental treatments, or at least two days for control treatments. Error bars smaller than their data point symbol are not visible.

Mass spectrometry analysis of drug levels during the three hour cell observation period.

The finding that two therapeutic drugs had no detectable effect on the leading edge pseudopod, while two other therapeutic drugs triggered an initial perturbation followed by recovery, raised the possibility that the drugs might be unstable in the cell culture. Quantitative mass spectrometry analysis was carried out to ascertain whether each of the four target drugs was present at the intended level when the timecourse began, and after three hours in culture. Fig 3.5 shows that each of the four therapeutic drugs was present in the cell culture media at the intended clinical concentration at the first timepoint after addition, and exhibited relatively little change during the three hour incubation. Thus, each of the four drugs remained at an

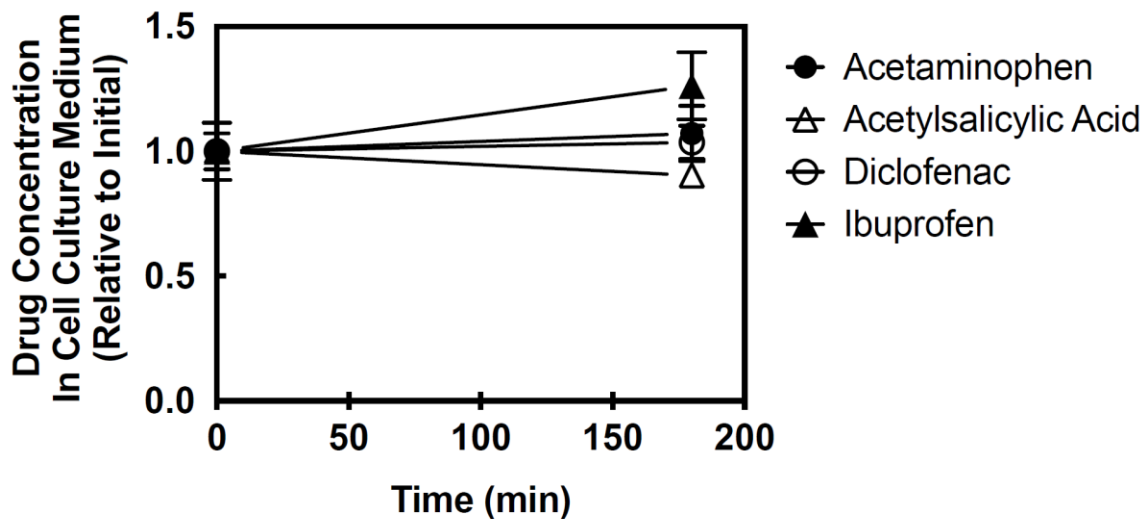


Figure 3.5. Stability of therapeutic drug concentrations in cell culture after rapid drug addition. Each of the four therapeutic drugs was analyzed in standard population imaging experiments (Fig 3.4) to ascertain the stability of the total drug concentration in the media surrounding the cells. Aliquots of media were removed from cell imaging wells immediately after drug addition at $t = 0$ to the total concentration indicated in Table 1, and again at $t = 3$ hr after completion of imaging, then snap frozen. Later, the samples were prepared for quantitation with addition of internal standards, then quantitative mass spectrometry was carried out to compare the initial and final drug concentrations. Error bars are SD for $n = 3$ (acetylsalicylic acid, diclofenac) to 6 (ibuprofen, acetaminophen).

approximately fixed, standard clinical concentration during the timecourses described in this study. It follows that macrophages are relatively insensitive to clinical levels of acetylsalicylic acid and diclofenac, while rapid addition of ibuprofen or acetaminophen to their clinical level

triggers a temporary perturbation of the leading edge pseudopod followed by gradual adaptation of the macrophage population to the constant presence of these drugs in the media during a recovery period.

Population analysis of the effects of slow drug addition on the leading edge pseudopod. To ascertain whether perturbations of the leading edge pseudopod observed for rapid addition of ibuprofen or acetaminophen are alleviated by more gradual drug addition over a period of 90 min, additional studies were carried out on populations of polarized RAW macrophages comparing the effects of rapid and incremental drug addition. As before, cells were plated on glass in the absence of an attractant gradient, and control rapid drug additions at $t = 0$ yielding the final concentration indicated in Table 1 were carried out as in Fig 3.4. In parallel, more gradual additions of drug or carrier were carried out in four equal increments at 0, 30, 60, 90 min, together yielding the same final drug concentration indicated in Table 1. Cells with extended, leading edge pseudopods were imaged and counted in each unit area at the indicated timepoints during a 125 min observation period as shown in Fig 3.6.

Fig 3.6 compares the effects of rapid and slow addition of a given perturbing drug (ibuprofen or acetaminophen) on the relative number of cells possessing extended leading edge pseudopods. As before, rapid addition of ibuprofen or acetaminophen at $t = 0$ triggered significant reduction of the number of cells with extended pseudopods within 5 min (decreased $70 \pm 5\%$, $p < 0.01$ and $26 \pm 6\%$, $p < 0.03$, respectively) followed by slow recovery. Notably, however, slow addition of ibuprofen or acetaminophen over a period of 90 min, incrementally approaching the same final concentration as the rapid addition protocol, had no significant effect on the number of cells with extended pseudopods ($0.75 > p > 0.21$ and $0.91 > p > 0.73$ for the

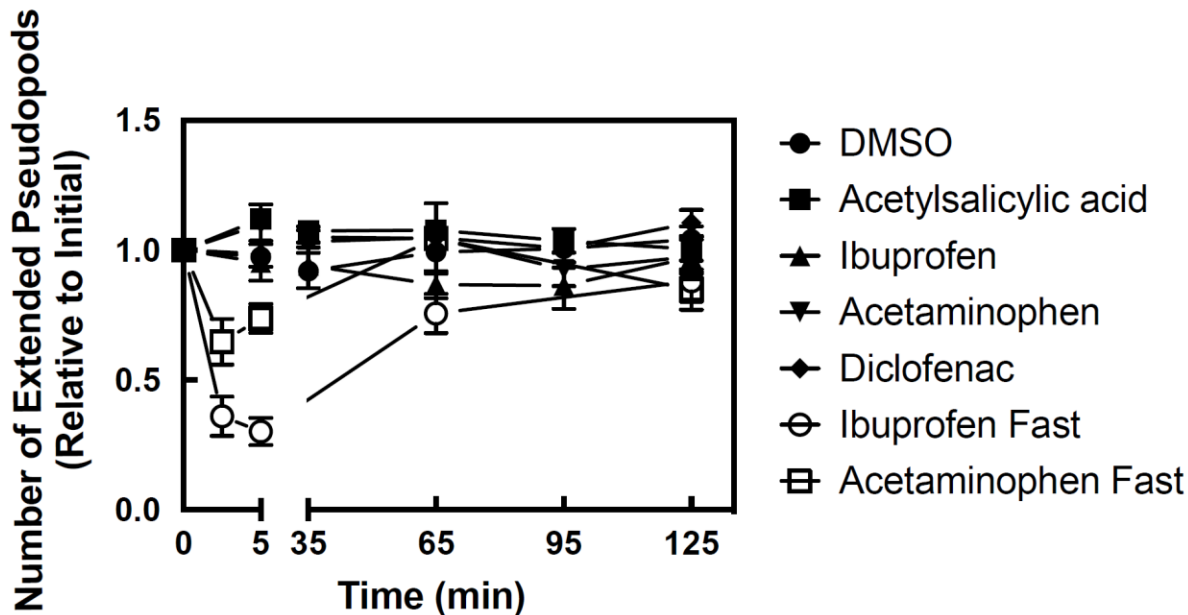


Figure 3.6. Effects of slow drug addition on populations of polarized RAW macrophages. Cells were plated on glass in the absence of an attractant gradient, then drug or carrier was added in four equal increments at 0, 30, 60, 90 min together yielding the final concentration indicated in Table 1. Images of the cell population were collected 5 min after each incremental addition, at the indicated timepoints (filled symbols). In parallel, control rapid addition timecourses were acquired as described in Fig. 3.4 for the two drugs found to collapse the leading edge pseudopod when added rapidly (ibuprofen fast and acetaminophen fast, open symbols). The number of cells in the population displaying extended leading edge pseudopods was counted for each timepoint and normalized to the initial number prior to drug addition. Data collected for multiple populations was averaged, yielding the illustrated mean timecourse for each treatment. Error bars are SEM for N = 3 (fast acetaminophen) or 4 (others) experiments carried out on at least three days. Error bars smaller than their data point symbol are not visible.

full range of timepoints, respectively). Fig 3.6 also shows, as previously observed for rapid addition (Fig 3.4), that slow addition of acetylsalicylic acid, diclofenac, or carrier DMSO had little or no effect. In summary, for all therapeutic drugs tested, gradual drug addition yielded no detectable effect on the leading edge pseudopod, in contrast to the pseudopod collapse triggered by rapid addition of certain drugs. This finding suggests that when the perturbing drug is added sufficiently slowly, the same adaptation process observed after rapid addition of ibuprofen or acetaminophen is able to concurrently respond with regulatory adjustments that maintain leading edge integrity.

DISCUSSION

The present findings identify two therapeutic drugs that, when added rapidly up to their standard clinical concentration, trigger short term collapse of the macrophage leading edge pseudopod followed by adaptation and recovery. More broadly, the results show that an analysis of polarized macrophages employing both single cell and population measurements can effectively classify therapeutic and research pharmaceuticals into at least four distinct functional classes ranging from inhibition to activation. (i) Ibuprofen and acetaminophen illustrate a category of transiently perturbing drugs that, when added rapidly, trigger significant collapse of the leading edge pseudopod area and PIP_3 signal within minutes in single cells, as well as dramatic loss of pseudopod-possessing cells in the macrophage population. On a longer timescale of hours, the macrophage population adapts to these drugs and the number of cells possessing extended leading edge pseudopods returns to pre-drug levels. (ii) Wortmannin and Go6976 are representative toxic drugs that generate long-term loss of the leading edge pseudopod and its PIP_3 lipid signaling, with no detectable adaptation and recovery. (iii) Acetylsalicylic acid and diclofenac illustrate a category of non-perturbing drugs that yield no detectable effect on leading edge pseudopod area and PIP_3 levels, nor on the number of pseudopod-possessing cells in the population. (iv) Platelet derived growth factor ($PDGF-\beta\beta$) is a representative activator that increases leading edge pseudopod area, as well as PIP_3 levels and the number of pseudopod-possessing cells observed in the population.

The most intriguing new observations are that rapid addition of ibuprofen or acetaminophen up to its clinical concentration at $t = 0$ triggers a rapid collapse of the macrophage leading edge pseudopod, and this initial perturbation is followed by gradual pseudopod recovery. The perturbation requires rapid drug addition, since incremental addition of the same drugs to the same therapeutic concentration over 90 min yields no detectable pseudopod collapse. The mechanisms by which rapid ibuprofen or acetaminophen addition

transiently inhibits the leading edge pseudopod remains unknown. Neither drug directly blocks the lipid kinase activity of purified PI3K in a standard PIP₃ production assay, indicating they are not PI3K inhibitors. It follows that the perturbing drugs may specifically modulate unidentified component(s) of the leading edge pathway other than PI3K, or trigger a nonspecific cellular perturbation (most likely not a pH change, since the drug perturbations are not strongly correlated with drug pKa values (Table 1)).

Similarly, the mechanism of pseudopod adaptation and recovery following rapid drug addition and transient pseudopod collapse is not yet known. The same adaptation mechanism is hypothesized to be acting during slow drug addition to successfully counteract and mask the effects of drug perturbation, thereby accounting for the lack of pseudopod collapse observed for the slow addition protocol. The adaptation mechanism does not involve extracellular chemical or enzymatic degradation of the drug in the media, since mass spectrometry analysis indicates that when each drug is added at $t = 0$ to cultured macrophages, the drug remains stable at its clinical concentration in the media during the three hour incubation. It follows that macrophages utilize one or more intracellular mechanisms that enable adaptation to the perturbing drug over a period of minutes to hours. Such adaptation could arise from the intrinsic adaptation capabilities of the leading edge chemosensory pathway which, like other sensory pathways, must adapt to background signals and other features of the local environment in order to detect attractant gradients in different environments (140-143). Other possible adaptive mechanisms could include activation of an intracellular sink, pump, degradation or modification reaction that eliminates free drug in the cell interior, but has a negligible effect on the bulk external drug concentration. Such mechanisms have been reported for other drugs (reviewed in (144, 145)

The well-established lack of clinical toxicity observed for four therapeutic drugs at their recommended dosage (146) is fully compatible with the present findings, since two (acetylsalicylic acid and diclofenac) have little or no effect on the leading edge signaling pathway of macrophages in culture, while the other two (ibuprofen and acetaminophen) yield

temporary perturbations of the leading edge pseudopod that gradually disappear as the cells adapt and recover. Moreover, the temporary perturbations observed for the latter two drugs require rapid drug addition, since gradual addition over 90 min of each drug to its peak, therapeutic total concentration yielded no detectable pseudopod perturbation. In a clinical setting these drugs are typically administered orally, yielding a gradual buildup of total drug concentration in the serum requiring 0.5 - 2 hr to reach peak concentration (147-151). The present

findings strongly suggest that such a gradual increase allows concurrent gradual adaptation of the macrophage population, thereby minimizing drug-induced perturbation of the leading edge pseudopod and the innate immune response, and fully accounting for the safety of these drugs in the clinic. However, our findings also suggest that rapid introduction of a perturbing drug in seconds or minutes, for example by intravenous injection, could increase the drug concentration too rapidly for macrophage adaptation, potentially increasing the risk of infection by temporarily inhibiting the innate immune response. The present in vitro assay enables identification of drugs that perturb the leading edge pseudopod when added rapidly, as well as drug perturbations that the macrophage adaptation process can counteract and overcome given adequate time to respond.

The present findings suggest a number of directions for future research. Further studies are needed to determine the molecular mechanisms by which rapid ibuprofen or acetaminophen addition inhibits macrophage leading edge activity, and by which macrophages adapt to these drugs. For example, acetaminophen has been shown to reduce intracellular glutathione levels (152), potentially suggesting an oxidative stress driven mechanism. Additional studies are needed to ascertain whether similar effects and mechanisms are observed for other therapeutic drugs, in macrophages and other leukocytes including neutrophils, and to confirm that perturbation of the leading edge pseudopod inhibits leukocyte migration (153). Furthermore, it will be important to ascertain whether rapid administration of

perturbing drugs in animal studies can trigger temporary inhibition of the leukocyte leading edge pseudopod, and whether such inhibition yields temporary suppression of the innate immune response. The present findings suggest the utility of testing drugs on cultured leukocytes, especially before designing treatment protocols involving rapid drug introductions (i.e. rapid intravenous injection).

Chapter IV:

Discussion and Future Studies

A Role for Ras in Altering the Docking Geometry and Specific Kinase Activity of PI3K. Chapter II examined the mechanism by which H-Ras combines with soluble phospho-Tyr peptide to synergistically activate PI3K α , mimicking H-Ras synergy with soluble phospho-Tyr PI3K activators. This H-Ras synergistic activation is primarily recruitment driven, arising from a net 20 ± 2.5 fold increase in the surface density of stably bound PI3K α in the presence of surface tethered H-Ras driven by a 19 ± 5 fold increase in the PI3K α membrane docking on-rate and a 1.4 ± 0.3 fold decrease of the PI3K α membrane off-rate. Surprisingly, the binding of PI3K α to membrane-anchored H-Ras also generates a small but reproducible 2.6 ± 0.6 fold decrease in the lipid kinase turnover rate of PI3K α . Overall the combined effect of the greatly increased surface density and the slightly slower catalytic turnover rate yield a net increase in the total rate of PIP₃ production approaching one order of magnitude (8 ± 2 fold) under these same conditions (Chapter II).

The observation that PI3K α exhibits a slightly lower specific activity when in the presence of H-Ras on the membrane surface raises the question of how the protein-protein association slightly perturbs the average turnover rate of membrane-bound PI3K α . One possibility is that the H-Ras triggered allosteric conformational change observed in crystallographic studies of complex formation, which is transmitted to the PI3K α catalytic site, is primarily responsible for the perturbation. In addition, it appears that H-Ras binding must perturb the PI3K α membrane docking geometry. The latter conclusion is evidenced by the present observation that H-Ras binding does not slow the PI3K α membrane off-rate as much as expected for simple thermodynamic additivity of PI3K α binding to both membrane and H-Ras, suggesting that binding to H-Ras weakens the binding of PI3K α to the membrane surface, in

turn suggesting that the protein-protein interaction alters the membrane docking geometry of PI3K α .

The geometry of membrane docking could be affected due to the size, shape, and / or the orientation of Ras in the Ras-PI3K complex. As previously noted in Chapter II, all Ras isoforms are covalently tethered to the inner leaflet of the plasma membrane via at least one, and up to three, prenylated cysteine residue(s) at their C-terminus. Upstream of the cysteine residues is the hypervariable domain – an unstructured, approximately 20 residues long region (in H-Ras, varying in other isoforms) acting as a link between the lipid bilayer and the globular effector domain of Ras (20, 22, 56, 154). The HVR tether of H-Ras may be preventing PI3K α from making full wild-type membrane contacts due to a constraint of the combined length of the HVR, cystine-maleimide-lipid linkage, and globular domain of Ras. A hypothetical model of H-Ras-bound to the Ras binding domain (RBD) of the current model for membrane-docked PI3K α (Fig 4.1) shows that the distance between the C-terminus of the globular H-Ras domain and the surface of the lipid bilayer is approximately 20 Ångstroms. The number of HVR residues between the C-terminus of the H-Ras globular domain and the first membrane-anchoring Cys residue of the HVR is 20 residues in wild-type H-Ras and 19 residues in the H-Ras construct employed in Chapter II. These correspond to approximately a 70 Ångstrom and 66 Ångstrom lengths respectively, if fully extended.

Although both wild-type and the experimental constructs' fully extended HVR would be more than long enough to bridge the distance between the globular domain of RBD-bound Ras and the lipid bilayer, recent computational work (155, 156) predicts that the HVR of K-Ras is not on average fully extended, but rather contains tertiary structure. A compact, folded HVR would likely be too short to bridge the 20 Å gap between the H-Ras globular domain and the membrane surface. In this scenario, some fraction of the Ras – PI3K complexes would have a perturbed docking geometry at the PI3K-membrane interface, with the degree of perturbation

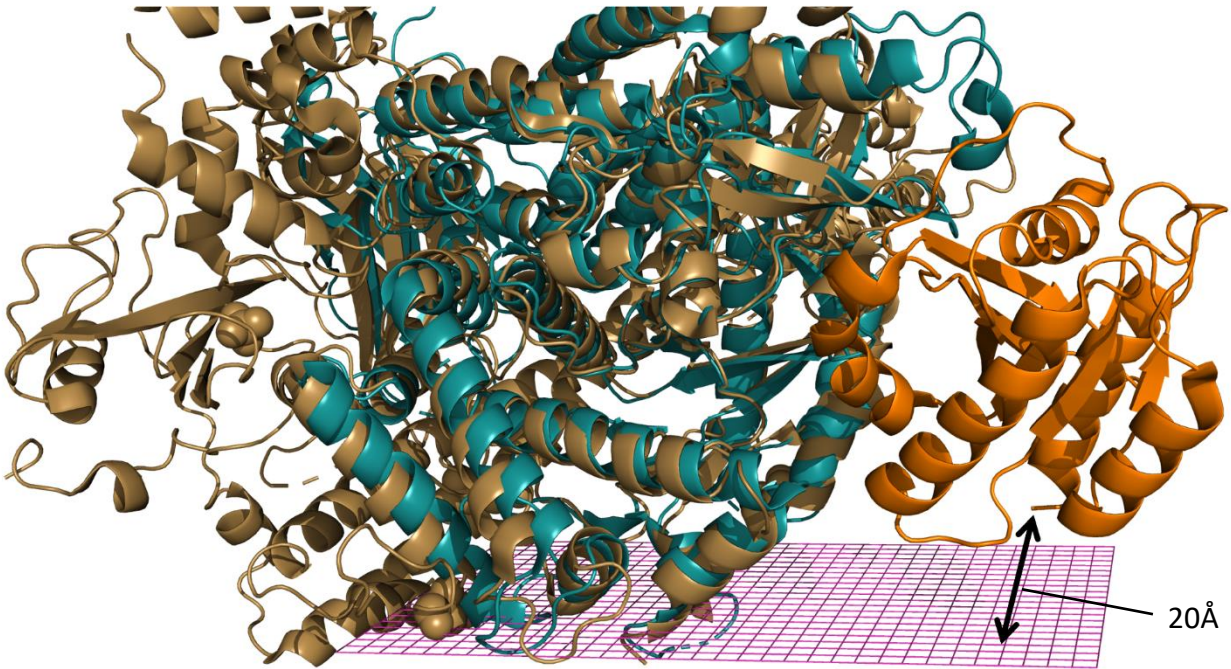


Figure 4.1. To-scale model of H-Ras-PI3K γ -lipid bilayer. The structure of PI3K γ (dark teal) bound to H-Ras (orange)(51) was threaded and aligned to the structure of PI3K α (tan)(157). Experimental and computational studies predicting the membrane-PI3K α interface (65, 156) were referenced to generate a membrane bilayer surface location (purple, grid). The hypervariable domain (HVR) of H-Ras (residues 166-185) is truncated due to the difficulty in crystallization of unstructured protein domains. The length between the end of the globular domain and the top of the bilayer, as indicated by the black arrows, is approximately 20 Ångstroms.

depending on the how the shortened length of HVR forces PI3K to undergo a conformational change or tilt relative to the bilayer to bring the Ras binding domain down to the level of H-Ras. Though the simulations suggesting a compact HVR focused on K-Ras, and the HVR domain exhibits little sequence homology between isoforms, it is plausible that analogous structure formation in the H-Ras HVR could drive a change in the PI3K α docking geometry responsible for the faster than expected dissociation rate, and that could also contribute to the observed subtle specific activity inhibition of PI3K α upon binding to H-Ras.

A simple method to examine whether Ras HVR sequence identity and length plays a significant role in PI3K α activation is HVR replacement, insertions, and deletions. By

lengthening and shortening an HVR using neutral residue insertion and wild-type residue deletion, the length component of an HVR-influenced PI3K specific activity change can be explored. Replacing the H-Ras HVR entirely with the HVRs of K-Ras and / or N-Ras will test whether the isoform specificity plays a role in the effect. These experiments would involve cloning and the use of an already-developed *in vitro* kinase assay, possibly making this question a relatively easy one to answer.

A related question is whether PI3K α displays the same lower specific activity when bound to the alternative Ras isoforms, N-Ras and K-Ras. Isoform-specific variations in turnover rate could be possible due to the diversity of sequence and length between Ras isoforms of the HVR. If one or both of these isoforms does not decrease the specific activity of PI3K α , then the relative expression levels of H, N, and K-Ras, which vary by cell type (22), could become an important modulator of total PI3K activity. If true, this could represent a subtle but important change in the paradigm of Ras-PI3K signaling. Ras is amenable to bacterial expression (appendix D) making this another easily approachable question and could be done simultaneously with the HVR mutagenesis experiments. It is reasonable to expect similar results between H and N Ras, as the length (20 and 21, respectively) and net charge (+1) of their HVRs are similar, or the same. K Ras4B also has an HVR length of 21 residues – its net charge, however, is significantly different at +10. It utilizes this cationic stretch as an additional tether to anionic lipids in place of a cystine prenylation. It is reasonable to assume the K Ras4B HVR membrane geometry may be different to other isoforms, which may affect the extent of specific activity change observed in PI3K α . Since the HVR is in direct membrane contact for longer than H or N Ras, and the HVRs are all of similar absolute lengths, the “shortened” K Ras4B HVR may result in a larger specific activity drop.

Similarly, an important and unaddressed question is whether PI3K β association with its small G protein activator Rac1 causes a drop in specific activity. Future studies of the Rac1-PI3K β module that could give further insight into the universality of the observed specific activity

drop. PI3K β activation has been linked to tumor growth (158, 159) and is synergistically activated by G $\beta\gamma$ signaling and Rac1 (154, 158, 159). Both PI3K α and PI3K β are expressed ubiquitously in human cells, lending significance to this module (23), though each kinase isoform also has a specific role within the cell. For example, PI3K β has strong autophagy input (160, 161).

Another, more distantly related module of note is that of the small G protein Rab5 and its lipid kinase substrate, the class III PI3K VPS34. Residing predominantly in the Golgi apparatus and endoplasmic reticulum, the Rab5-VPS34 module is important in vesicle transport to the plasma membrane, as well as many other cellular functions (25, 26, 162-164), and would provide insights outside the context of the plasma membrane. Preliminary evidence presented below in this chapter suggest this system is amenable to study in our experimental system and thus would represent a good module for asking which features of the H-Ras – PI3K α module are universal. Taken together, these modules can provide valuable insight into how G protein kinase signaling works at a global scale, as well as narrow which specific component is responsible for specific kinase activity changes by moving laterally in small G protein identity, lipid kinase identity, and both simultaneously.

A final consideration when addressing both activation mechanisms and docking geometry is the incorporation of a full, transmembrane RTK to the complex. As noted in Chapter II, a soluble phosphopeptide mimic representing a soluble PDGFR activation loop (18, 29, 53, 62-64, 66, 71) was utilized to achieve full PI3K α activation. Technical limitations involving the insertion of a transmembrane RTK into a supported lipid bilayer have thus far led us to study soluble phospho-Tyr peptide activators rather than membrane-anchored constructs, including full length RTKs. The mechanisms by which membrane-anchored phosphotyrosine proteins activate PI3K remains to be addressed. It has already been reported that phosphopeptide activation involves displacement of the inhibitory SH2 domains from the membrane docking face of PI3K (29, 62, 64, 66). This displacement can be mimicked by a soluble phosphopeptide.

However, a membrane-anchored RTK or phosphoprotein may provide membrane recruitment assistance such that the mechanism of Ras synergy could be different from that observed herein for a soluble phosphoprotein activator. This possibility could be examined using a membrane-anchored full RTK (technically not possible in our current supported bilayer system), or a membrane-anchored RTK cytoplasmic domain, or a membrane-anchored phosphopeptide that places the phospho-Tyr residues approximately the same distance from the bilayer as in an intact RTK. We have discussed these possibilities in the Falke lab, and Mo Gordon (a fellow grad student in the lab) is pursuing this direction.

Specific lipid tethering methods that could be used to couple RTK mimic to the supported lipid bilayer in our system include the cysteine coupling to a maleimide lipid headgroup as used to anchor Ras in Chapter II, strained alkyl copper free click chemistry, and biotin-streptavidin tethering. Cysteine-maleimide lipid coupling offers the advantages of being easy, cheap, quick, and specific at physiological pH values. A drawback, however, is that naturally occurring surface exposed cysteines will need to be engineered out to prevent multiple tethering points per RTK mimic, or RTK mimics tethered in the wrong orientation. Finally, the use of the same chemistry employed to anchor Ras could complicate controlled studies of Ras-RTK activation synergy. Alternatively, strained alkyne click chemistry is covalent and specific, utilizing the large amount of ring strain energy stored in a cyclooctyne to react with a phenylazide unnatural amino acid in the target protein. However, this method requires large amounts of expensive unnatural amino acid in each growth and incorporation can be quite inefficient. Biotin-streptavidin linkage is not covalent – however its K_d , 10^{-15} M (165), is strong enough to act similarly to a covalent modification with a bound state lifetime sufficient for our TIRFM measurements. The size of streptavidin, 60kDa (165), could be used as an advantage in this particular situation, mimicking the size and displacement from the membrane of phospho-Tyr residues in a full transmembrane RTK.

Once anchored, it is reasonable to expect that the membrane-anchored RTK mimic will drive additional recruitment of PI3K to membrane, as well as the allosteric activation provided by displacement of the autoinhibitory SH2 domains from the PI3K membrane docking face. When bound to the flexible phosphotyrosine activation sequence of a membrane-anchored RTK mimic, PI3K will be held near the membrane surface, increasing the local concentration of PI3K at the membrane and its average proximity to substrate PIP₂ lipid. This higher local concentration could result in an increase in the density of surface-bound PI3K molecules, and thus an increase in kinase activity. The effects of such a membrane-anchored RTK mimic on the off-rate of PI3K from the membrane, the lifetime of the RTK-PI3K complex, any ancillary allosteric changes to PI3K, and the mechanism of Ras synergy remain to be discovered.

Preliminary and Future Studies of Other G Protein-PI3K Signaling Modules.

Chapter II explored the mechanism by which H-Ras activates class I PI3K α . The same single molecule TIRFM approach described in Chapter II for the H-Ras – PI3K α module will be useful in elucidating the molecular mechanisms of G protein-PI3K interactions and regulation in other modules, thereby revealing universal and specialized features by which G proteins activate PI3K enzymes. As noted above, many isoforms of lipid kinase and G proteins exist in cells and are essential players in activating an array of cellular signaling pathways. The first few modules, being the easiest to address, are the activation of PI3K α by alternative Ras isoforms – N-Ras and K-Ras. Of the remaining untested, the most significant could be that of K-Ras. K-Ras mutations are involved in over a quarter of all cancers sequenced (20). A similar methodology to that used in chapter II could be easily adapted to study one or both of the remaining Ras isoforms, as they both are natively tethered to the membrane bilayer via a cysteine residue and thus should be amenable to the same cysteine-maleimide-lipid coupling used with H-Ras. In addition, a labeling methodology and site-specific labeling construct for PI3K α has already been verified for binding experiments (19, 71). Another, less closely related module with significant

implications in health and signaling is class I PI3K β and its corresponding small g-protein, Rac1. As one of the two universally expressed class I PI3K isoforms, PI3K β -Rac1 interactions

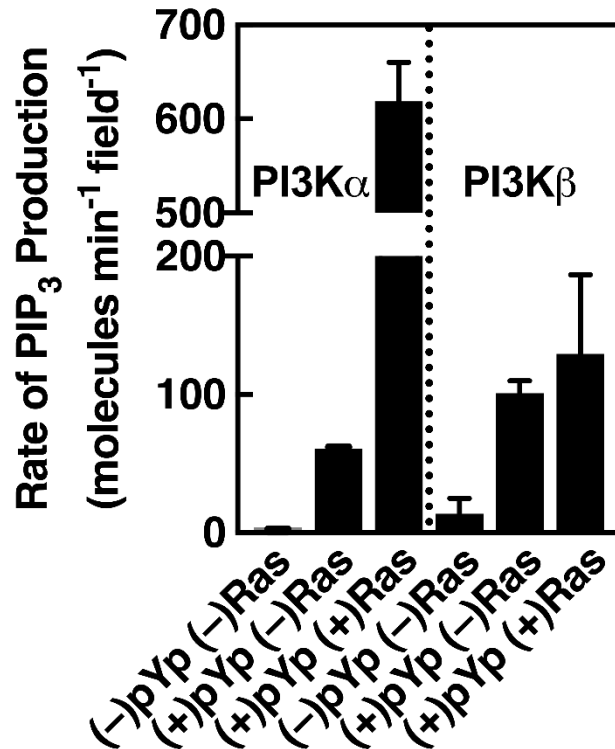


Figure 4.2. PI3K β activity on supported lipid bilayer. PI3K β is active on supported lipid bilayers identical to those used in Chapter II. Basal activity with or without soluble phosphotyrosine peptide is similar to that of PI3K α . However, PI3K β shows no activation by membrane anchored H-Ras, as the RBD of PI3K β is specific for Rac1. N = 3-7. Error bars represent standard deviation.

represent a highly significant target due in part to extensive evidence of PI3K α and PI3K β redundancy (64, 166). Experimentally, an activity assay using fluorescently labeled GRP-PH domain for measuring PIP₃ production, used in chapter II for PI3K α , is fully adaptable to PI3K β (Fig 4.2). Direct membrane binding experiments can be explored with commercially available anti-Rac1 and anti PI3K β antibodies. Alternatively, cloning a Sfp labeling tag (chapter II, appendix H) onto a flexible, exposed loop of PI3K β is more intensive, but provides a suitable secondary approach. This methodology has already been proven to work, being the fluorophore labeling method utilized for PI3K α in Chapter II.

A final module of interest is the class III PI3K enzyme termed VPS34 complex II, which phosphorylates PI to PI-3-P on endosomal membranes and plays vital roles in phagocytosis, autophagy, endosome trafficking, receptor degradation, cytokinesis, signaling, and cytoplasm to vacuole transport (25, 26, 162-164). Activated by the small G protein Rab5, a mechanistic study

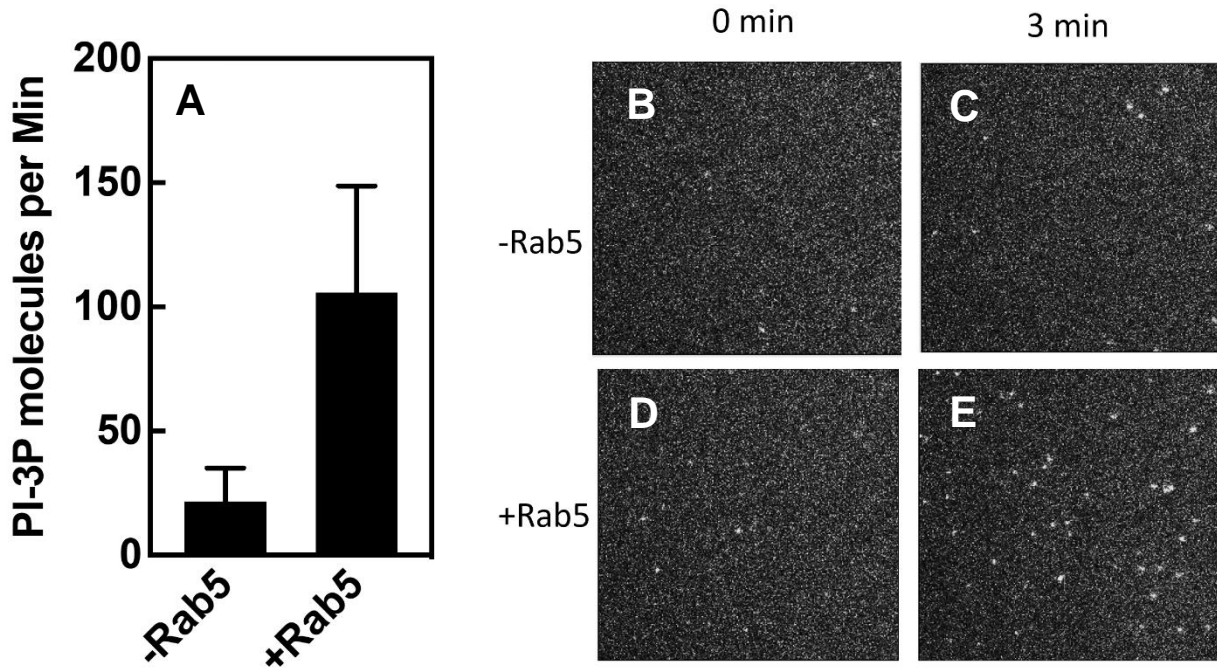


Figure 4.3. Single molecule kinase assay measurements of Rab5 activation of VPS34 complex II. Total internal fluorescence reflection microscopy (TIRFM) measurements of surface tethered Rab5 increases VPS34 complex II lipid kinase activity 5 ± 3 fold relative to VPS34 alone. **(A)** Ten minute kinase assays performed across two days. Bars represent the slope of kinase activity across time. Error bars represent standard deviation. N = 6. **(B,C)** Pictograph still frame representation of kinase activity at 0 (B) and 3 (C) minutes after kinase addition to start assay. **(D,E)** Same as B,C but in the presence of surface-tethered Rab5 lipid bilayers.

similar to that of Chapter II will provide mechanistic insights into important class III PI3K signaling pathways that class I and II PI3Ks do not play a known role in. Summarized here are preliminary studies showing the feasibility of this direction.

Rab5, a Ras superfamily member, is primarily located on early endosomes and recruits VPS34 to the relatively phosphatidylinositol (PI) rich early endosome membrane located on the endoplasmic reticulum. Once located, VPS34 binds the constitutive endosomal lipid PI and generates the important endosomal signaling lipid PI-3-P. In turn, PI-3-P acts as a second

messenger for signaling protein recruitment to the membrane, conscripting PX, FYVE, and PROPPINS domain containing signaling proteins to the endosome (26), similar to the PH domains that PIP lipids recruit to the plasma membrane. Proteins containing these targeting domains are integral to varied cellular processes such as vacuole sorting, endosome to Golgi trafficking, autophagy, and phagocytosis (167-170).

Preliminary data (Fig 4.3) suggests that Rab5 is amenable to membrane anchoring via cysteine coupling to a maleimide lipid headgroup, following the same protocol described for H-Ras in Chapter II. In a single-molecule TIRF microscopy *in vitro* kinase assay, a cysteine-maleimide alexafluor-555 labeled PX domain with high affinity for PI-3-P but little to no affinity for the substrate lipid PI was employed as a sensor to count individual product PI-3-P molecules. Initial experiments (Fig. 4.3) also indicate that VPS34 complex II is active on our supported lipid bilayer system, yielding measurable increases in the density of product PI-3-P with time, and is activated by surface tethered Rab5. Specifically, in these preliminary experiments the presence of surface-tethered Rab5 increases the kinase activity of VPS34 5 ± 3 fold. Here the supported bilayer is composed of 65% DOPC, 27% DOPE, 7% DOPS, 1% PI lipids as a simple endosomal membrane mimic (see Table 1.1 for abbreviations). PI3K activity buffer (Appendix A) was supplemented with 1 mM Mn^{2+} , the preferred divalent for VPS34 activity. Rab5 was tethered in reducing agent-free PI3K buffer for 5 minutes, followed by five buffer wash cycles in 5mM glutathione containing PI3K buffer. This both quenches unreacted maleimide lipid and removes untethered Rab5 from the experiment.

Ongoing studies are devising a strategy to quantify the surface density of Rab5 and VPS34. In particular, it is essential to measure the surface density of VPS34 in order to define its specific kinase activity, in order to resolve the contributions of membrane recruitment and allosteric activation to the mechanism by which Rab5 stimulates VPS34 lipid kinase activity. Toward this end, an alexafluor 555 cysteine-maleimide VPS34 nanobody had good

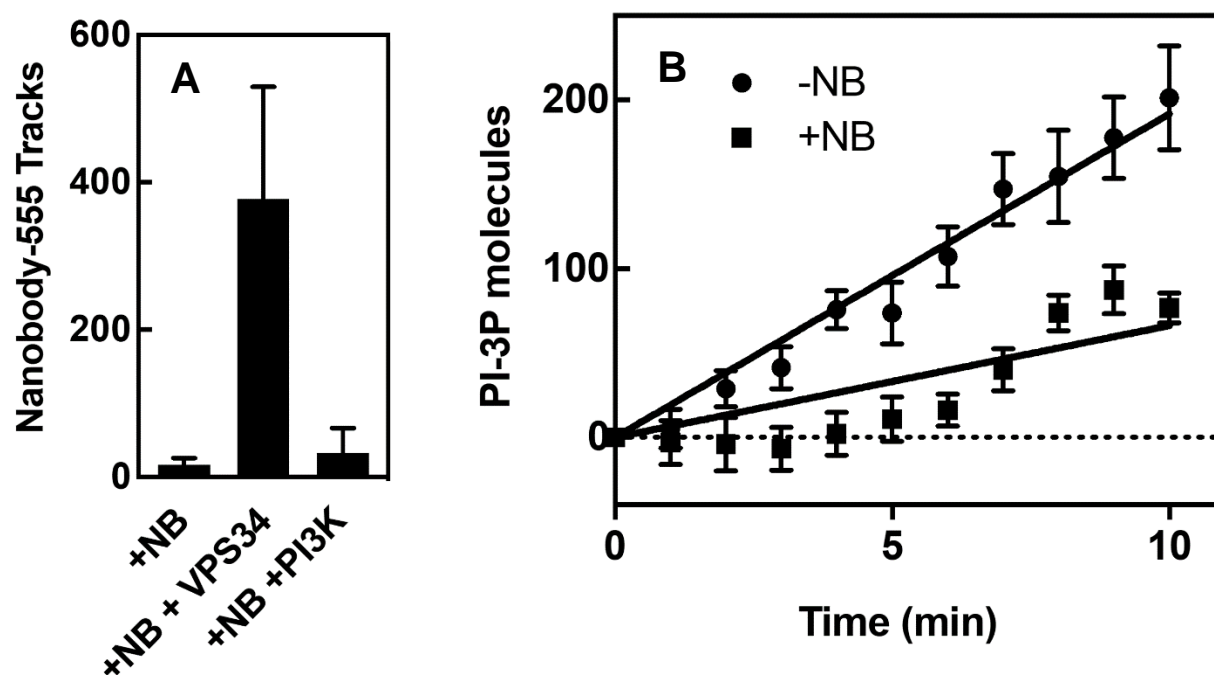


Figure 4.4. Single molecule assay measurements of VPS34-membrane surface binding and effect of fluorescent nanobody on VPS34 kinase activity. Total internal fluorescence reflection microscopy (TIRFM) Surface binding and activity measurements. **(A)** Bars represent membrane surface tracks in the presence of nanobody alone, VPS34, and PI3K α . Error bars represent standard deviation. N = 4. **(B)** Timecourse representation of kinase activity at to 10 minutes after kinase addition to start assay. Error bars represent standard deviation. N = 6.

success in binding VPS34 specifically, relative to PI3K α or membranes alone (Fig. 4.4 A). However, the same nanobody disrupts VPS34 lipid membrane kinase activity (Fig. 4.4 B). This inhibition is significant at 10 minutes into the kinase assay, dropping 2.6 ± 0.5 fold. If this activity loss is due to a nanobody-triggered decrease in VPS34 membrane binding, the measured kinase density would be incorrect. Alternative VPS34 kinase labeling methodologies are being pursued to accurately predict binding. These approaches include fluorophore labeled-antibody detection using commercially available antibodies against Rab5 and VPS34. Such antibodies can be labeled using succinimidyl ester dyes, which covalently react with primary amines. This approach was successfully employed to determine the surface density of H-Ras in Chapter II. Since both lysine side chains and the N-terminal residue amine will become labeled, and the

number of lysine residues in a given antibody will typically not be known in advance, the stoichiometry of labeling should be considered when filtering track data by brightness.

Preliminary and Future Studies of Leading Edge Pseudopod Collapse by Other NSAIDs. Chapter III discussed the inhibitory effect that rapid exposure to therapeutic levels of acetaminophen or ibuprofen have on the leading edge pseudopod of macrophages, likely impeding chemotaxis and the innate immune response. Future studies will address the effects of other common therapeutics on the leading edge pseudopod, starting with other NSAIDs recommended by our clinical advisors (Drs. Ken Hunt, Rachel Frank, and Sourav Poddar). These include: ketorelac; naproxen; meloxicam; celecoxib; prednisone; glucosamine; and cannabidiol (CBD). Like acetaminophen and ibuprofen, some of these compounds may have an inhibitory effect on leukocyte leading edge area and PIP₃, and characterization of additional drugs will help elucidate universal and specialized features of drugs that perturb the leading edge pseudopod. Preliminary evidence from Dr. Brian Ziemba suggests that rapid addition of naproxen collapses the leading edge ($58 \pm 11\%$ drop, $p < 0.02$) (Fig. 4.5 A) while meloxicam and celecoxib both seem to have little or no effect, either in the population or single cell analysis (Fig 4.5 A,B). The extent of naproxen's effect at a population level, and whether it exhibits the same delayed recovery as ibuprofen and acetaminophen, remain to be answered. The procedures detailed in chapter III and appendices F and G can be used as a screening method to identify drugs that perturb the leading edge pseudopod of cultured macrophages. These procedures include both single cell and population level measurements, as they are complementary. The single cell data is better suited to determining the extent of the inhibition on a per cell basis, and for quantifying the drug effects on the PIP₃ signal generated by the leading edge chemosensory pathway, while the population data is better suited to determining the overall drug effect on populations of polarized cells, as well as quantifying adaptation and recovery.

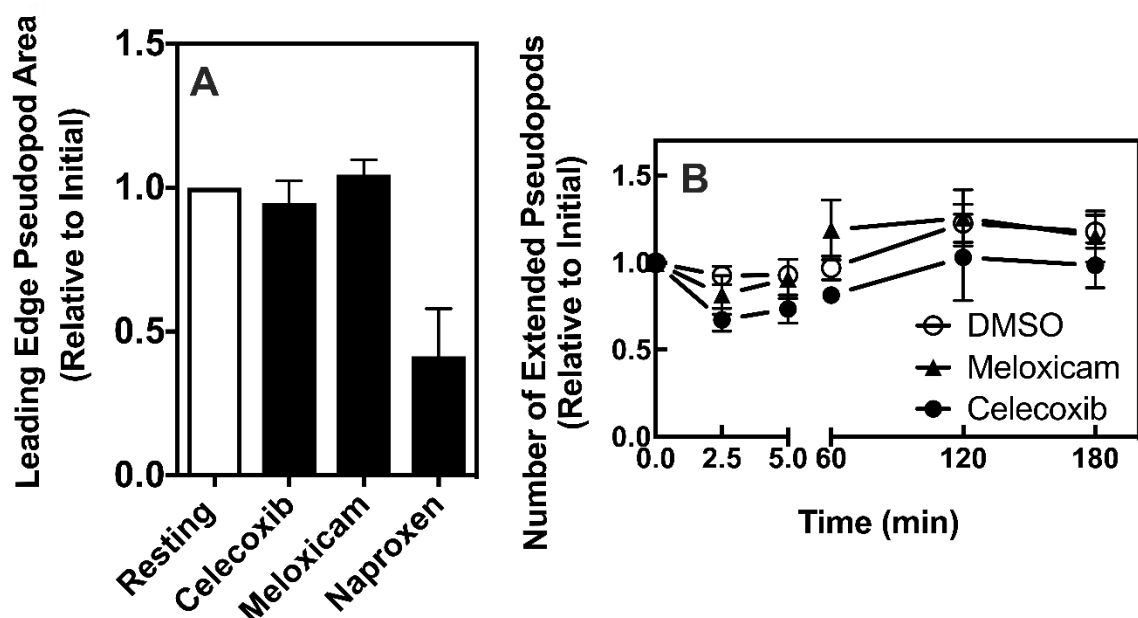


Figure 4.5. Preliminary leading edge pseudopod data for alternate pharmaceuticals. (A) Single-cell data analyzing leading edge area (chapter III) for meloxicam, celecoxib, and racemic naproxen. N = 23 (Naproxen) or 31 (meloxicam, celecoxib). (N represents number of cells analyzed). This panel and data provided by Dr. Brian Ziembra. **(B)** Population level data for rapid addition (chapter III, appendix F) of meloxicam and celecoxib. N = 4 for therapeutics, N = 6 for DMSO (N represents days, with each day encompassing ~1000 cells). Error bars are SEM.

Expanding the Diagnostic Protocol for Characterizing Drug Effects on the Leukocyte Leading Edge Pseudopod. Thus far, the morphology (area) and PIP₃ signal of the leukocyte leading edge pseudopod have been used as proxies to detect drug-induced perturbations of the leading edge signaling pathway that provides pseudopod stability and directs leukocyte chemotaxis. The implementation of a chemotactic assay would complement these observations and would test the prediction that drugs that collapse the leading edge will also inhibit chemotaxis. Specifically, the compounds tested in Chapter III will be subjected to this chemotactic assay to ask whether acetaminophen and ibuprofen block chemotaxis, while aspirin and diclofenac have no effect.

Many commercially available chemotactic assay kits are available, as well as analysis software to quantify population level chemotaxis. Ibidi chemotaxis μ -slides represent a promising assay and software analysis direction, as they offer single-cell resolution and excellent time resolution. In this scenario, typically cells are plated onto a thin, elongated imaging plate. Media containing an attractant (ATP, PDGF, etc.) is added to one end of the plate, and control media on the other. Diffusion through the elongated plate creates a chemical gradient in which the cells will begin to chemotax. The proper substrate, chemotactic agent, and software of choice will require experimentation. Alternatively, Boyden chambers could be employed. These assay chambers require more experimentation to attain time resolution but have a great deal of literature supporting their use across various cell types and attractants. Implementation of this sort of assay is important in bridging the gap between leukocyte leading edges and migration.

Ultimately, the addition of animal studies to the testing protocol will be important to ascertain whether the observed *in vitro* inhibitory effects translate to an *in vivo* setting. In an animal host, for example, the leukocyte will detect competing signals from multiple sources. These can include growth factors and small molecules that signal for leading edge expansion and cell growth, as exemplified by PDGF- $\beta\beta$ in chapter III (Figs. 3.2, 3.3). Moreover, the adaptation pathway of the leukocyte could be operating at different set-points within its range of operation in the *in vitro* and *in vivo* environments, which could make the cell more susceptible to perturbation or less capable of adaptation in one environment of the other. Whether or not the inhibitory effect of NSAIDs and other drugs are impacted by the additional complexities of the *in vivo* environment remain to be tested.

References

1. Miller AF & Falke JJ (2004) Chemotaxis receptors and signaling. *Adv Protein Chem* 68:393-444.
2. Iijima M, Huang YE, & Devreotes P (2002) Temporal and spatial regulation of chemotaxis. *Dev Cell* 3(4):469-478.
3. Devreotes P & Janetopoulos C (2003) Eukaryotic chemotaxis: distinctions between directional sensing and polarization. *J Biol Chem* 278(23):20445-20448.
4. Iglesias PA & Devreotes PN (2008) Navigating through models of chemotaxis. *Curr Opin Cell Biol* 20(1):35-40.
5. Swaney KF, Huang CH, & Devreotes PN (2010) Eukaryotic chemotaxis: a network of signaling pathways controls motility, directional sensing, and polarity. *Annu Rev Biophys* 39:265-289.
6. Korchak HM, Rutherford LE, & Weissmann G (1984) Stimulus response coupling in the human neutrophil. I. Kinetic analysis of changes in calcium permeability. *J Biol Chem* 259(7):4070-4075.
7. Matsuoka S, et al. (2006) Single-molecule analysis of chemoattractant-stimulated membrane recruitment of a PH-domain-containing protein. *J Cell Sci* 119(Pt 6):1071-1079.
8. Ziemba BP & Falke JJ (2018) A PKC-MARCKS-PI3K regulatory module links Ca²⁺ and PIP₃ signals at the leading edge of polarized macrophages. *PLoS One* 13(5):e0196678.
9. Cai H & Devreotes PN (2011) Moving in the right direction: how eukaryotic cells migrate along chemical gradients. *Semin Cell Dev Biol* 22(8):834-841.
10. Devreotes P & Horwitz AR (2015) Signaling networks that regulate cell migration. *Cold Spring Harb Perspect Biol* 7(8):a005959.
11. Loovers HM, et al. (2006) Distinct roles of PI(3,4,5)P₃ during chemoattractant signaling in *Dictyostelium*: a quantitative in vivo analysis by inhibition of PI3-kinase. *Mol Biol Cell* 17(4):1503-1513.
12. Huang YE, et al. (2003) Receptor-mediated regulation of PI3Ks confines PI(3,4,5)P₃ to the leading edge of chemotaxing cells. *Mol Biol Cell* 14(5):1913-1922.
13. Iijima M, Huang YE, Luo HR, Vazquez F, & Devreotes PN (2004) Novel mechanism of PTEN regulation by its phosphatidylinositol 4,5-bisphosphate binding motif is critical for chemotaxis. *J Biol Chem* 279(16):16606-16613.
14. Kamimura Y & Devreotes PN (2010) Phosphoinositide-dependent protein kinase (PDK) activity regulates phosphatidylinositol 3,4,5-trisphosphate-dependent and -independent protein kinase B activation and chemotaxis. *J Biol Chem* 285(11):7938-7946.

15. Lawson MA & Maxfield FR (1995) Ca²⁺- and calcineurin-dependent recycling of an integrin to the front of migrating neutrophils. *Nature* 377(6544):75-79.
16. Peersen OB, Madsen TS, & Falke JJ (1997) Intermolecular tuning of calmodulin by target peptides and proteins: differential effects on Ca²⁺ binding and implications for kinase activation. *Protein Sci* 6(4):794-807.
17. Malmberg NJ, Varma S, Jakobsson E, & Falke JJ (2004) Ca²⁺ activation of the cPLA2 C2 domain: ordered binding of two Ca²⁺ ions with positive cooperativity. *Biochemistry* 43(51):16320-16328.
18. Ziemba BP, Burke JE, Masson G, Williams RL, & Falke JJ (2016) Regulation of PI3K by PKC and MARCKS: Single-Molecule Analysis of a Reconstituted Signaling Pathway. *Biophys J* 110(8):1811-1825.
19. Buckles TC, Ziemba BP, Masson GR, Williams RL, & Falke JJ (2017) Single-Molecule Study Reveals How Receptor and Ras Synergistically Activate PI3K α and PIP3 Signaling. *Biophys J* 113(11):2396-2405.
20. Castellano E & Downward J (2011) RAS Interaction with PI3K: More Than Just Another Effector Pathway. *Genes Cancer* 2(3):261-274.
21. Bamford S, et al. (2004) The COSMIC (Catalogue of Somatic Mutations in Cancer) database and website. *Br J Cancer* 91(2):355-358.
22. UniProt C (2019) UniProt: a worldwide hub of protein knowledge. *Nucleic Acids Res* 47(D1):D506-D515.
23. Jean S & Kiger AA (2014) Classes of phosphoinositide 3-kinases at a glance. *J Cell Sci* 127(Pt 5):923-928.
24. Vanhaesebroeck B, Guillermet-Guibert J, Graupera M, & Bilanges B (2010) The emerging mechanisms of isoform-specific PI3K signalling. *Nat Rev Mol Cell Biol* 11(5):329-341.
25. Backer JM (2008) The regulation and function of Class III PI3Ks: novel roles for Vps34. *Biochem J* 410(1):1-17.
26. Ohashi Y, Tremel S, & Williams RL (2019) VPS34 complexes from a structural perspective. *J Lipid Res* 60(2):229-241.
27. Falasca M & Maffucci T (2012) Regulation and cellular functions of class II phosphoinositide 3-kinases. *Biochem J* 443(3):587-601.
28. Dituri F, et al. (2012) PI3K class IB controls the cell cycle checkpoint promoting cell proliferation in hepatocellular carcinoma. *Int J Cancer* 130(11):2505-2513.
29. Burke JE & Williams RL (2015) Synergy in activating class I PI3Ks. *Trends Biochem Sci* 40(2):88-100.

30. Lemmon MA & Schlessinger J (2010) Cell signaling by receptor tyrosine kinases. *Cell* 141(7):1117-1134.
31. Ferguson KM, et al. (2000) Structural basis for discrimination of 3-phosphoinositides by pleckstrin homology domains. *Mol Cell* 6(2):373-384.
32. Kilic U, et al. (2017) Particular phosphorylation of PI3K/Akt on Thr308 via PDK-1 and PTEN mediates melatonin's neuroprotective activity after focal cerebral ischemia in mice. *Redox Biol* 12:657-665.
33. Han MH, et al. (2016) Flavonoids Isolated from Flowers of *Lonicera japonica* Thunb. Inhibit Inflammatory Responses in BV2 Microglial Cells by Suppressing TNF-alpha and IL-beta Through PI3K/Akt/NF-kb Signaling Pathways. *Phytother Res* 30(11):1824-1832.
34. Li Z, et al. (2016) A positive feedback loop involving EGFR/Akt/mTORC1 and IKK/NF-kB regulates head and neck squamous cell carcinoma proliferation. *Oncotarget* 7(22):31892-31906.
35. Shen J, et al. (2010) ERK- and Akt-dependent neuroprotection by erythropoietin (EPO) against glyoxal-AGEs via modulation of Bcl-xL, Bax, and BAD. *Invest Ophthalmol Vis Sci* 51(1):35-46.
36. Conti S, et al. (2012) Phosphatase and tensin homolog (PTEN) gene mutations and autism: literature review and a case report of a patient with Cowden syndrome, autistic disorder, and epilepsy. *J Child Neurol* 27(3):392-397.
37. Raffone A, et al. (2019) PTEN expression in endometrial hyperplasia and risk of cancer: a systematic review and meta-analysis. *Arch Gynecol Obstet* 299(6):1511-1524.
38. Hu M, Zhu S, Xiong S, Xue X, & Zhou X (2019) MicroRNAs and the PTEN/PI3K/Akt pathway in gastric cancer (Review). *Oncol Rep* 41(3):1439-1454.
39. Xiao J, et al. (2016) PTEN expression is a prognostic marker for patients with non-small cell lung cancer: a systematic review and meta-analysis of the literature. *Oncotarget* 7(36):57832-57840.
40. Yuan TL & Cantley LC (2008) PI3K pathway alterations in cancer: variations on a theme. *Oncogene* 27(41):5497-5510.
41. Zahedi Abghari F, Moradi Y, & Akouchekian M (2019) PTEN gene mutations in patients with macrocephaly and classic autism: A systematic review. *Med J Islam Repub Iran* 33:10.
42. Chen Z, et al. (2005) Crucial role of p53-dependent cellular senescence in suppression of Pten-deficient tumorigenesis. *Nature* 436(7051):725-730.
43. Burke JE & Williams RL (2013) Dynamic steps in receptor tyrosine kinase mediated activation of class IA phosphoinositide 3-kinases (PI3K) captured by H/D exchange (HDX-MS). *Adv Biol Regul* 53(1):97-110.

44. Lee JY, Chiu YH, Asara J, & Cantley LC (2011) Inhibition of PI3K binding to activators by serine phosphorylation of PI3K regulatory subunit p85alpha Src homology-2 domains. *Proc Natl Acad Sci U S A* 108(34):14157-14162.
45. Lemmon MA, Schlessinger J, & Ferguson KM (2014) The EGFR family: not so prototypical receptor tyrosine kinases. *Cold Spring Harb Perspect Biol* 6(4):a020768.
46. Choudhury GG, et al. (1997) PI-3-kinase and MAPK regulate mesangial cell proliferation and migration in response to PDGF. *Am J Physiol* 273(6 Pt 2):F931-938.
47. Amzel LM, et al. (2008) Structural comparisons of class I phosphoinositide 3-kinases. *Nat Rev Cancer* 8(9):665-669.
48. Ren L, Zhou X, Huang X, Wang C, & Li Y (2019) The IRS/PI3K/Akt signaling pathway mediates olanzapine-induced hepatic insulin resistance in male rats. *Life Sci* 217:229-236.
49. Sjolander A, Yamamoto K, Huber BE, & Lapetina EG (1991) Association of p21ras with phosphatidylinositol 3-kinase. *Proc Natl Acad Sci U S A* 88(18):7908-7912.
50. Rodriguez-Viciano P, et al. (1994) Phosphatidylinositol-3-OH kinase as a direct target of Ras. *Nature* 370(6490):527-532.
51. Pacold ME, et al. (2000) Crystal structure and functional analysis of Ras binding to its effector phosphoinositide 3-kinase gamma. *Cell* 103(6):931-943.
52. Denley A, Kang S, Karst U, & Vogt PK (2008) Oncogenic signaling of class I PI3K isoforms. *Oncogene* 27(18):2561-2574.
53. Siempelkamp BD, Rathinaswamy MK, Jenkins ML, & Burke JE (2017) Molecular mechanism of activation of class IA phosphoinositide 3-kinases (PI3Ks) by membrane-localized HRas. *J Biol Chem* 292(29):12256-12266.
54. Guil S, et al. (2003) Alternative splicing of the human proto-oncogene c-H-ras renders a new Ras family protein that trafficks to cytoplasm and nucleus. *Cancer Res* 63(17):5178-5187.
55. Downward J (1997) Role of phosphoinositide-3-OH kinase in Ras signaling. *Adv Second Messenger Phosphoprotein Res* 31:1-10.
56. Castellano E, et al. (2013) Requirement for interaction of PI3-kinase p110alpha with RAS in lung tumor maintenance. *Cancer Cell* 24(5):617-630.
57. Weber KS, et al. (2001) Dual role of H-Ras in regulation of lymphocyte function antigen-1 activity by stromal cell-derived factor-1alpha: implications for leukocyte transmigration. *Mol Biol Cell* 12(10):3074-3086.
58. Yang HW, et al. (2012) Cooperative activation of PI3K by Ras and Rho family small GTPases. *Mol Cell* 47(2):281-290.
59. Anonymous (2019) Avanti Polar Lipids, Inc.

60. Denley A, Gymnopoulos M, Kang S, Mitchell C, & Vogt PK (2009) Requirement of phosphatidylinositol(3,4,5)trisphosphate in phosphatidylinositol 3-kinase-induced oncogenic transformation. *Mol Cancer Res* 7(7):1132-1138.
61. Downward J (2003) Targeting RAS signalling pathways in cancer therapy. *Nat Rev Cancer* 3(1):11-22.
62. Burke JE, Perisic O, Masson GR, Vadas O, & Williams RL (2012) Oncogenic mutations mimic and enhance dynamic events in the natural activation of phosphoinositide 3-kinase p110alpha (PIK3CA). *Proc Natl Acad Sci U S A* 109(38):15259-15264.
63. Burke JE, Perisic O, & Williams RL (2013) Allosteric activation of PI3Kalpha by oncogenic mutations. *Oncotarget* 4(2):180-181.
64. Vadas O, Burke JE, Zhang X, Berndt A, & Williams RL (2011) Structural basis for activation and inhibition of class I phosphoinositide 3-kinases. *Sci Signal* 4(195):re2.
65. Hon WC, Berndt A, & Williams RL (2012) Regulation of lipid binding underlies the activation mechanism of class IA PI3-kinases. *Oncogene* 31(32):3655-3666.
66. Mellor P, Furber LA, Nyarko JN, & Anderson DH (2012) Multiple roles for the p85alpha isoform in the regulation and function of PI3K signalling and receptor trafficking. *Biochem J* 441(1):23-37.
67. Hales EC, Taub JW, & Matherly LH (2014) New insights into Notch1 regulation of the PI3K-AKT-mTOR1 signaling axis: targeted therapy of gamma-secretase inhibitor resistant T-cell acute lymphoblastic leukemia. *Cell Signal* 26(1):149-161.
68. Zhang Y, et al. (2013) Silibinin ameliorates steatosis and insulin resistance during non-alcoholic fatty liver disease development partly through targeting IRS-1/PI3K/Akt pathway. *Int Immunopharmacol* 17(3):714-720.
69. Harrington LS, et al. (2004) The TSC1-2 tumor suppressor controls insulin-PI3K signaling via regulation of IRS proteins. *J Cell Biol* 166(2):213-223.
70. Castellano E & Santos E (2011) Functional specificity of ras isoforms: so similar but so different. *Genes Cancer* 2(3):216-231.
71. Ziemba BP, et al. (2016) Regulation of a Coupled MARCKS-PI3K Lipid Kinase Circuit by Calmodulin: Single-Molecule Analysis of a Membrane-Bound Signaling Module. *Biochemistry* 55(46):6395-6405.
72. Hon WC, Berndt A, & Williams RL (2011) Regulation of lipid binding underlies the activation mechanism of class IA PI3-kinases. *Oncogene*.
73. Jolly LA, Massoll N, & Franco AT (2016) Immune Suppression Mediated by Myeloid and Lymphoid Derived Immune Cells in the Tumor Microenvironment Facilitates Progression of Thyroid Cancers Driven by HrasG12V and Pten Loss. *J Clin Cell Immunol* 7(5).
74. Thorpe LM, Yuzugullu H, & Zhao JJ (2015) PI3K in cancer: divergent roles of isoforms, modes of activation and therapeutic targeting. *Nat Rev Cancer* 15(1):7-24.

75. Kolsch V, Charest PG, & Firtel RA (2008) The regulation of cell motility and chemotaxis by phospholipid signaling. *J Cell Sci* 121(Pt 5):551-559.
76. Gericke A, Leslie NR, Losche M, & Ross AH (2013) PtdIns(4,5)P₂-mediated cell signaling: emerging principles and PTEN as a paradigm for regulatory mechanism. *Adv Exp Med Biol* 991:85-104.
77. Knight JD, Lerner MG, Marcano-Velazquez JG, Pastor RW, & Falke JJ (2010) Single molecule diffusion of membrane-bound proteins: window into lipid contacts and bilayer dynamics. *Biophys J* 99(9):2879-2887.
78. Lin WC, et al. (2014) H-Ras forms dimers on membrane surfaces via a protein-protein interface. *Proc Natl Acad Sci U S A* 111(8):2996-3001.
79. Knight JD & Falke JJ (2009) Single-molecule fluorescence studies of a PH domain: new insights into the membrane docking reaction. *Biophys J* 96(2):566-582.
80. Kalb E, Frey S, & Tamm LK (1992) Formation of supported planar bilayers by fusion of vesicles to supported phospholipid monolayers. *Biochim Biophys Acta* 1103(2):307-316.
81. Nair PM, Salaita K, Petit RS, & Groves JT (2011) Using patterned supported lipid membranes to investigate the role of receptor organization in intercellular signaling. *Nat Protoc* 6(4):523-539.
82. Ziemba BP, Knight JD, & Falke JJ (2012) Assembly of membrane-bound protein complexes: detection and analysis by single molecule diffusion. *Biochemistry* 51(8):1638-1647.
83. Sbalzarini IF & Koumoutsakos P (2005) Feature point tracking and trajectory analysis for video imaging in cell biology. *J Struct Biol* 151(2):182-195.
84. Gureasko J, et al. (2008) Membrane-dependent signal integration by the Ras activator Son of sevenless. *Nat Struct Mol Biol* 15(5):452-461.
85. Nan X, et al. (2015) Ras-GTP dimers activate the Mitogen-Activated Protein Kinase (MAPK) pathway. *Proc Natl Acad Sci U S A* 112(26):7996-8001.
86. Haugh JM, Huang AC, Wiley HS, Wells A, & Lauffenburger DA (1999) Internalized epidermal growth factor receptors participate in the activation of p21(ras) in fibroblasts. *J Biol Chem* 274(48):34350-34360.
87. Corbin JA, Dirx RA, & Falke JJ (2004) GRP1 pleckstrin homology domain: activation parameters and novel search mechanism for rare target lipid. *Biochemistry* 43(51):16161-16173.
88. Ferrell JE, Jr. & Huestis WH (1984) Phosphoinositide metabolism and the morphology of human erythrocytes. *J Cell Biol* 98(6):1992-1998.
89. Hagelberg C & Allan D (1990) Restricted diffusion of integral membrane proteins and polyphosphoinositides leads to their depletion in microvesicles released from human erythrocytes. *Biochem J* 271(3):831-834.

90. Ziemba BP & Falke JJ (2013) Lateral diffusion of peripheral membrane proteins on supported lipid bilayers is controlled by the additive frictional drags of (1) bound lipids and (2) protein domains penetrating into the bilayer hydrocarbon core. *Chem Phys Lipids* 172-173:67-77.
91. Wu D (2005) Signaling mechanisms for regulation of chemotaxis. *Cell Res* 15(1):52-56.
92. Charest PG & Firtel RA (2006) Feedback signaling controls leading-edge formation during chemotaxis. *Curr Opin Genet Dev* 16(4):339-347.
93. Stephens L, Milne L, & Hawkins P (2008) Moving towards a better understanding of chemotaxis. *Curr Biol* 18(11):R485-494.
94. Majumdar R, Sixt M, & Parent CA (2014) New paradigms in the establishment and maintenance of gradients during directed cell migration. *Curr Opin Cell Biol* 30:33-40.
95. Graziano BR & Weiner OD (2014) Self-organization of protrusions and polarity during eukaryotic chemotaxis. *Curr Opin Cell Biol* 30:60-67.
96. Rosowski EE, Deng Q, Keller NP, & Huttenlocher A (2016) Rac2 Functions in Both Neutrophils and Macrophages To Mediate Motility and Host Defense in Larval Zebrafish. *J Immunol* 197(12):4780-4790.
97. Giese M, Hind L, & Huttenlocher A (2019) Neutrophil plasticity in the tumor microenvironment. *Blood*.
98. Niggli V (2003) Signaling to migration in neutrophils: importance of localized pathways. *Int J Biochem Cell Biol* 35(12):1619-1638.
99. Stramer B, et al. (2005) Live imaging of wound inflammation in *Drosophila* embryos reveals key roles for small GTPases during in vivo cell migration. *J Cell Biol* 168(4):567-573.
100. Wei C, et al. (2009) Calcium flickers steer cell migration. *Nature* 457(7231):901-905.
101. Rossaint J, Margraf A, & Zarbock A (2018) Role of Platelets in Leukocyte Recruitment and Resolution of Inflammation. *Front Immunol* 9:2712.
102. Hopkin SJ, Lewis JW, Krautter F, Chimen M, & McGettrick HM (2019) Triggering the Resolution of Immune Mediated Inflammatory Diseases: Can Targeting Leukocyte Migration Be the Answer? *Front Pharmacol* 10:184.
103. Falke JJ & Ziemba BP (2014) Interplay between phosphoinositide lipids and calcium signals at the leading edge of chemotaxing ameboid cells. *Chem Phys Lipids* 182:73-79.
104. Goodwin JS (1984) Mechanism of action of nonsteroidal anti-inflammatory agents. *Am J Med* 77(1A):57-64.
105. Vane JR & Botting RM (1998) Mechanism of action of nonsteroidal anti-inflammatory drugs. *Am J Med* 104(3A):2S-8S; discussion 21S-22S.

106. Gunaydin C & Bilge SS (2018) Effects of Nonsteroidal Anti-Inflammatory Drugs at the Molecular Level. *Eurasian J Med* 50(2):116-121.
107. Wang Y, Chen CL, & Iijima M (2011) Signaling mechanisms for chemotaxis. *Dev Growth Differ* 53(4):495-502.
108. Wei C, Wang X, Zheng M, & Cheng H (2012) Calcium gradients underlying cell migration. *Curr Opin Cell Biol* 24(2):254-261.
109. Gambardella L & Vermeren S (2013) Molecular players in neutrophil chemotaxis--focus on PI3K and small GTPases. *J Leukoc Biol* 94(4):603-612.
110. Ziemba BP, et al. (2014) Single-molecule studies reveal a hidden key step in the activation mechanism of membrane-bound protein kinase C- α . *Biochemistry* 53(10):1697-1713.
111. Petri B & Sanz MJ (2018) Neutrophil chemotaxis. *Cell Tissue Res* 371(3):425-436.
112. Klippel A, et al. (1998) Activation of phosphatidylinositol 3-kinase is sufficient for cell cycle entry and promotes cellular changes characteristic of oncogenic transformation. *Mol Cell Biol* 18(10):5699-5711.
113. Evans JH, Murray D, Leslie CC, & Falke JJ (2006) Specific translocation of protein kinase C α to the plasma membrane requires both Ca²⁺ and PIP₂ recognition by its C2 domain. *Mol Biol Cell* 17(1):56-66.
114. Roose JP, Mollenauer M, Ho M, Kurosaki T, & Weiss A (2007) Unusual interplay of two types of Ras activators, RasGRP and SOS, establishes sensitive and robust Ras activation in lymphocytes. *Mol Cell Biol* 27(7):2732-2745.
115. Evans JH & Falke JJ (2007) Ca²⁺ influx is an essential component of the positive-feedback loop that maintains leading-edge structure and activity in macrophages. *Proc Natl Acad Sci U S A* 104(41):16176-16181.
116. Corbin JA, Evans JH, Landgraf KE, & Falke JJ (2007) Mechanism of specific membrane targeting by C2 domains: localized pools of target lipids enhance Ca²⁺ affinity. *Biochemistry* 46(14):4322-4336.
117. Balla T (2013) Phosphoinositides: tiny lipids with giant impact on cell regulation. *Physiol Rev* 93(3):1019-1137.
118. Hawkins PT & Stephens LR (2015) PI3K signalling in inflammation. *Biochim Biophys Acta* 1851(6):882-897.
119. Pendin D, Greotti E, Lefkimmatis K, & Pozzan T (2017) Exploring cells with targeted biosensors. *J Gen Physiol* 149(1):1-36.
120. Miyanaga Y, Kamimura Y, Kuwayama H, Devreotes PN, & Ueda M (2018) Chemoattractant receptors activate, recruit and capture G proteins for wide range chemotaxis. *Biochem Biophys Res Commun* 507(1-4):304-310.

121. Li X, et al. (2018) Mutually inhibitory Ras-PI(3,4)P2 feedback loops mediate cell migration. *Proc Natl Acad Sci U S A* 115(39):E9125-E9134.
122. Dickson EJ & Hille B (2019) Understanding phosphoinositides: rare, dynamic, and essential membrane phospholipids. *Biochem J* 476(1):1-23.
123. Cantley J (2014) The control of insulin secretion by adipokines: current evidence for adipocyte-beta cell endocrine signalling in metabolic homeostasis. *Mamm Genome* 25(9-10):442-454.
124. Hart FD & Huskisson EC (1984) Non-steroidal anti-inflammatory drugs. Current status and rational therapeutic use. *Drugs* 27(3):232-255.
125. Janssen GM & Venema JF (1985) Ibuprofen: plasma concentrations in man. *J Int Med Res* 13(1):68-73.
126. Davies NM & Anderson KE (1997) Clinical pharmacokinetics of diclofenac. Therapeutic insights and pitfalls. *Clin Pharmacokinet* 33(3):184-213.
127. Regenthal R, Krueger M, Koepfel C, & Preiss R (1999) Drug levels: therapeutic and toxic serum/plasma concentrations of common drugs. *J Clin Monit Comput* 15(7-8):529-544.
128. Rao P & Knaus EE (2008) Evolution of nonsteroidal anti-inflammatory drugs (NSAIDs): cyclooxygenase (COX) inhibition and beyond. *J Pharm Pharm Sci* 11(2):81s-110s.
129. Zhou Y, Boudreau DM, & Freedman AN (2014) Trends in the use of aspirin and nonsteroidal anti-inflammatory drugs in the general U.S. population. *Pharmacoepidemiol Drug Saf* 23(1):43-50.
130. Davis JS, et al. (2017) Use of non-steroidal anti-inflammatory drugs in US adults: changes over time and by demographic. *Open Heart* 4(1):e000550.
131. Kundra V, et al. (1994) Regulation of chemotaxis by the platelet-derived growth factor receptor-beta. *Nature* 367(6462):474-476.
132. Kundra V, Anand-Apte B, Feig LA, & Zetter BR (1995) The chemotactic response to PDGF-BB: evidence of a role for Ras. *J Cell Biol* 130(3):725-731.
133. Le ADK, Enweze L, DeBaun MR, & Dragoo JL (2018) Current Clinical Recommendations for Use of Platelet-Rich Plasma. *Curr Rev Musculoskelet Med* 11(4):624-634.
134. Kia C, et al. (2018) Platelet-Rich Plasma: Review of Current Literature on its Use for Tendon and Ligament Pathology. *Curr Rev Musculoskelet Med* 11(4):566-572.
135. Chen MR & Dragoo JL (2013) The effect of nonsteroidal anti-inflammatory drugs on tissue healing. *Knee Surg Sports Traumatol Arthrosc* 21(3):540-549.
136. Clemens DL & Horwitz MA (2007) Uptake and intracellular fate of *Francisella tularensis* in human macrophages. *Ann N Y Acad Sci* 1105:160-186.

137. Altman A & Kong KF (2014) Protein kinase C inhibitors for immune disorders. *Drug Discov Today* 19(8):1217-1221.
138. Matsuoka S & Ueda M (2018) Mutual inhibition between PTEN and PIP3 generates bistability for polarity in motile cells. *Nat Commun* 9(1):4481.
139. Walker EH, et al. (2000) Structural determinants of phosphoinositide 3-kinase inhibition by wortmannin, LY294002, quercetin, myricetin, and staurosporine. *Mol Cell* 6(4):909-919.
140. Falke JJ, Bass RB, Butler SL, Chervitz SA, & Danielson MA (1997) The two-component signaling pathway of bacterial chemotaxis: a molecular view of signal transduction by receptors, kinases, and adaptation enzymes. *Annu Rev Cell Dev Biol* 13:457-512.
141. Foxman EF, Kunkel EJ, & Butcher EC (1999) Integrating conflicting chemotactic signals. The role of memory in leukocyte navigation. *J Cell Biol* 147(3):577-588.
142. Von Philipsborn A & Bastmeyer M (2007) Mechanisms of gradient detection: a comparison of axon pathfinding with eukaryotic cell migration. *Int Rev Cytol* 263:1-62.
143. Takeda K, et al. (2012) Incoherent feedforward control governs adaptation of activated ras in a eukaryotic chemotaxis pathway. *Sci Signal* 5(205):ra2.
144. Munita JM & Arias CA (2016) Mechanisms of Antibiotic Resistance. *Microbiol Spectr* 4(2).
145. Mansoori B, Mohammadi A, Davudian S, Shirjang S, & Baradaran B (2017) The Different Mechanisms of Cancer Drug Resistance: A Brief Review. *Adv Pharm Bull* 7(3):339-348.
146. Ong CK, Lirk P, Tan CH, & Seymour RA (2007) An evidence-based update on nonsteroidal anti-inflammatory drugs. *Clin Med Res* 5(1):19-34.
147. Bushra R & Aslam N (2010) An overview of clinical pharmacology of Ibuprofen. *Oman Med J* 25(3):155-1661.
148. Mazaleuskaya LL, et al. (2015) PharmGKB summary: pathways of acetaminophen metabolism at the therapeutic versus toxic doses. *Pharmacogenet Genomics* 25(8):416-426.
149. Hunter TS, Robison C, & Gerbino PP (2015) Emerging evidence in NSAID pharmacology: important considerations for product selection. *Am J Manag Care* 21(7 Suppl):S139-147.
150. Moore RA, Derry S, Wiffen PJ, & Straube S (2015) Effects of food on pharmacokinetics of immediate release oral formulations of aspirin, dipyrrone, paracetamol and NSAIDs - a systematic review. *Br J Clin Pharmacol* 80(3):381-388.
151. Calatayud S & Esplugues JV (2016) Chemistry, Pharmacodynamics, and Pharmacokinetics of NSAIDs. *NSAIDs and Aspirin: Recent Advances and Implications for Clinical Management*, ed Lanás A (Springer International Publishing, Cham), pp 3-16.

152. Dimova S, Hoet PH, Dinsdale D, & Nemery B (2005) Acetaminophen decreases intracellular glutathione levels and modulates cytokine production in human alveolar macrophages and type II pneumocytes in vitro. *Int J Biochem Cell Biol* 37(8):1727-1737.
153. Liao XH, et al. (2016) A High-Throughput, Multi-Cell Phenotype Assay for the Identification of Novel Inhibitors of Chemotaxis/Migration. *Sci Rep* 6:22273.
154. Fritsch R, et al. (2013) RAS and RHO families of GTPases directly regulate distinct phosphoinositide 3-kinase isoforms. *Cell* 153(5):1050-1063.
155. Prakash P, Zhou Y, Liang H, Hancock JF, & Gorfe AA (2016) Oncogenic K-Ras Binds to an Anionic Membrane in Two Distinct Orientations: A Molecular Dynamics Analysis. *Biophys J* 110(5):1125-1138.
156. Zhang M, Jang H, & Nussinov R (2019) The structural basis for Ras activation of PI3Kalpha lipid kinase. *Phys Chem Chem Phys* 21(22):12021-12028.
157. Miller MS, et al. (2014) Structural basis of nSH2 regulation and lipid binding in PI3Kalpha. *Oncotarget* 5(14):5198-5208.
158. Dbouk HA, Vadas O, Williams RL, & Backer JM (2012) PI3Kbeta downstream of GPCRs - crucial partners in oncogenesis. *Oncotarget* 3(12):1485-1486.
159. Dbouk HA, et al. (2012) G protein-coupled receptor-mediated activation of p110beta by Gbetagamma is required for cellular transformation and invasiveness. *Sci Signal* 5(253):ra89.
160. Dou Z, et al. (2010) The class IA phosphatidylinositol 3-kinase p110-beta subunit is a positive regulator of autophagy. *J Cell Biol* 191(4):827-843.
161. Dou Z, et al. (2013) Class IA PI3K p110beta subunit promotes autophagy through Rab5 small GTPase in response to growth factor limitation. *Mol Cell* 50(1):29-42.
162. Parekh VV, et al. (2013) Impaired autophagy, defective T cell homeostasis, and a wasting syndrome in mice with a T cell-specific deletion of Vps34. *J Immunol* 190(10):5086-5101.
163. Rostislavleva K, et al. (2015) Structure and flexibility of the endosomal Vps34 complex reveals the basis of its function on membranes. *Science* 350(6257):aac7365.
164. Ohashi Y, et al. (2016) Characterization of Atg38 and NRBF2, a fifth subunit of the autophagic Vps34/PIK3C3 complex. *Autophagy* 12(11):2129-2144.
165. Weber PC, Ohlendorf DH, Wendoloski JJ, & Salemme FR (1989) Structural origins of high-affinity biotin binding to streptavidin. *Science* 243(4887):85-88.
166. Singh P, Dar MS, & Dar MJ (2016) p110alpha and p110beta isoforms of PI3K signaling: are they two sides of the same coin? *FEBS Lett* 590(18):3071-3082.
167. Patki V, et al. (1997) Identification of an early endosomal protein regulated by phosphatidylinositol 3-kinase. *Proc Natl Acad Sci U S A* 94(14):7326-7330.

168. Simonsen A, et al. (1998) EEA1 links PI(3)K function to Rab5 regulation of endosome fusion. *Nature* 394(6692):494-498.
169. Komada M & Soriano P (1999) Hrs, a FYVE finger protein localized to early endosomes, is implicated in vesicular traffic and required for ventral folding morphogenesis. *Genes Dev* 13(11):1475-1485.
170. Simonsen A, et al. (2004) Alfy, a novel FYVE-domain-containing protein associated with protein granules and autophagic membranes. *J Cell Sci* 117(Pt 18):4239-4251.
171. Schutz GJ, Schindler H, & Schmidt T (1997) Single-molecule microscopy on model membranes reveals anomalous diffusion. *Biophys J* 73(2):1073-1080.
172. Saffman PG & Delbruck M (1975) Brownian motion in biological membranes. *Proceedings of the National Academy of Sciences of the United States of America* 72(8):3111-3113.
173. Peters R & Cherry RJ (1982) Lateral and rotational diffusion of bacteriorhodopsin in lipid bilayers: experimental test of the Saffman-Delbruck equations. *Proceedings of the National Academy of Sciences of the United States of America* 79(14):4317-4321.
174. Berg HC (1983) *Random Walks in Biology*.
175. Einstein A (1926) *Investigations On The Theory Of Brownian Movement*. *Annalen der Physik*.
176. Evans, E. and E. Sackmann, 1988, Translational and rotational drag coefficients for a disk moving in a liquid membrane associated with a rigid substrate, *J. Fluid Mech.*194, 553–561.
177. Hughes, B.D., B.A. Pailthorpe and L.R. White, 1981, The translational and rotational drag on a cylinder moving in a membrane, *J. Fluid Mech.*110, 349–372.
178. Saffman, P.G., 1976, Brownian motion in thin sheets of viscous fluid, *J. Fluid Mech.*73, 593–602.

APPENDIX A.

Protocol for Liposome Creation and Deposition for Single Molecule TIRF Fluorescence

Tracking

I. Prepare liposomes

FBVI buffer

25mM HEPES pH 7.3

140mM KCl

15mM NaCl

5mM MgCl₂

0.2 micron filtered.

PI3K buffer

50mM HEPES pH 6.9

1mM CaCl₂

1mM EGTA

0.5mM MgCl₂

15mM NaCl

100mM KCl

0.2 micron filtered.

*Use only non-autoclaved pipet tips or syringes for transferring lipids, e.g. TipOne pre-sterilized filter tips.

1. Mix lipids from chloroform stocks to the desired ratio in standard dark tubes. If using PIP lipids in powder form, add 100 μ L chloroform:methanol:water (20:9:1, v/v, single-molecule dedicated, spectroscopic grade). Vortex well and add to chloroform lipid mixture. Repeat "rinse" three times. Typically, we use molar 1% Maleimide, 1% PIP₂, and/or 1% PIP₃.

2. Dry on speed-vac for ≥ 2 h. When finished there should be a film on the bottom of the tube, no liquid.
3. Hydrate with FBVI buffer for a final lipid concentration of 3 mM. If maleimide lipid included, make sure to leave out reducing agent.
4. Fully resuspend lipid (MLVs) by vortexing 5x 5 min. Alternatively and/or in addition add freeze-thaw cycles: Vortex ~ 1 min, freeze in LN₂, thaw at 37°C, repeat. Keep at -80°C or proceed to sonication.
5. Sonicate on ice with microtip at power 4. Tip should be midway into sample. Listen for strong hiss sound. Duty cycle 0.6s on, 1.2 s off, total sonication time 4 min. Before sonication you should not be able to see through the sample well enough to detect the gradations on the other side of the tube. Sample should be relatively transparent with gradations visible following sonication, although the SUVs of some lipid compositions are sometimes slightly cloudy. We have not noticed that slight cloudiness has a negative effect on bilayer formation. Use day of sonication, or day after.

*Previous lab members have successfully stored sonicated liposomes at 4°C for ~ 1 week. This author has no experience with this method.

*For Ca-free work, add ~ 0.1 mg chelex beads to liposome stock and rotate for 1 hr. before using.

II. Prepare glass via piranha etch –use this to clean and prepare surface for bilayer

1. Put on nitrile gloves and rinse in diH₂O with scrubbing to remove soapy film, dry with clean paper towels.
2. Spray dust and smudges from each cover slip (22x22mm, #1.5 (refer to 0.16-0.19 mm thick)) using pressurized N₂, double check cleanliness by holding up to light and put in metal rack. It is recommended to prepare $\sim 1.5x$ the number of cover slips needed for bilayers.

3. Prepare piranha solution (3:1 conc. H_2SO_4 : 30% H_2O_2), stand cover slips in 20 ml beaker (Can fit up to 3 per beaker using an inverted pyramid – make sure all surfaces of slide are exposed), pour in piranha to cover and soak for 1 hr. Also soak metal tweezer tips in small amount of solution. Caution: piranha solution is extremely acidic and a strong oxidizer. Use metal forceps to handle cover slips in acid. Note piranha will burn through clothing and eventually through nitrile gloves. Latex gloves do not offer sufficient protection.
4. Meanwhile, attach a clean glass Pasteur pipet to N_2 tank hose for drying slides.
5. After one hour, use metal forceps to remove each slip, handling each near the edge. Rinse each side into designated waste beaker using Milli-Q H_2O wash bottle, ensuring no significant amount of piranha solution is still attached. Place in a metal rack submerged in Milli-Q H_2O . When all are in rack, take to sink and rinse 3x on each side with Milli-Q water directly from filter, maneuvering the slips back and forth through the stream, being careful to rinse all surfaces and to not allow significant water to pass from gloves to cover slips. After rinse, dry slips immediately (Nitrogen gas) unless using Ca-free conditions (if required).
**For Ca-free work, soak in 0.1M EDTA in Milli-Q water 1 hr at 4°C , then rinse with Ca-free water.
6. Dry under nitrogen stream, working quickly to ensure that water is first blown down to the bottom corner of each coverslip so contaminants don't dry in center. Direct air flow downward onto the slips at ~5-10 psi. Place rack with dry slips in dry tip box for transport.
*Directly perpendicular N_2 gas on the slide will break the slide at the tweezers. Blow at a more obtuse angle.
7. Take dry slips to UV oven, clean slides in rack 0.8 hr (to overnight) in ozone (UV) cleaner. Place the rack under the chamber, make sure UV is on, then push the trigger button. The blue indicator light on the chamber should be on when in progress.
*Typically, this author would clean slides a day prior to experimentation, leaving them in the UV oven overnight, but would sonicate fresh liposomes the morning of experimentation.

III. Deposit bilayers

1. Change to a new pair of powder-free latex gloves.
2. Cut apart perfusion chambers from Invitrogen (C-18139) and peel off the protective liner from the chamber using metal forceps.)

*For Ca-free work, soak in 0.1M EDTA \geq 1 hr.

3. Rinse/wet perfusion chambers with Milli-Q H₂O (Ca-free if desired)
4. Spray perfusion chamber dry with N₂ and set perfusion chamber upside-down on lens paper.
Then take a coverslip and confirm cleanliness by holding up to light to ensure that center of slip is free from dust and smudges. Press a clean coverslip on top of the perfusion chamber and visually confirm the seal. Press gently to ensure good seal. Flip the slide over, label on the edge of the coverslip. Cover prepared slides with a weighing tray to protect from dust.

5. In a non-autoclaved 1.5 ml Eppendorf tube, mix 35 μ L liposome stock with 35 μ L bilayer deposition buffer for every sample slide desired. Pipette up and down to mix.

*If lipids contain significant PE, typically solution will become cloudy / opaque. This is normal.

*Deposition buffer = 1xFBVI + 1M NaCl)

*Run through 0.2 micron filter before mixing with liposomes

* The perfusion chamber can hold \sim 35 μ L. To avoid evaporation, increase the volume of the liposome solution to \sim 50-60 μ L total.

6. Inject liposome suspension into perfusion chambers. If air gaps or bubbles are present the suspension may be pipetted back and forth carefully before bilayer deposition commences.

* It is beneficial to add to the near side of the chamber, such that the “bubble” of extra buffer is on the far side of the chamber. The lipids will deposit where the bubble is present, aiding in the breaking of surface tension. If these are both on the near side of the chamber, the two near side bubbles could mix during experimentation.

7. Incubate 30 min. at room temperature, covered to protect from dust.

8. Rinse sample ~20 s with fresh Milli-Q water from a wash bottle with a non-autoclaved tip at the spout (Ca free if desired) in order to remove liposomes in solution or adhered nonspecifically to the bilayer.

* Holding each slide between the thumb and forefinger, generate a stream of water from the wash bottle by applying constant pressure and make sure no air bubbles are in the tip.

Rotate the slide between the 11 o'clock and 1 o'clock position in order to wash down each side of the perfusion chamber interior.

*No air bubbles in perfusion chamber! (small bubbles adhered to top side of perfusion chamber ok, but not ok if the bilayer is exposed to air)

9. Be sure to add ~100 ug/mL ultrapure BSA to block bilayer prior to imaging

10. Blot dry any water from sides and bottom of coverslip with a Kimwipe and add a small drop of water to the top of the perfusion chamber so that the sample will not dry out before imaging. Protect slides from dust prior to imaging.

APPENDIX B.

Anchoring Small G-Protein (Ras) to Surface (Maleimide lipids)

1. Prepare liposomes as in Appendix A, ensuring no reducing agent comes in contact with maleimide lipid. Typically 1 molar percent maleimide lipid was incorporated. Avanti lipid #780201 was typically used (1,2-dioleoyl-sn-glycero-3-phosphoethanolamine-N-[4-(p-maleimidomethyl)cyclohexane-carboxamide])
2. Having taken care to never have exposed the Ras stock or maleimide lipids to any reducing agent save low mM TCEP, exchange deposited lipids into 1xPI3K Buffer pH 6.9. Maleimide reactions are cystine specific especially when the pH is 6.5 – 7. This means that when the activity buffer is pH 8.0, as in VPS34, an additional more acidic buffer must be prepared for the conjugation phase.
3. Add H-Ras to a final concentration of ~ 5 μ M and cycle through perfusion chamber. Other G-proteins may need different conjugation concentrations.
4. Allow Maleimide coupling reaction to proceed for 5 min (at room temperature, undisturbed).
5. Wash out excess soluble Ras with PI3K buffer (5x 50uL exchanges)
6. Quench excess maleimide with reducing agent (We typically use 5mM Glutathione).

*To quench, typically this author would exchange into a PI3K buffer pH 6.9 with 5mM glutathione added, rather than adding glutathione directly.

*This author conjugated each experiment just prior to imaging, rather than all experiments at once.

APPENDIX C.

TIRF Microscope Setup and Use (Homebuilt Nikon TE-2000)

- *Protect your eyes – direct laser beam will cause blindness.
- *Protect the objective from scratches, the CCD camera from excess light, and the laser from power fluctuations – these are the most costly and easily damaged components.
- *Monitoring temperature in room over the course of the experiment recommended – should stay constant at ~71° F (see thermostat on wall) but can vary slightly.
- * When using fluorescent proteins, less is more. Begin with single nanomolar amounts of fluorescent protein, diluted 1:10 dark protein to begin with, and titrate up or down.

Microscope set-up and TIRFM measurements

1. First check that CCD camera is off. Lower all ND filters into beampath. Choose high power green laser or low power red / green combination. Then turn on the power supply for the laser source.
2. Take OD 2.0 filter out of beampath. Adjust defocusing stage until spot is vertical.
3. Remove anything from top of microscope and adjust positioning of defocusing lens so that the beam is centered on the spot marked on the ceiling and has a symmetrical diffraction pattern. Usually this can be done with just the finger screws on the defocusing lens, but if necessary, the lens mount can be moved a few mm. If the diffraction pattern is extremely asymmetric then clean the microscope objective (Methanol and lens paper).
4. Measure the laser power: using the power meter to measure the intensity coming out directly from the laser beam and the power coming from the objective.
5. Put all the filters down, block the laser beam, put the stage back, cover the objective with the cap, double check that the CCD camera is off and make sure scope output setting is #4 to direct the image into the T.V. With the dark box closed, turn on the EMCCD camera.

5. On the computer open the program NIS. Wait a few minutes for the temperature of the EMCCD camera cool down to -70 deg. Double check / adjust experimental parameters such as exposure time, binning mode, capture duration, etc.
6. Insert sample onto center of metal disc. If smudged, wipe the back of coverslip with methanol (wash bottle filled with spectroscopic grade MeOH) using the cotton-tipped applicator. This is a rare occurrence.
7. Holding the dropper / stick ~1 cm above the objective, carefully drop one drop of the immersion oil onto the center of the objective (the oil has same reflective index as the objective). Be careful not to touch the objective with the dropper to avoid scratching the objective and cross-contamination of the oil in the dropper. Then, make sure the objective is down, and put the sample chamber on the stage. Watching the sample chamber and objective, carefully raise the objective until the oil contacts the coverslip.
8. Put all the neutral density filters down into the beam (OD 3.8), make sure the scope setting is #4 directing the image into the T.V., rotate the defocus lens out of beam. Then adjust the scope focus, slowly and carefully moving the objective up, until the laser light appears in the eyepiece. Adjust focus using first the coarse, then fine adjustment knobs until a green X with is observed. If you miss the green X and continue moving the objective up it will strike the cover slip, raising the sample chamber – immediately move the objective down and start over.
9. Turn room lights off. Rotate the defocus lens back into the beam and switch the scope setting to #3 to direct image into CCD camera. View live image on NIS and autoscale lookup tables.
10. To switch from epifluorescence mode to TIR mode, go to the back of the laser table and adjust the beam angle by moving the single-axis translation stage to the right until the return beam spot is observed at the back of the scope and optimize the brightness and roundness of this spot.

11. Perform steps 6-9 to put on sample. Adjust focus based on the on-screen image, and take one initial movie (see step 14, OD 1.3-1.5) to record the background contamination. Monitor the image and consider using another sample if contamination levels in water are high.
 12. Find a suitable field with mobile particles, photobleach, block laser and recover ~1 min., focus and record movie.
- * To add desired protein to sample, prepare a dilution of the protein prior to imaging by adding concentrated stock to proper volume of assay buffer. Add desired amount of dilute protein to the small excess buffer bubble and cycle through the chamber at least 5 times to ensure good mixing.
13. To change the sample, block the laser beam, adjust the scope setting to #4, turn the room lights on, move the objective down, and remove chamber. After replacing the sample with a new one, put the chamber back on the scope and repeat steps 6-10 except that new objective oil may only be needed only every 2-3 samples.

Powering down and cleaning the microscope

1. When finished with final sample, move the objective down and remove sample, turn off laser(s), and turn off the power supply(s). Last, turn off the EMCCD camera.
2. To clean the objective without scratching it, first raise it above the stage where it is easily accessible. Carefully and gently blot the objective with one sheet of lens paper, holding the paper at the edges, until the oil remaining on the objective is not enough to “wet” the paper. Then, using a clean lens paper, fold several times into a strip, and saturate the folded end with methanol. Carefully wipe the objective lens outward from the center in the 4 compass directions, using a new folded paper saturated with methanol each time. If there is excess oil on the metal part of the objective, soak up with a new, dry folded paper. Then with a final new, methanol-saturated folded paper wipe around the metal part of the objective, not touching the lens. Lower the lens below the stage surface.

APPENDIX D.

H-Ras Purification Protocol

his₆-TEV-H-RAS (1-181), or his₆-TEV-H-RAS (1-184)

23729 Da (pre cleavage), pI= 5.32, Σ =19370

20760 Da (post cleavage), pI= 5.04, Σ =13410

Sequence:

MSYYHHHHHDYDIPTTENLYFQGAMAMTEYKLVVVGAGGVGKSALTIQLIQNHFVDEYDPTIE
DSYRKQVVIDGETCLLDILDITAGQEEYSAMRDQYMRTGEGFLCVFAINNTKSFEDIHQYREQIK
RVKDSDDVPMVLVGNKSDLAARTVESRQAQDLARSYGIPYIETSAKTRQGVEDAFYTLVREIRQ
HKLRKLNPPDESGPGC*

Lysis buffer:

50 mM Na₂HPO₄ pH 8.0

150 mM NaCl

0.4 mM TCEP

1 mM PMSF

DNase

*2x 1mL of 200mM PMSF was used during the purification

Wash Buffer:

50 mM Na₂HPO₄ pH 8.0

150 mM NaCl

0.5 mM TCEP

15mM Imidazole

HiTrap chelating column elution buffer:

50 mM Na₂HPO₄ pH 8.0

300 mM NaCl

250 mM imidazole

0.5 mM TCEP

(add 10% glycerol to prevent RAS from crystalizing/ppt before starting concentrating step).

Protocol:

1. Transform BL21 (DE3) cells. Plate on LB containing 100µg/mL carbenicillin / Ampicillin.
Next day, pick five colonies and inoculate 100 mL of LB containing 100µg/mL carbenicillin.
Grow overnight at 37C for 16 hours. OD600 = 2.4-2.6 the next morning.
2. Inoculate 4 x 750mL 2 liter flasks of LB (1% Inoculation). Add 100µg/mL ampicillin. Grow to OD600 = 0.7-0.8 at 37C (took about 2 hours). Lower temperature to 18°C. Induce with 500 µM IPTG after ~ 1 hour at 18°C (induced at 12:30pm, harvest at 8am). Grew for ~20 hours at 18C.
3. Pour bacteria cultures into 1 liter plastic screw cap bottles. Centrifuge at 5000xg in Sorval centrifuge for 20 minutes at 4C.
4. Resuspend pellets in lysis buffer and Lyse bacteria using sonicator (around 50mL of lysis buffer used).
5. Spin at 30,000xg in JA-17 (Avanti) rotor for 35 minutes. Keep supernatant.
6. Recirculate the clarified lysate over a single HiTrap (Co²⁺) column (2-3 mL bed volume) that was equilibrated in lysis buffer.
7. Wash with 10x column volumes of wash buffer.
8. Elute with 2-4 bed volumes Elution buffer (or create Gradient)
9. Add glycerol to a final concentration of 10%.
10. Concentrate cleaved protein with Vivaspin 500 (5 or 10 kDa MWCO).

11. Exchange into EDTA buffer in concentrator:
13. 50 mM EDTA
14. 40 mM HEPES pH 7.4
15. 1mM TCEP
16. 150 mM NaCl
17. Incubate 5 min. This removes the Mg²⁺ ion coordinating the bound nucleotide. Repeat this process ~5x times to begin with.
12. Take nanodrop reading of Apo-Ras to determine concentration and whether additional EDTA spins are necessary (A260/280 ratio).
13. Exchange back into storage buffer to replenish Mg and remove free nucleotides / EDTA.
14. Add excess nucleotide of your choosing (GMPP-N-P, GTP, GDP, etc.). Add to at least 5 fold molar excess of G-protein.
15. Run SDS-PAGE gel to determine purity of Ras.

Example Final product:

H-RAS (1-181), C181S; 20760 Da

10.8 mg/mL (A280=6.949 on nanodrop); 518 μ M, 4 mL

43 mg total yield

APPENDIX E.

Protocol for RAW 264.7 Culture Method

Cell Culture and Transfections.

Starting from cryogenic stocks, RAW 264.7 macrophages were grown at 37°C under 5% CO₂ in supplemented DMEM media containing 2 mM GlutaminePlus, 20 mM HEPES pH 7.2 with NaOH, 100 U/mL penicillin, 100 µg/mL streptomycin, and 10% FBS in media flasks (T25 to T175). Cells were washed in D-PBS pH 7.2 with HCl and passaged upon reaching ~80% confluency, as recommended by ATCC. Cell scrapers are effective at removing these semi-adherent cells from flask surfaces. Single cell or population experiments used RAW cells following at most 14 or 5 such passages, respectively.

*Healthy cell populations appear as significantly polarized. RAW 264.7 cells do not seem to divide confluent – in other words they can build in piles rather than homogeneously distributed. This is normal.

*RAW 264.7 cells produce more CO₂ than some other cell lines. The HEPES supplementation is important in maintaining physiological pH values.

Cell Imaging and Analysis

Cells were counted by hemocytometer and plated at known density in 96 well imaging plates, then subsequently incubated at 37°C under 5% CO₂ for ~24 hours to facilitate cell adhesion and generate conditions of steady state cell polarization. In the bottom of each well, cells attach to a flat glass surface and spontaneously polarize in the absence of an attractant gradient.

For single cell studies, only polarized cells with extended, actively ruffling leading edge pseudopods were counted for the study. For each cell the value of the initial t = 0 timepoint was used to normalize all timepoints. Subsequently, for a group of at least 3 cells in a single cell experiment, corresponding normalized timepoints were averaged to generate a mean value for

each timepoint. Finally, the resulting mean timepoints for individual experiments were averaged over all experiments to generate a global mean and its standard error of the mean (SEM) for N = the number of experiments. Statistical significance of differences between global means was calculated using student's t-test.

Analysis of population timecourse data was as follows. In each single experiment, a population of 1245 ± 125 cells was captured in a super-image generated by stitching together 64 or 36 unit areas in an 8 x 8 (or 6 x 6) grid using Nikon Elements Software. A unit area is an objective capture. At each timepoint, the number of polarized cells with extended leading edge pseudopods was counted in Fiji (ImageJ) yielding an average over the 64 or 36 unit areas of that super-image. For each super-image, the resulting mean timepoints were normalized to the mean initial value of the $t = 0$ timepoint. Finally, the final global mean timecourse was determined by averaging the corresponding mean normalized timepoints from different super-images (experiments), yielding the global mean timepoints and their SEM for N = the number of super-images. The statistical significance of differences between global means was determined as described above for single cell studies.

APPENDIX F.

Protocol for RAW 264.7 NSAID Addition Experiments, Fast Methodology

Supplemented DMEM

DMEM

20mM HEPES pH 7.4

2mM GlutaminePlus

100 U/mL Penicillin & Streptomycin

10% FBS

*All drugs used in chapter II are 1000x soluble in DMSO. Naproxen takes significant heating, vortexing, and lower concentrations to dissolve. PDGF should be made and added in DMEM as a protein would be negatively affected by organic solvent.

*When opening or closing the environmental chamber on the microscope stage to add drug, take a precaution to not “bump” any part of the chamber or matriplate. This will shift the saved X,Y coordinates and you will no longer be imaging the same cells. There are multiple methods to do this– the chamber can be clamped, or the lid of the chamber can be always left slightly open. The closing of the lid is magnetized and will disturb the position of the plate. It is also beneficial to move the 96 well plate to a corner of the humidity chamber, and the humidity chamber to the same corner of the microscope stage. Ensuring these components stay in their corners helps you reorient if a disturbance does occur.

1. Obtain healthy RAW 264.7 cells confluent to around 80% and at a passage number less than 6.
2. Scrape cells and reconstitute in supplemented DMEM of a reasonably low volume (2-8 mL, depending on size of flask being scraped)
3. Count cells on hemocytometer and dilute cells to 0.75 to 1×10^5 per mL with supplemented DMEM. Fluorbrite DMEM may be necessary for transformed cells.

*Make note of whether the cells are clumped when looking at them on the hemocytometer – when depositing cells in a 96 well plate, well-separated cells are preferable.

4. Add 0.5 mL of cells to the required number of wells (96 well matriplate, optical glass).
Ensure proper mixing of master stock and of individual wells to aid in homogenous distribution. It can be helpful to add to wells in a recognizable pattern (e.g. a square, then a line, etc). to aid when remembering where you have already used on the microscope.
5. Incubate cells at 37°C, 5% CO₂ overnight.
6. Prepare the microscope, ensuring enough time for the environmental chamber to warm and humidify to 37°C prior to inserting plate.
7. Set desired microscope conditions (DIC, laser turret, light power, focus, etc.) and choose an area within a well representing well polarized cells (and fluorescent if transformed).
8. Save the X,Y,Z coordinate of your chosen location.
9. Collect a 0 minute timepoint (8x8, 6x6 large image for population studies)
10. Add 0.5 µL of 1000x drug stock to sample using micropipette or Hamilton syringe. Do not add directly over objective to avoid capturing local effect of very high drug concentration. When drug is added, make sure to take a mark of the current time. Gently pump mix 8x using ~100 µL volume on a micropipette, and not directly over the objective capture area. This ensures you do not forcefully unadhere your cells of interest. Refer to the second asterisk to ensure you do not disturb the X,Y coordinates of the plate.
11. Using your timestamp taken when you added the drug, take a 2.5 minute and 5 minute timepoint. Typically leading edges would respond to a drug within 5 minutes. PDGF was slower.
12. Once the 5 minute timepoint is captured, the next experiment can be started, and the experimenter can return at the 1 hour (or chosen timepoint) mark using the saved coordinates.

APPENDIX G.

Protocol for RAW 264.7 NSAID Addition Experiments, Slow Methodology

*Follow steps 1-9 in appendix E to set up the cells for experimentation.

1. Add 0.25 μL of 500x drug stock using a 1 μL or a 5 μL Hamilton syringe. Only a Hamilton syringe is accurate enough for such small volumes. Gently pump mix 8x using ~ 100 μL volume on a micropipette, and not directly over the objective capture area. This ensures you do not forcefully unadhere your cells of interest. Refer to the second asterisk in appendix E to ensure you do not disturb the X,Y coordinates of the plate.

*It is beneficial to use a 7000 series Hamilton, which holds zero dead volume. Take care to not pull the plunger out of the barrel, it can be difficult to re-insert such a small needle.

2. Take a timestamp upon drug addition and wait to capture a 5 minute timepoint. It is important to wait 5 minutes after each addition to capture the drugs' effect of the leading edge, if any.

*When practiced, this author could begin an additional experiment in between the 0 minute and 5 minute timepoint.

3. Repeat steps 1-2 every 30 minutes for each experiment, for a minimum of 2 hours. Using this protocol, the final concentration as in appendix E will be reached at 1.5 hours. However, twice the volume will be used. If a direct comparison between appendix E and F data is desired, it is important to do a new carrier vessel control using the proper volume.

APPENDIX H.

Protocol for Sfp Protein Site-Specific Labeling Procedure

Labeling buffer

50mM HEPES, pH 7.5

10mM MgCl₂

0.2 micron filtered

* Before labeling consider unreacted dye clean-up methodology, and whether it has a maximum volume for cleanup.

1. Combine equimolar amounts of maleimide-dye and Coenzyme-A in 50mM HEPES, pH 7.5. Ensure that only TCEP or no reducing agent is present.
2. Leave mixture at room temperature for 30 minutes.
3. Quench remaining free dye using 5 fold molar excess of sulfonyl reducing agent of choice - DTT or BM-E.
4. In a 500uL Eppendorf, mix sfp labeling buffer, 15% glycerol by volume, 30uM conjugated dye-Coenzyme A (CoA) from steps 1-3, and 1-5mM beta-mercaptoethanol, or other reducing agent. Add MiliQ water to final desired volume (100 uL)
5. After ensuring glycerol is fully combined with other buffers, add proteins (3uM Sfp enzyme, 10uM target protein).
6. Leave at 4 °C for 4 hours.
7. Equilibrate Bio-Rad mini P6 spin columns in storage buffer of choice. 3-4 buffer exchanges results in >99% buffer replacement.
8. Insert spin columns into 15mL conical tubes, the bottoms of which have been packed with a kimwipe. This adaptor allows swinging bucket centrifuge use.

*swinging bucket centrifuge use is important as a fixed-angle rotor may allow unconjugated dye to bypass the gel filtration matrix of the column by being forced down the sides of the column.

9. Add sample to column and spin (1000 x g, 3 minutes) to elute (or otherwise given column instructions for elution). The free dye should remain in the column due to the much greater accessible volume for the smaller sized dye.
10. Confirm both A_{280} and A_{555} (or otherwise given fluorophore emission spectra) on nanodrop.
11. Subaliquot labeled protein and snap freeze. Store -80°C .

APPENDIX I

Diffusion Coefficient Considerations

Typically, the diffusion coefficients presented in this work are calculated using the Schütz method, where the probability distribution of a square displacement r^2 or bigger over the course of Δt was plotted and fit to the equation:

$$P(r^2, \Delta t) = 1 - e^{-r^2/\langle r^2 \rangle}$$

For a single-component fit, where $\langle r^2 \rangle$ is the mean square displacement value (79, 110, 171).

When considering the displacement value, a simple calculation shows us that we can capture “true” diffusion speeds in our experimental setup. For a camera with pixel size 16x16 μm (photometrics evolve 512), a point spread function is no larger than $r = 4$ pixels

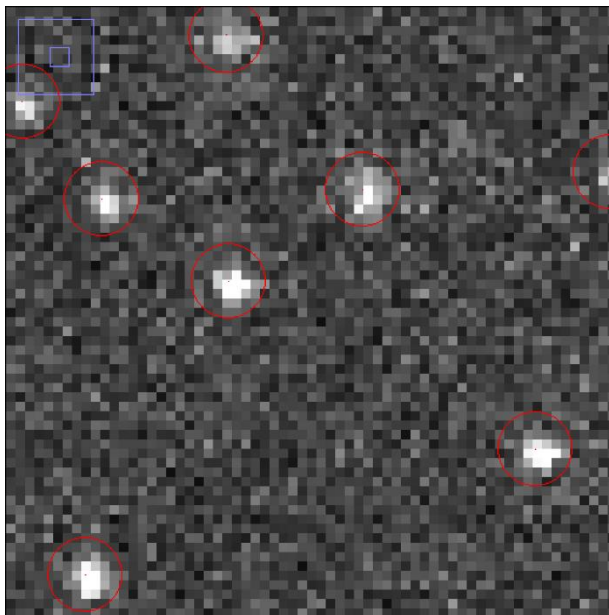


Figure A1.1. pixel measurements of normal point spread functions in TIRF apparatus. The average point spread function of a track is determined to have a radius of 4 pixels, equal to 64 microns. Each track is highlighted in red corresponding to the track radius.

(64 μm). Tracks with distances larger than 10 pixels apart in subsequent frames are disregarded as independent events. Therefore, a particle would have to travel 10 pixels (160 μm) per frame

to be considered “too fast”, corresponding to an $8,000 \text{ um}^2 / \text{s}$ diffusion coefficient, several orders of magnitude larger than those previously measured *in vitro*. (19, 79, 110).

Additionally, previous publications have shown that the diffusion coefficient of a larger construct were accurately predicted by the sum of the frictional drag of its subcomponents, an unlikely scenario if the empirical D captured was inaccurate.

A theoretical calculation of diffusion coefficient is notoriously difficult, as shown below:

Constants:

Boltzmann constant (K_b) = $1.38 \times 10^{-23} \text{ m}^2 \text{ kg s}^{-2} \text{ K}^{-1}$

η (water) = $9 \times 10^{-4} \text{ Pa s}$ (or $\text{kg m}^{-1} \text{ s}^{-1}$)

η (lipid bilayer) = 0.1 Pa s (or $\text{kg m}^{-1} \text{ s}^{-1}$) (172, 173)

$T = 298 \text{ K}$

$r = 9 \text{ \AA}$ (length of phospholipid)

Diffusion coefficient is inversely proportional to the sum of frictional drag for small Reynolds' number objects where inertial terms can be ignored (110, 172).

$$D = \frac{1}{\sum_i(f_i)}$$

In terms of energy, a given molecule will have an average kinetic energy at a temperature T of $K_b / 2$. This can be related to diffusion as

$$D = \left(\frac{1}{f}\right) K_b T$$

(174, 175)

It is also known that frictional drag for low Reynolds' number objects can be related

$$f = 6 \pi \eta r$$

(172, 174)

Using these simple equations, assuming cross-sectional area of a phospholipid is similar to the frictional drag of a sphere, and using the constants listed above, a theoretical diffusion constant for various proteins can be calculated.

For a protein with no protein keel insertion into the membrane, the frictional drag is equivalent to that of a single lipid. Drag from the aqueous layer is ignored, as it is two orders of magnitude smaller.

However, we know that phospholipids are not spheres, and that drag across a cylinder is a tensor, a function of the direction of drag across different faces of the cylinder. This can result in turbulent flow. We also know that the viscosity of the bottom leaflet of a supported lipid bilayer is significantly different from either the top leaflet or the aqueous phase.

Attempts have been made to compensate for these and other problems (176, 177, 178) with varying degrees of success. However, the work presented herein relies on empirical measurements only.